

Alma Mater Studiorum – Università di Bologna

DOTTORATO DI RICERCA IN
CHIMICA

Ciclo XXVI

Settore Concorsuale di afferenza: 03/B2

Settore Scientifico disciplinare: CHIM-07

DESIGN AND FABRICATION OF BIOCOMPATIBLE SCAFFOLDS FOR THE
REGENERATION OF TISSUES

Presentata da: Barbalinardo Marianna

Coordinatore Dottorato

Prof. Aldo Roda

Relatore

Prof. Fabio Biscarini

Correlatore

Dr. Francesco Valle

Esame finale anno 2014

*Dedico questo lavoro di tesi a Luigi ed
a tutte le persone che hanno creduto in me*

Table of Contents

Abstract	1
Chapter 1. State of the art	3
1.1 Regenerative Medicine, Tissue Engineering and Nanotechnologies	3
1.2 Scaffolds	5
1.3 Scaffold fabrication: top-down & bottom-up approaches	7
Chapter 2. Experimental techniques	11
2.1 Deposition and patterning	11
2.2 Scanning Electron Microscopy	15
2.3 Immuno-fluorescence assays	22
2.4 Atomic Force Microscopy	27
2.5 Cell culture	30
Chapter 3. Neuron cell alignment by patterning gradients of extracellular matrix protein: the laminin case (2D scaffold)	35
3.1 Introduction	35
3.2 Fabrication and characterization of laminin pattern	37
3.3 Analysis of patterned protein gradients	38
3.4 Analysis of cell nuclei orientation	41
3.5 Correlation between laminin gradient and orientation order parameter	43
3.5 Conclusions	44
Chapter 4. Fibrin 3D-scaffolds for the reconstruction of urethra	47
4.1 Introduction	47
4.2 Fabrication of scaffold based on fibrin	52
4.3 Porosity analysis	55
4.4. Correlation of scaffold multiscale morphology and cell viability	58
4.5 Conclusions	60
Chapter 5. Enhancing fibrin scaffold functionality with drug delivery	63
5.1 Introduction	63
5.2 Blending retinoic acid into fibrin scaffolds with calcium carbonate microcrystal: modulation of neuronal stem cell differentiation	65
5.3 Conclusions	70
Chapter 6. Chitin 3D-scaffold for cornea regeneration	73
6.1 Introduction	73
6.2 Changing the physical chemical properties: different squid pen	

deacetylation	76
6.3 Cell adhesion on squid pen	78
6.4 Conclusions	81
Conclusions and Perspectives	85
Participation to meeting and conference	87
Training	88
Publications	88

Abstract

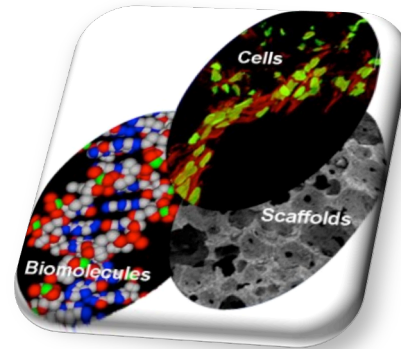
Regenerative medicine and tissue engineering attempt to repair or improve the biological functions of tissues that have been damaged or have ceased to perform their role through three main components: a biocompatible scaffold, cellular component and bioactive molecules. Nanotechnology provide a toolbox of innovative scaffold fabrication procedures in regenerative medicine. In fact, nanotechnology, using manufacturing techniques such as conventional and unconventional lithography, allows fabricating supports with different geometries and sizes as well as displaying physical chemical properties tunable over different length scales. Soft lithography techniques allow to functionalize the support by specific molecules that promote adhesion and control the growth of cells. Understanding cell response to scaffold, and *viceversa*, is a key issue; here we show our investigation of the essential features required for improving the cell-surface interaction over different scale lengths.

The main goal of this thesis has been to devise a nanotechnology-based strategy for the fabrication of scaffolds for tissue regeneration. We made four types of scaffolds, which are able to accurately control cell adhesion and proliferation. For each scaffold, we chose properly designed materials, fabrication and characterization techniques.

In the following chapters the different techniques and applications are described. In Chapter 1 a brief introduction on the state of art of nanotechnology, nanofabrication techniques and regenerative medicine, with a particular focus on the thematic related to fabrication of scaffolds is presented. In Chapter 2 a detailed description of the main fabrication and characterization techniques employed in this work is reported. Chapter 3 (chemical and topographical control) describes an easy route to obtain a control over cell proliferation close to 100% accuracy. The example is based on cell guidance on hydrophobic and chemically inert material such as polystyrene. Systems with controlled topography may be of interest in the field of tissue engineering to make systematic studies on the relationship between topography and cell behaviour. In Chapter 4, it is shown the fabrication, characterization and analysis of scaffolds to be used as supports for the reconstruction of the human urethra for the treatment of urethral strictures. The supports are made of a material (fibrin gel) that is biocompatible, biodegradable and already used in clinical stage and that is possible to be used to fabricate a tubular geometry. Chapter 5 describes the fabrication of a bioactive fibrin scaffold where microcrystals of calcium carbonate loaded with retinoic acid were incorporated to obtain its controlled release and the differentiation of stem cells to neurons. A key feature of some organs is to be constituted by transparent tissue, for example the eye cornea. In Chapter 6 it is shows the fabrication of a scaffold via the top-down strategy using a scaffold manufactured by nature and composed of extremely ordered chitin fibers: squid pen. The squid's pen is a support consisting of chitin fibers transparent, biocompatible, low cost and displaying high mechanical resistance. This material can be a great alternative to the materials used in the literature. In Chapter 7 conclusions are given.

Chapter 1

State of the art



This chapter is dedicated to a brief introduction on the state of art of regenerative medicine, nanotechnologies, nanofabrication techniques and nanobiotechnology, with a particular focus on the thematic related to the applications for scaffold fabrication.

1.1 Regenerative Medicine, Tissue Engineering and Nanotechnologies

Regenerative medicine has brought worldwide high expectations for a great number of current human illnesses. Diseases, such as Parkinson's disease, Alzheimer's disease, osteoporosis, spine injuries or cancer, might in the near future be treated with methods that aim at regenerating diseased or damaged tissues¹. The perspective of regenerating damaged or nonfunctional tissues by using an off-the-shelf synthetic product is a driving force for medical science. Today's interest in nanomedicine keeps growing because the application of nanotechnology tools to the development of structures at the molecular level enables the improvement of the interactions between material surfaces and biological entities².

Nanotechnology offers promising perspectives in biomedical research and in clinical practice. Nanofibrous materials that mimic the native extracellular matrix (ECM) and promote the adhesion of various cells are being developed as tissue-engineered scaffolds for the skin, bone, vasculature, heart, cornea, nervous system, and other tissues². A range of novel materials has been developed to enhance the bioactive or therapeutic properties of these nanofibrous scaffolds via surface modifications, including the immobilization of functional cell-adhesive ligands and bioactive molecules such as drugs, enzymes and cytokines³. As a novel approach, nanofibers prepared by using industrial scale needleless technology have been recently introduced, and their use as scaffolds to treat spinal cord injury or as cell carriers for the regeneration of the injured cornea is the subject of many recent works⁴. Cell therapy is a modern approach of regenerative medicine for the treatment of various diseases or injuries that is based on the accurate positioning and differentiation of stem cells. As an example, to follow the migration and fate of transplanted cells, superparamagnetic iron oxide nanoparticles have been developed for cell labelling and non-invasive monitoring of cells in the living organism, with successful applications in, e.g, the central nervous system, heart, liver and kidney and also in pancreatic islet and stem cell transplantation⁵.

In this strategy, the role of nanotechnology is improving of the toolbox for the construction of a biocompatible scaffold that, in combination with living cells and/or bioactive molecules,

replaces, regenerates or repairs damaged cells or tissue. The crucial scaffold requirements include biocompatibility, controlled porosity and permeability, physical properties comparable to the targeted tissue and, additionally, they must be a suitable support for cell attachment and proliferation. To promote cell adhesion and growth, the addition of nanotopographies to the biomaterial surface can improve its bioadhesive properties, e.g. the surface roughness, aside from the chemistry, is an important factor influencing cell attachment and spreading⁶. The large surface area of nanostructured materials enhances the adsorption of adhesive proteins such as fibronectin and laminin, which mediate cell-surface interactions through integrin cell surface receptors^{7,8}. Because nanotopography has an essential role in guiding cell behaviour *in vivo*, it is now being used in biomaterials science as a tool for controlling tissue regeneration. A wide variety of techniques, soft-lithography included, have been used to produce nanotopography on biomaterial surfaces leading both to an ordered topography with a regular controlled pattern and to an unordered topography with random orientation and organisation.

Although cells have micrometre size, they evolve *in vivo* in close contact with the ECM, a substratum with topographical and structural features in the nanometre range. The interactions between cells and the ECM influence cell growth, guide cell mobility and affect the general behaviour of cells. Nanotechnologies provide the possibility to produce surfaces, structures and materials with nanoscale features that can mimic the natural environment of cells, to promote specific functions, such as cell adhesion, cell mobility and cell differentiation.

Nanomaterials used in biomedical applications include nanoparticles for molecule delivery (drugs, growth factors, DNA), nanofibres for tissue scaffolds, surface modifications of implantable materials or nanodevices, such as biosensors^{9,10}. The combination of these elements within tissue engineering (TE) is an excellent example of the great potential of nanotechnology applied to regenerative medicine. The ideal goal of regenerative medicine is the *in vivo* regeneration or, alternatively, the *in vitro* generation of a complex functional organ consisting of a scaffold made out of synthetic or natural materials that has been loaded with living cells (Figure 1.1). Ideally, stem cells are to be used owing to their ability to generate all types of tissues and their unlimited self-renewal capacity. The functionalization of such a porous scaffold with different biomolecules (depending on the targeted cells) or the entrapment of nanoparticles carrying growth factors, drugs or genes, could enhance the success of the TE strategy greatly. However, crucial issues, such as stem cell isolation from the patient and their proliferation, the culturing process in a bio-reactor and the time delay before the engineered hybrid construct is implanted back into the patient, present major bottlenecks for this approach that promise to become a well established standardised procedure in the near future.

The rapid expansion of nanotechnology during the past ten years has led to new perspectives and advances in biomedical research as well as in clinical practice. As nanotechnology is defined by the size of a material or manipulation on the molecular level, it involves a broad range of nanoscaled materials used in various fields of regenerative medicine, including TE, cell therapy, diagnosis and drug and gene delivery.

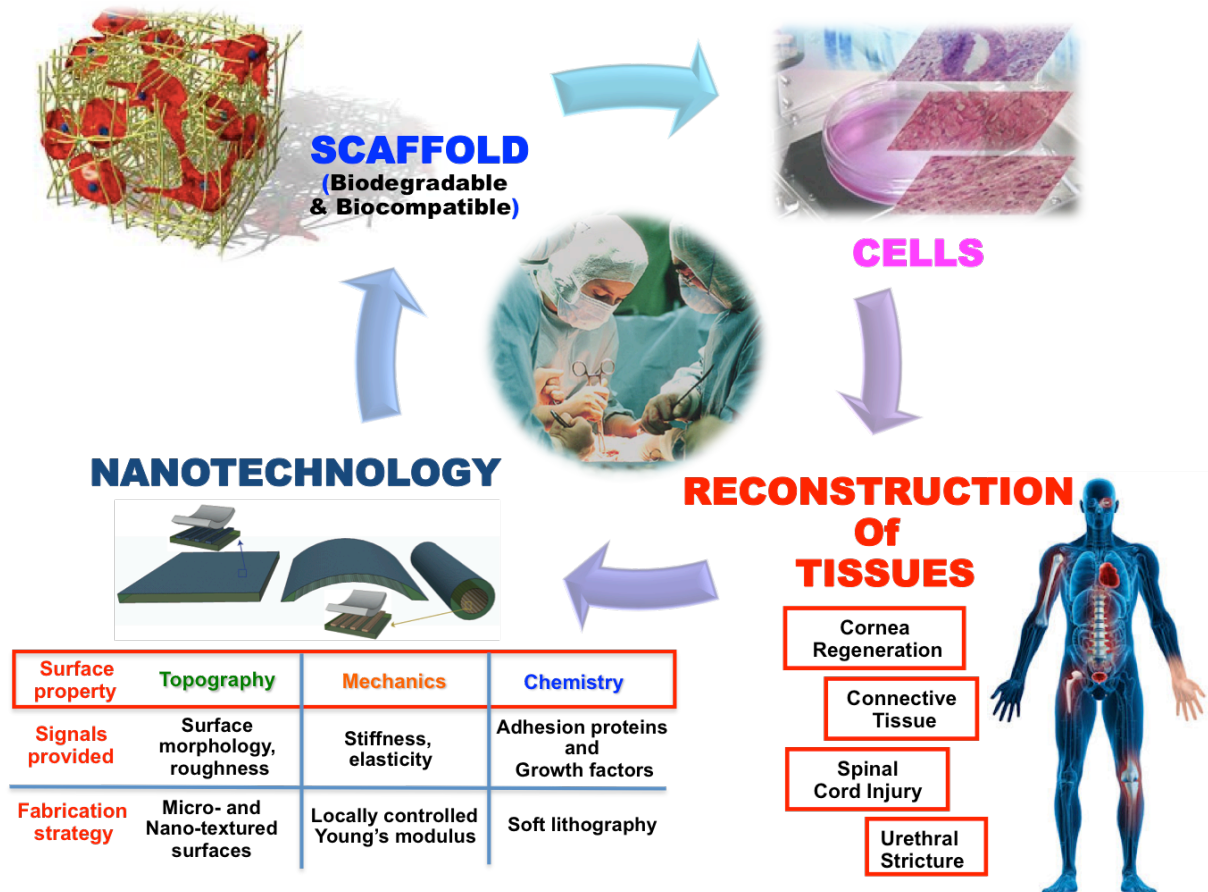


Figure 1.1: Regenerative medicine and nanotechnology approach for tissue regeneration.

1.2 Scaffolds

To regenerate a natural tissue a crucial step is to achieve the correct three-dimensional structure able to induce the adequate stimuli to the cells and to promote the tissue regrowth. Recent studies show that the isolated cells are hardly able to organize themselves spontaneously to form complex tissues in the absence of three-dimensional structures that guide them and stimulate their activities¹¹. In almost all examined cases cultured cells tend to multiply and proliferate only in two dimensions. The three-dimensional tissue regeneration requires a support (scaffold) that emulates the ECM for the organization of cells in complex structures. Apart from blood cells, most, if not all other normal cells in human tissues are anchorage-dependent, residing in a solid matrix called ECM. There are numerous types of ECM¹²⁻¹⁴ in human tissues, which usually have multiple components and tissue-specific composition¹⁵. They can be generally classified into five categories according the function they have to carry on in the tissues and that are briefly listed here. Firstly, ECM provides structural support and physical environment for cells residing in that tissue to attach, grow, migrate and respond to signals. Secondly, ECM gives the tissue its structural and therefore mechanical properties, such as rigidity and elasticity that is associated with the tissue functions. For example, well-organized thick bundles of collagen type I in tendon are highly

resistant to stretching and are responsible for the high tensile strength of tendons. On the other hand, randomly distributed collagen fibrils and elastin fibers of skin are responsible for its toughness and elasticity. Thirdly, ECM may actively provide bioactive cues to the residing cells for regulation of their activities. Fourthly, ECM may act as reservoir of growth factors and potentiate their bioactivities. For instance, heparin sulfate proteoglycans facilitate bFGF dimerization and thus activities¹⁶. Fifthly, ECM provides a degradable physical environment so as to allow neovascularization and remodeling in response to developmental, physiological and pathological challenges during tissue dynamic processes namely morphogenesis, homeostasis and wound healing, respectively.

Intuitively, the best scaffold for an engineered tissue should be the ECM of the target tissue in its native state¹⁷. Nevertheless, the multiple functions, the complex composition and the dynamic nature of ECM in native tissues make it difficult to be exactly mimicked. Therefore, contemporary concept of scaffolding in TE is to mimic the functions of native ECM, at least partially. Let us consider these functions and features as follows:

- **Architecture:** Scaffolds should provide void volume for vascularization, new tissue formation and remodeling so as to facilitate host tissue integration upon implantation. The biomaterials should be processed to give a porous enough structure for efficient nutrient and metabolite transport without significantly compromising the mechanical stability of the scaffold. Moreover, the biomaterials should also be degradable upon implantation at a rate matching that of the new matrix production by the developing tissue.
- **Cyto- and tissue compatibility:** Scaffolds should provide support for either extraneously applied or endogenous cells to attach, grow and differentiate during both in vitro culture and in vivo implantation. The biomaterials used to fabricate the scaffolds need to be compatible with the cellular components of the engineered tissues and endogenous cells in host tissue.
- **Bioactivity:** Scaffolds may interact with the cellular components of the engineered tissues actively to facilitate and regulate their activities. The biomaterials may include biological cues such as cell-adhesive ligands to enhance attachment or physical cues such as topography to influence cell morphology and alignment. The scaffold may also serve as a delivery vehicle or reservoir for exogenous growth-stimulating signals such as growth factors to speed up regeneration. In this regard, the biomaterials need to be compatible with the biomolecules and amenable to an encapsulation technique for controlled release of the biomolecules with retained bioactivity. For example, hydrogels synthesized by covalent or ionic crosslinking can entrap proteins and release them by a mechanism controlled by the swelling of hydrogels¹⁸.
- **Mechanical property:** Scaffolds provide mechanical and shape stability to the tissue defect. The intrinsic mechanical properties of the biomaterials used for scaffolding or their post-processing properties should match that of the host tissue. Recent studies on mechanobiology have highlighted the importance of mechanical properties of a scaffold on the seeded cells. Exerting traction forces on a substrate, many mature cell types, such as epithelial cells, fibroblasts, muscle cells, and neurons, sense the

stiffness of the substrate and show dissimilar morphology and adhesive characteristics¹⁹.

In conclusion we can sum up that the role of the scaffold is to induce tissue regeneration by providing a "temporary guide" for cell growth, under appropriate culture conditions, to accommodate the program of differentiation²⁰.

1.3 Scaffold fabrication: top-down & bottom-up approaches

Three-dimensional scaffolds have widespread applications in biomedical TE because of their nanoscaled architecture, eg, nanofibers and nanopores, similar to the native ECM.

The emerging "bottom-up" method (Figure 1.2b) focuses on fabricating microscale tissue building blocks with a specific microarchitecture and assembling these units to engineer larger tissue constructs from the bottom up.

Hydrogels have widespread applications in biomedical engineering because of their hydrated environment and tunable mechanical, chemical, and biocompatibility properties which are similar to the native ECM²¹. Recently, the bottom-up approach has emerged as an assembly process for microscale building blocks (eg, cell-encapsulating microgels) which holds great potential to fabricate complex tissue constructs, with control over the shape and compositional features of the individual building blocks²²⁻²⁴. Another advantage of the bottom-up method is the superior diffusion properties of microgels due to their controllable volume, which can obtain a high cell density after encapsulating cells. A variety of methods have been developed to fabricate microgels, including molding²⁵, folding, photolithography²⁶, molecular synthesis²⁷, and generation of microdroplets²⁸.

In the conventional "top-down" approach (Figure 1.2a), cells are seeded onto a biocompatible and biodegradable scaffold, in which cells are expected to populate in the scaffold and create their own ECM. The top-down approach based on these scaffolds has successfully engineered thin tissues, including skin, bladder, and cartilage *in vitro*. However, it is still a challenge to fabricate complex and functional tissues (eg, liver and kidney) due to the lack of vascularization systems and limited diffusion properties of these large biomimetic scaffolds.

The top-down approach based on a variety of three-dimensional scaffolds has been investigated for application in tissue engineering, due to the nanoscale structure of these scaffolds being analogous to that of the native ECM. For instance, in vascular tissue engineering, fabrication of small diameter (inner diameter, 6 mm) vascular grafts to meet clinical needs is still a big challenge, mostly due to the potential for thrombus formation. To address this challenge, Liu et al²⁹ fabricated sulphated silk fibroin nanofibrous scaffolds (S-silk scaffold) with enhanced anticoagulant activity to reduce platelet adhesion and aggregation in denuded areas on the luminal surface of vascular grafts, which may prevent thrombus formation and improve the chances of successful vascular reconstruction in small vessels. For engineering of cartilage tissue, the major limitation of currently engineered cartilage is its nonhomogeneous structure and poor mechanical properties. It has also been demonstrated that oriented scaffolds (similar to cartilage tissue *in vivo*) could greatly improve cell migration compared with the non-oriented scaffolds achieving cartilage regeneration in

vitro. Thus, how to engineer three-dimensional scaffolds with regulated oriented structures and the desired mechanical properties is still a challenge.

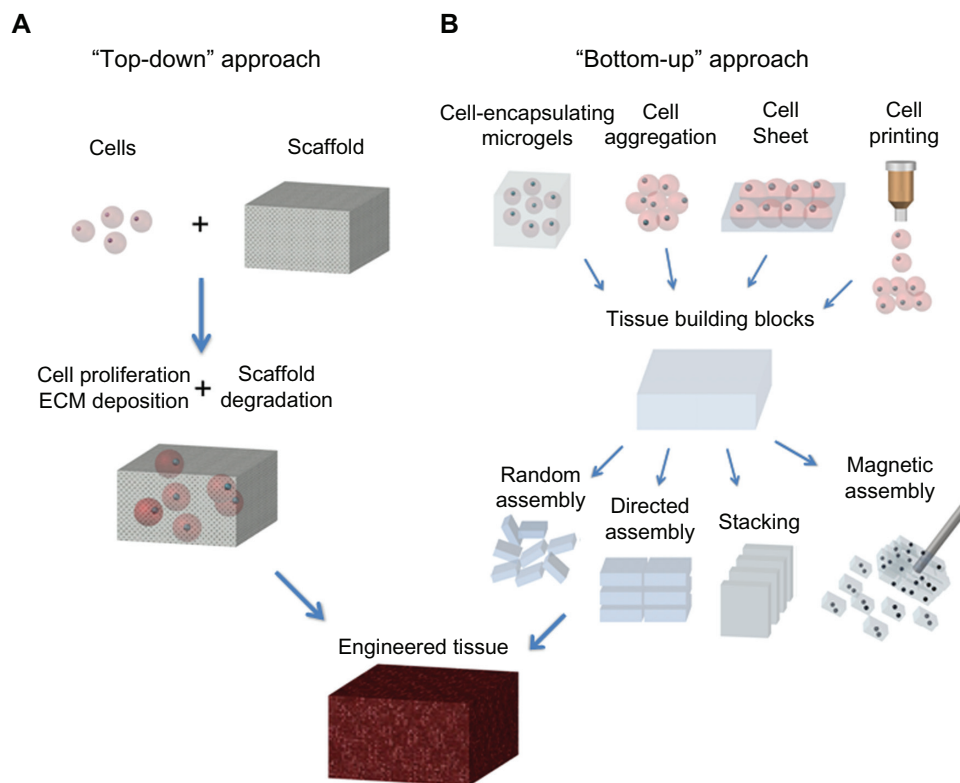


Figure 1.2: Schematic of “top-down” and “bottom-up” approaches for tissue engineering. (A) In the top-down approach, cells are seeded on a biocompatible and biodegradable scaffold and are expected to populate in the scaffold and create their own extracellular matrix. (B) In the bottom-up approach, various methods are utilized for generating tissue building blocks and these units can be engineered into large tissue constructs via multiple assembling methods.

Conventional approaches to engineering tissues based on three-dimensional biomimetic scaffolds *in vitro* involve three steps: fabrication of three-dimensional scaffolds via different techniques including electrospinning, phase separation, freeze-drying, and self-assembly; surface modification of the prepared scaffolds to enhance their biocompatibility, especially of their synthetic polymer components; and co-culture of cells on three-dimensional porous scaffolds to regenerate tissues *in vitro*³⁰. Although several thin or avascular tissues (eg, skin, bladder, and cartilage) have been engineered successfully via the top-down strategy *in vitro*, fabrication of complex and large functional tissues (eg, liver and kidney) with high cell densities and high metabolic requirements still faces challenges. This is mainly because of the limited diffusion properties of biomimetic scaffolds.

Bibliography

- 1 Khang, D., Carpenter, J., Chun, Y. W., Pareta, R. & Webster, T. J. Nanotechnology for regenerative medicine. *Biomed Microdevices* **12**, 575-587, (2010).
- 2 Boisseau, P. & Loubaton, B. Nanomedicine, nanotechnology in medicine. *Cr Phys* **12**, 620-636, (2011).
- 3 Chen, G. P., Ushida, T. & Tateishi, T. Scaffold design for tissue engineering. *Macromol Biosci* **2**, 67-77, (2002).
- 4 Kubinova, S. & Sykova, E. Nanotechnologies in regenerative medicine. *Minim Invasiv Ther* **19**, 144-156, (2010).
- 5 Leary, J. F. Nanotechnology: what is it and why is small so big? *Can J Ophthalmol* **45**, 449-456, (2010).
- 6 Valle, F. *et al.* Stable Non-Covalent Large Area Patterning of Inert Teflon-AF Surface: A New Approach to Multiscale Cell Guidance. *Adv Eng Mater* **12**, B185-B191, (2010).
- 7 Woo, K. M., Chen, V. J. & Ma, P. X. Nano-fibrous scaffolding architecture selectively enhances protein adsorption contributing to cell attachment. *J Biomed Mater Res A* **67A**, 531-537, (2003).
- 8 Zhu, X. L. *et al.* Cellular reactions of Osteoblasts to micron- and submicron-scale porous structures of titanium surfaces. *Cells, tissues, organs* **178**, 13-22, (2004).
- 9 Casalini, S., Leonardi, F., Cramer, T. & Biscarini, F. Organic field-effect transistor for label-free dopamine sensing. *Org Electron* **14**, 156-163, (2013).
- 10 Cramer, T. *et al.* Organic ultra-thin film transistors with a liquid gate for extracellular stimulation and recording of electric activity of stem cell-derived neuronal networks. *Phys Chem Chem Phys* **15**, 3897-3905, (2013).
- 11 Smith, I. O., Liu, X. H., Smith, L. A. & Ma, P. X. Nanostructured polymer scaffolds for tissue engineering and regenerative medicine. *Wires Nanomed Nanobi* **1**, 226-236, (2009).
- 12 Badylak, S. F. Xenogeneic extracellular matrix as a scaffold for tissue reconstruction. *Transpl Immunol* **12**, 367-377, (2004).
- 13 Piez, K. A. History of extracellular matrix: A personal view. *Matrix Biol.* **16**, 85-92, (1997).
- 14 Ruan, D. K. *et al.* Intervertebral disc transplantation in the treatment of degenerative spine disease: a preliminary study. *Lancet* **369**, 993-999, (2007).
- 15 Poole, A. R. *et al.* Composition and structure of articular cartilage - A template for tissue repair. *Clin Orthop Relat R*, S26-S33, (2001).
- 16 Schonherr, E. & Hausser, H. J. Extracellular matrix and cytokines: a functional unit. *Developmental immunology* **7**, 89-101, (2000).
- 17 Chan, B. P. & Leong, K. W. Scaffolding in tissue engineering: general approaches and tissue-specific considerations. *Eur Spine J* **17**, S467-S479, (2008).
- 18 Berger, J. *et al.* Structure and interactions in covalently and ionically crosslinked chitosan hydrogels for biomedical applications. *Eur. J. Pharm. Biopharm.* **57**, 19-34, (2004).
- 19 Discher, D. E., Janmey, P. & Wang, Y. L. Tissue cells feel and respond to the stiffness of their substrate. *Science* **310**, 1139-1143, (2005).
- 20 Ikada, Y. Challenges in tissue engineering. *J R Soc Interface* **3**, 589-601, (2006).
- 21 Geckil, H., Xu, F., Zhang, X. H., Moon, S. & Demirci, U. Engineering hydrogels as extracellular matrix mimics. *Nanomedicine-Uk* **5**, 469-484, (2010).

- 22 Gurkan, U. A., Tasoglu, S., Kavaz, D., Demirel, M. C. & Demirci, U. Emerging Technologies for Assembly of Microscale Hydrogels. *Adv Healthc Mater* **1**, 149-158, (2012).
- 23 Jensen, B. E. B. *et al.* Poly(vinyl alcohol) Physical Hydrogels: Noncryogenic Stabilization Allows Nano- and Microscale Materials Design. *Langmuir* **27**, 10216-10223, (2011).
- 24 Xu, F. *et al.* Three-Dimensional Magnetic Assembly of Microscale Hydrogels. *Adv. Mater.* **23**, 4254-4260, (2011).
- 25 Diez, M. *et al.* Molding Micropatterns of Elasticity on PEG-Based Hydrogels to Control Cell Adhesion and Migration. *Adv Eng Mater* **13**, B395-B404, (2011).
- 26 Du, Y. A., Lo, E., Ali, S. & Khademhosseini, A. Directed assembly of cell-laden microgels for fabrication of 3D tissue constructs. *P Natl Acad Sci USA* **105**, 9522-9527, (2008).
- 27 Qi, H. *et al.* Patterned Differentiation of Individual Embryoid Bodies in Spatially Organized 3D Hybrid Microgels. *Adv. Mater.* **22**, 5276-5281, (2010).
- 28 Moon, S. *et al.* Layer by Layer Three-Dimensional Tissue Epitaxy by Cell-Laden Hydrogel Droplets. *Tissue Eng Part C-Me* **16**, 157-166, (2010).
- 29 Liu, H. F., Li, X. M., Zhou, G., Fan, H. B. & Fan, Y. B. Electrospun sulfated silk fibroin nanofibrous scaffolds for vascular tissue engineering. *Biomaterials* **32**, 3784-3793, (2011).
- 30 Khademhosseini, A. & Langer, R. Microengineered hydrogels for tissue engineering. *Biomaterials* **28**, 5087-5092, (2007).

Chapter 2

Experimental techniques



In this chapter, an overview of the main techniques used for fabrication and patterning is provided. Scanning Electron Microscopy (SEM) has been used to characterize the scaffold morphology. Optical Microscopy has been used for Immuno-fluorescence (IF) assays, to detect specific proteins and organelles both on the membrane and inside the cell body. Atomic Force Microscopy (AFM), was performed to address in detail the scaffold morphology giving at the same time an accurate characterization of the topography.

2.1 Patterning

Soft-lithography

Soft lithography describes a whole set of techniques for microfabrication, based on printing and molding using elastomeric stamps that display the patterns of interest in bas-relief. For fabricating microstructures for biological applications, soft lithography overcomes many of the shortcomings of photolithography because it allows to work with water solutions thus allowing to control the molecular structure of surfaces by patterning complex molecules such as proteins or nucleic acids. When dealing with the relatively large features used in this work ($\leq 50 \mu\text{m}$), production of prototype patterns is convenient, inexpensive, and rapid. Microfabrication has already proved to be crucial for life science and medicine as demonstrated by the recent combinations of disease-specific genetic information¹⁻³ with combinatorial methods of organic synthesis^{4,5} and miniaturized assays for obtaining new classes of diagnostic tools⁶. The use of photolithography in the fabrication of DNA arrays was the first example that attracted a wide attention^{7,8}. Although photolithography is the technology for micropatterning most common and widely used, its application to biotechnology and life science is still limited. It is intrinsically expensive, it gives limited control over surface properties, it is often not directly applicable to proteins and cells due to the use of organic solvents, the time to go from the design to prototype can be long, and the techniques are unfamiliar and inaccessible to the majority of the life science community.

Soft-lithography encompasses several techniques that share the use of elastomeric materials to fabricate by molding the pattern transfer elements, and the application to pattern complex biological molecules⁹⁻¹¹. The main soft lithography techniques are Microcontact Printing (μCP)¹²,

Replica Molding (REM)¹³, MicroTransfer Molding (μ TM)¹⁴, MicroMolding in Capillaries (MIMICs)¹², Solvent Assisted Microcontact Molding (SAMIM)¹⁴ and Lithographically Controlled Wetting (LCW)^{15,16}. The most used elastomeric material is polydimethylsiloxane (PDMS) and in its most widely commercialized version (Sylgard 186, Dow Chemicals) it is supplied as two components, a base and a curing agent¹⁷. PDMS displays many relevant properties. It has a Young's modulus that makes it a moderately stiff elastomer (1 MPa). It is nontoxic and readily available commercially. It is intrinsically very hydrophobic (advancing contact angle of water of 110°), but its surface can be converted to a hydrophilic form ($\pm 10^\circ$) by common plasma treatments¹⁸.

The ability to change the surface properties of PDMS is useful when designing a stamp for transferring patterns of molecular species; the amount of material that is loaded on the stamp can be maximized by using a stamp with properties similar to those of the compound¹⁹. PDMS is relatively permeable to nonpolar gases, including O₂, N₂, and CO₂; this property is also essential to its use in channel systems for cell culture.

In figure 2.1 the processing steps of soft-lithographic fabrication are depicted.



Figure 2.1: The fast prototyping procedure for soft-lithography.

Starting from the original idea, the pattern is transferred to a CAD file and printed on a transparent sheet of polymer with a commercial image setter. This patterned sheet is used as a mask to prepare the master in a thin film of photoresist; a negative replica of this master with an elastomeric material becomes the stamp or mold for soft-lithography. One can start also from a commercial mask (usually of chromium/quartz or polyester) or fabricate a mask by laser ablation of a metallic thin film thus obtaining a high contrast mask²⁰. The overall cycle from design to stamp takes less than 24 hours to be completed. However, once one has fabricated the master, multiple stamps can be obtained by Replica Molding (REM) before the master deteriorates. This is another advantage of soft-lithography compared to conventional photolithography.

Replica Molding

“Replica molding” (REM) allows the fabrication of a conformal copy of the topographic information present in a master. Being the masters usually rigid, the use of an elastomer facilitates the separation of master and replica. In REM, an appropriate elastomer such as PDMS,

enables replicating highly complex master structures with nanometer features in a simple, reliable and inexpensive way. In figure 2.2 the general replica procedure is reported. The molds are prepared by casting a mixture of PDMS and curing agent (generally in a ratio 10:1) against a rigid masters. The PDMS/master is placed in a oven at 90°C for 2 hours to complete the curing process. Then the mold is peeled off and it is ready to be used as stamp. This process can be replicated many time on the same master without damaging it.

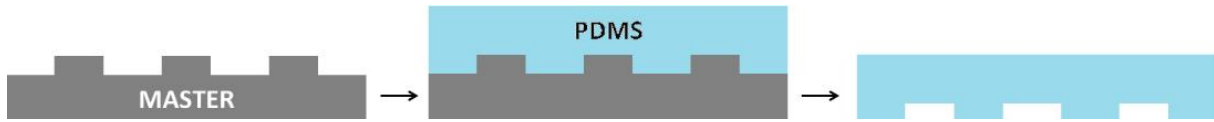


Figure 2.2: Replica molding steps.

MicroMolding In Capillaries

MicroMolding In Capillaries is one of the most common patterning techniques based on a PDMS stamp with open-end microchannels placed brought into conformal contact with the substrate to be patterned (Figure 2.3a). A low viscosity solution is then supplied at the entrance of the capillaries at one side of the mould (Figure 2.3b).

The solution is drawn into the microchannels by Laplace pressure (Figure 2.4c). In principle, no residue layer can form in areas where adhesive conformal contact between mould and substrate is already established. After solvent evaporation, the mould is removed to reveal patterned microstructures of the solute (Figure 2.3d).

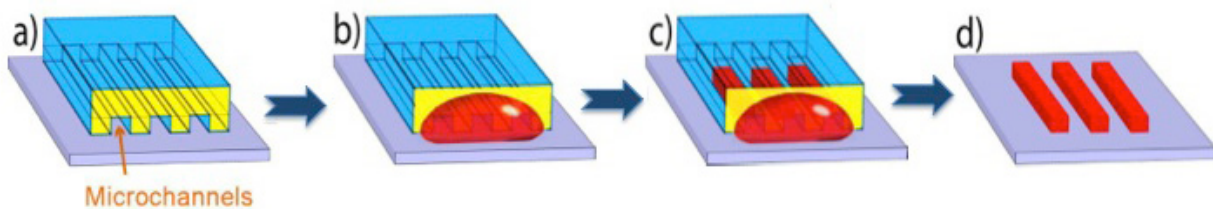


Figure 2.3: Schematic representation of MIMICs.

A zero order model of MIMICs is described in the following, referring to figure 2.4. First, we assume that $\gamma_{SV} = \gamma_{S'V}$. The liquid, whose liquid-vapor tension is γ_{LV} , fills the channel driven by Laplace pressure²¹:

$$\Delta P = 2\gamma_{LV} \cos\theta/r$$

The contact angle θ is defined by Young's equation:

$$\cos\theta = (\gamma_{SV} - \gamma_{SL})/\gamma$$

The surface tensions γ_{SV} and γ_{SL} depend on the substrate and the channel walls, and r is the effective diameter of the channel.

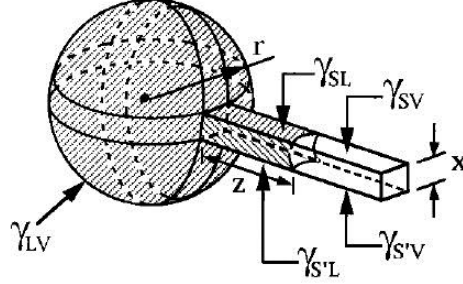


Figure 2.4: A model for MIMICs. A fluid is assumed to move from a spherical drop (radius r) into a square channel (width x) with three identical surfaces (PDMS) and one different (the substrate). The terms γ_{SV} , γ_{SL} , and γ_{LV} corresponds to interfacial free energies of solid-vapor, solid-liquid and liquid-vapor interfaces²².

The rate of the liquid flow²² in the capillary is determined by the ratio of surface tension and viscosity of the liquid, the cross-sectional size of the capillary and the length of the channel by the following equation²³ :

$$\frac{dz}{dt} = \frac{R\gamma_{LV}\cos\theta}{4\eta z} = \frac{R(\gamma_{SV} - \gamma_{SL})}{4\eta z}$$

where z is the length of the liquid capillary inside the channel, η is the viscosity of the penetrating liquid, R is the ratio between capillary volume and the surface area of the channel, and θ is the contact angle of the fluid meniscus inside the capillary. The surface tensions γ_{LV} , γ_{SV} and γ_{SL} are the surface tensions between liquid and air, channel wall and air, and channel wall and liquid, respectively. It follows upon integration that:

$$z(t) = \sqrt{\frac{R(\gamma_{SV} - \gamma_{SL})t}{2\eta}}$$

The equation shows that although the capillary force of a channel increases with decreasing hydraulic radius R , this effect is more than counterbalanced by the increased friction exerted by the channel walls, so that the filling rates are lower in smaller channels.

The shape of the imbibition front of the liquid precursors has been studied in detail²⁴. Depending on the surface energy of the channel wall γ_{SV} , different spreading regimes can be observed, as illustrated in the figure 2.5.

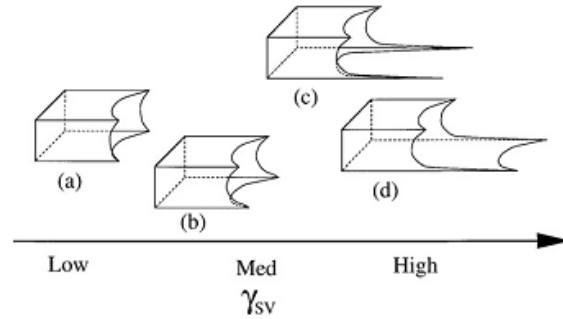


Figure 2.5: Schematic representation of different spreading regimes observed in MIMIC. Shapes of the penetrating liquids in PDMS capillaries are formed inside (a) walls with low γ_{sv} (b and c) walls with medium γ_{sv} , and (d) walls with high γ_{sv} .

Liquids penetrating inside a channel with low surface energy walls, exhibit capillary fronts that advance as a whole. As the surface energy of the channel increases, solute structures advancing in front of the macroscopic body of liquid are observed, especially in the corners between mold and substrate. Some of these structures include slipping films and shoulders. Similar regimes have been observed with differences in the velocity of imbibition on surfaces with constant γ_{sv} ²⁵.

MIMIC is a microfabrication method that works well with many different materials but at its current stage of development has also some limitations. The rate of capillary filling is rapid and complete over short distances while, over a large distance, it decreases significantly owing to the viscous drag of the fluid in the capillary. The forward ends of capillaries may fill incompletely if the hydraulic drag is sufficiently high. The rate of filling also decreases as the cross-sectional dimension of the capillary decreases and as the interfacial free energy of the surface decreases²⁴.

2.2 Scanning Electron Microscopy

Scanning electron microscopy (SEM) is one of the most versatile techniques available for the examination and analysis of the microstructure morphology and for the characterization of their chemical composition. The unaided eye can discriminate objects subtending about $1/60^\circ$ visual angle, corresponding to a resolution of ~ 0.1 mm (at the optimum viewing distance of 25 cm). The limit of resolution is defined as the minimum distances where two structures can be separated still appearing as two distinct objects. Ernst Abbe²⁶ proved that the limit of resolution depends on the wavelength of the illumination source. At a defined wavelength, when resolution exceeds this limit, the magnified image starts blurring. Because of diffraction and interference, a point of light cannot be focused as a perfect dot, the image will rather have the appearance of a larger diameter than the source, consisting of a disk composed of concentric circles with decreasing intensity. This is known as an Airy disk and is represented in figure 2.6a. The primary wave front contains approximately 84% of the light energy, and the intensity of secondary and tertiary wave fronts

decay rapidly at higher orders. Generally, the radius of Airy disk is defined as the distance between the first-order peak and the first-order trough, as shown in figure 2.6a. When the center of two primary peaks are separated by a distance equal to the radius of Airy disk, the two objects can be distinguished from each other, as shown in figure 2.6b. Resolution, in a perfect optical system, can be described mathematically by Abbe's equation. In this equation:

$$d = 0.612 \lambda / n \sin \alpha$$

where d is the resolution, λ the wavelength of imaging radiation, n the refractive index of the medium between the point source and the lens relative to free space, α is half the angle of the cone of light from specimen plane accepted by the objective (half aperture angle in radians), $n \sin \alpha$ is often called numerical aperture (NA).

Substituting the illumination source and condenser lens with electron beam and electromagnetic coils in light microscopes, respectively, the first transmission electron microscope (TEM) was constructed in the 1930s²⁷, in which electron beam was focused by an electromagnetic condenser lens onto the specimen plane. The SEM uses a focused electron beam scanned across the surface of the specimen systematically thus producing a large number of signals (secondary electrons, back-scattered electrons, characteristic X-ray, Auger electrons, cathodoluminescence, transmitted electrons and specimen current). These electron signals are eventually converted to a visual signal.

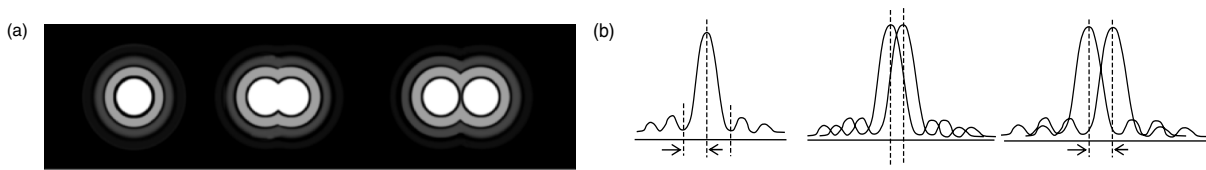


Figure 2.6: Illustration of resolution in (a) Airy disk and (b) wave front.

Image formation in the SEM is dependent on the acquisition of the signals produced by the interactions of the electron beam with the samples. These interactions can be divided into two major categories: elastic and inelastic.

Elastic scattering results from the deflection of the incident electrons by the sample atomic nuclei or by the outer shell electrons of similar energy. This kind of interaction is characterized by negligible energy loss during the collision and by a wide-angle directional change of the scattered electron. Incident electrons that are elastically scattered through an angle of more than 90° are called backscattered electrons (BSE), and yield a useful signal for imaging the sample. Inelastic scattering occurs through a variety of interactions between the incident electrons and the electrons and atoms of the sample, and results in the primary beam electron transferring substantial energy to that atom. The amount of energy loss depends on whether the specimen electrons are excited singly or collectively and on the binding energy of the electron to the atom.

As a result, the excitation of the specimen electrons during the ionization of specimen atoms leads to the generation of secondary electrons (SE), which are conventionally defined as possessing energies of less than 50 eV and can be used to image or analyze the sample. In addition to those signals that are utilized to form an image, a number of other signals are produced when an electron beam strikes the sample surface, including the emission of characteristic x-rays, Auger electrons, and cathodoluminescence (Figure 2.7).

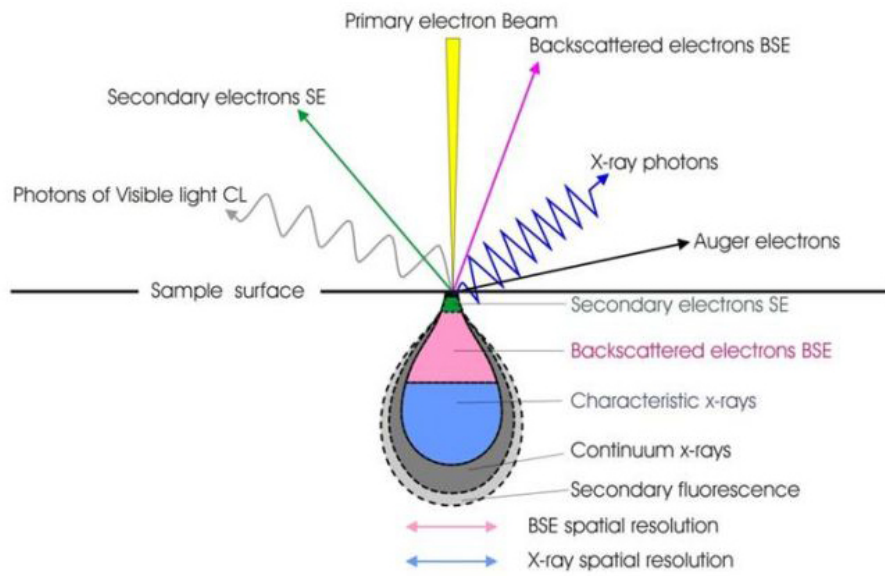


Figure 2.7: Shows the regions from which different signals are detected (from University of Glasgow Imaging Spectroscopy and Analysis Centre).

The main components of a typical SEM are the electron column, the scanning system, the detector(s), the display, the vacuum system and the electronics controls (Figure 2.8). Below the description of the main components of the SEM is reported.

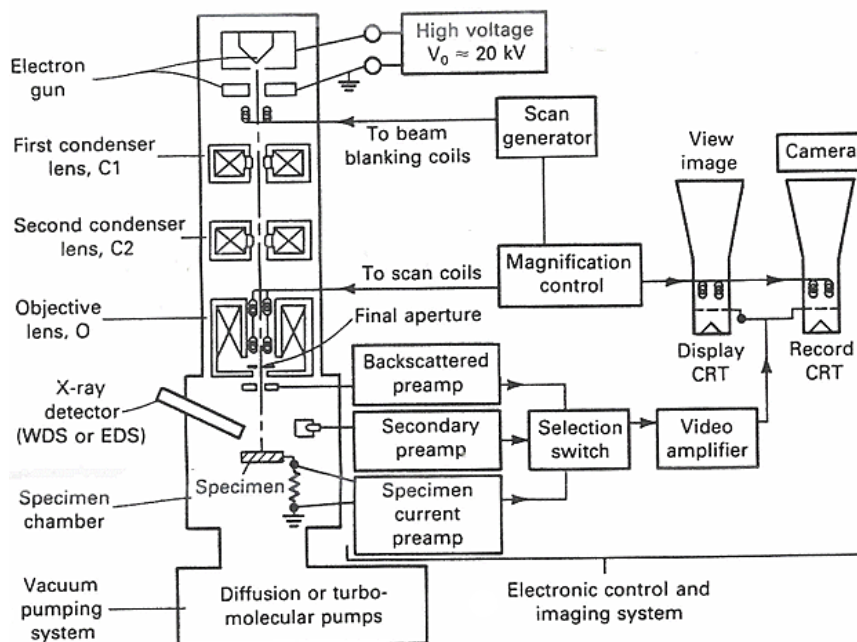


Figure 2.8: Schematic representation of SEM.

Electron Guns

The electron column, which is on the top of the column, consists of an electron gun and two or more electromagnetic lenses operating in vacuum. The electron gun generates free electrons and accelerates these electrons to energies in the range 1-40 keV in the SEM. The purpose of the electromagnetic lenses is to create a small, focused electron probe on the specimen. Most SEMs can generate an electron beam with a spot size at the specimen surface of less than 10 nm in diameter.

In this work we used a SEM Hitachi S4000, a field emission electron guns (FEG). In a FEG, a single crystal tungsten wire with very sharp tip, generally prepared by electrolytic etching, is used as the electron source. Figure 2.9a and b shows a micrograph of a typical field emission tip and the schematic structure of the FEG. There are three types of FEGs commonly used in the SEM systems: cold field emission, thermal field emission and Schottky emitters²⁸. Hitachi S4000 is a cold field emission (CFE) sources. The “cold field” means the electron sources operate at room temperature. The emission of electrons from the CFE purely depends on the electric field applied between the anodes and the cathode. Although the current of the emitted electron beams is very small, a high brightness can still be achieved because of the small electron beam diameter and emission area. An operation known as “flashing” in which the field emission tip is heated to a temperature of more than 2,000 K for a few seconds is needed to clean absorbed gas on the tip. Compared with thermionic sources, CFE provides enhanced electron brightness, typically 100X greater compared to a typical tungsten source. However, field emitters must operate under ultrahigh vacuum to stabilize the electron emission and to prevent contamination.

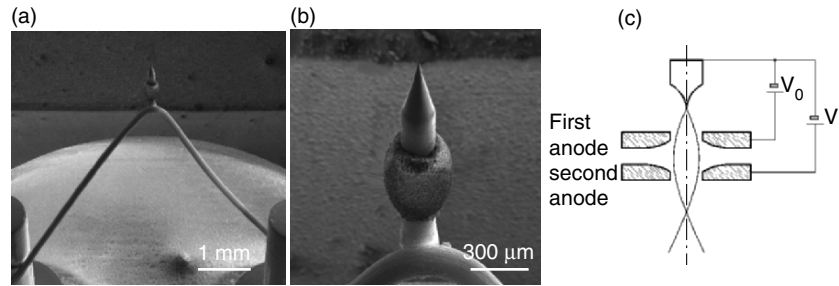


Figure 2.9: (a) Field emission source with extreme sharp tip; (b) a higher magnification image; and (c) schematic diagram of a typical field emission electron source. The two anodes work as an electrostatic lens to form electron beams.

Electron Lenses

The purpose of the electron lenses is to produce a convergent electron beam with desired crossover diameter. The lenses are metal cylinders with cylindrical hole, operated in vacuum. Inside the lenses a magnetic field is generated, which in turn is varied to focus or defocus the electron beam passing through the hole of the lens.

SEMs employ one to three condenser lenses to demagnify the electron-beam crossover diameter in the electron gun to a smaller size. The first and second condenser lenses control the amount of demagnification. Usually in the microscopes this is a single control labeled “spot size”, “condenser”, “C1” or “resolution”. The final lens in the column sometimes inappropriately called “objective” focuses the probe on the sample. The design of the lenses often incorporates space for the scanning coils, the stigmator, and the beam limiting aperture. The electron lenses can be used to magnify or demagnify the electron beam diameter, because their strength is variable, which results in a variable focal length. SEM always uses the electron lenses to demagnify the “image” of the emission source so that a narrow probe can be formed on the surface of the specimen. The aberrations of the final lens and consequently the resolution are controlled by a final lens aperture, which affects the beam convergence angle.

The final lens aperture has three important effects on the final probe. First there is an optimum aperture angle that minimizes aberrations. Second, the current in the final probe is controlled by the size of the aperture. Third, the probe convergence angle α controls the depth of field. Smaller α produces greater depth of field. Spot size in SEM is minimized at the expense of current.

The general approach in SEM is to minimize the probe diameter and maximize the probe current. The minimum probe diameter depends on the spherical aberration of the SEM electron optics, the gun source size, the electron optical brightness and the accelerating voltage.

The probe size, which directly effects resolution can be decreased by increasing the brightness. The electron optical brightness β is a parameter that is function of the electron gun performance and design. For all types of electron guns, brightness increases linearly with accelerating voltage,

so every electron source is 10 times as bright at 10 kV as it is at 1 kV. Decreasing the wavelength and the spherical aberration also decreases the probe size.

The lens defects (machining errors and asymmetry in lens winding), and contamination on aperture or column can cause the cross section of the electron beam profile to vary in shape. Generally, an elliptical cross section is formed rather than a circular one. As a result, during operation, the image will stretch along different direction at underfocus and overfocus condition. This imperfection on the electromagnetic lens is called astigmatism. A series of coils surrounding the electron beam, referred to as “stigmator,” can be used to correct astigmatism and achieve an image with higher resolution.

The astigmatism correction cycle (x-stigmator, focus, y-stigmator, focus) should be repeated, until ultimately the sharpest image is obtained. At that point the beam cross section will be focused to the smallest point. Generally the compensation for astigmatism is performed while operating at the increased magnification, which ensures the image quality of lower magnification even when perfect compensation is not obtained. However, the astigmatism is not obvious for low magnification observation.

Image Formation

The SEM image is a 2D intensity map in the analog or digital domain. Each image pixel on the display corresponds to a point on the sample, which is proportional to the signal intensity captured by the detector at each specific point (Figure 2.10). Unlike optical or transmission electron microscopes no true image exists in the SEM. It is not possible to place a film anywhere in the SEM and record an image. It does not exist. The image is generated and displayed electronically. The images in the SEM are formed by electronic synthesis, no optical transformation takes place, and no real or virtual optical images are produced in the SEM²⁶.

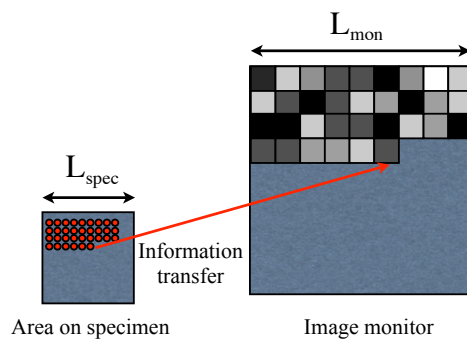


Figure 2.10: Image formation by SEM.

In an analog scanning system, the beam is moved continuously; with a rapid scan along the X-axis (line scan) supplemented by a stepwise slow scan along the Y-axis at predefined number of lines. The time for scanning a single line multiplied by the number of lines in a frame gives the frame time. In digital scanning systems, only discrete beam locations are allowed. The beam,

positioned in a particular location, remains there for a fixed time and then it is moved to the next point.

When the beam is focused on the specimen an analog signal intensity is measured by the detector. The voltage signal produced by the detector's amplifier is digitized and stored as discrete numerical value in the corresponding computer registry. Typically, the intensity is digitized into 8 bits (256 levels), 12 bits (4096) or 16 bits (65,536). The digital image is viewed by converting the numerical values stored in the computer memory into an analog signal for display on a monitor.

No optical transformation is responsible for image magnification in the SEM. Magnification is achieved by scanning an area on the specimen, which is smaller than the display. Since the monitor length is fixed, increase or decrease in magnification is achieved by respectively reducing or increasing the length of the scan on the specimen. For accurate magnification measurements a calibration is necessary.

Magnification in the SEM depends only on the excitation of the scan coils and not on the excitation of the objective lens, which determines the focus of the beam. The magnification of the SEM image is changed by adjusting the length of the scan on the specimen (L_{spec}) for a constant length of scan on the monitor (L_{mon}) (Figure 2.10), which gives the linear magnification of the image (M). The numerical value of magnification is determined by the ratio of the length of the monitor versus the length of the scan on the sample:

$$M = \frac{L_{mon}}{L_{spec}}$$

Topographic contrast includes all effects by which the shape and morphology of the specimen can be imaged. Vast majority of applications of the SEM involve studying shapes. Topographic contrast is the most important imaging mechanism. Topographic contrast arises because the number and trajectories of BS electrons and the number of SE depend on the angle of incidence between the beam and the specimen's surface. The angle of incidence varies because of the local inclination of the specimen. At each point struck by the beam, the number of BSE and SE detected gives direct information on the local inclination of the specimen. The interpretation of the images is intuitive and no knowledge of the mechanism of image formation is necessary. The topographic contrast actually observed depends on the detector used and its placement relative to the specimen and on the exact contribution BSE and SE detected.

Samples Preparation

The SEM column, gun, and specimen chambers all maintain a vacuum of 10^{-6} Torr or better for performance of the electron optics. High vacuum environments are alien to most forms of life due to the nearly 80% water content of cells and tissues. Even small biomolecules need a hydration shell to remain in a natural active state. This incompatibility of water rich specimens with the

electron microscope vacuum system necessitates a preparation of these samples devoiding it of all the fluids that would degas in high vacuum and contaminate the microscope. Therefore, all samples placed in a SEM must be dried of fluids in order to be stable for secondary electron imaging.

The strategy followed to preserve the structural features of organisms, organs, tissues, cells, and biomolecules is to chemically fix them into a rigid state with a cross-linkers and then load them with heavy metal salts to enhance the mass density of the components. Biological samples are first “fixed” with glutaraldehyde, a dialdehyde that contains five-carbon atoms. When this molecule is buffered and the biological sample is either perfused or immersed in it, it reacts with the N terminus of amino acids on adjacent proteins thereby releasing $2\text{H}_2\text{O}$ molecules and cross-linking the peptide chains. Thus, movement of all protein components of cells and tissues are prevented. Biological samples are then “postfixed” with osmium tetroxide that is believed to interact with the unsaturated fatty. Since OsO_4 contains the heaviest of all elements, it serves to add electron density and scattering properties to otherwise low contrast biological membranes. OsO_4 also serves as a mordant that interacts with itself and with other stains²⁹. Subsequent to fixation, the aqueous content of the sample is replaced with an intermediate fluid, usually an organic solvent such as ethanol or acetone before drying. The dehydration procedure uses ethanol or acetone in a graded series such as 50%, 75%, 95% and then several washes with pure 100% solvent. Caution should be exercised not to remove too much of the bulk fluid and expose the sample surface to air. A better method is a linear dehydration gradient that requires an exchange apparatus that slowly increases the intermediate fluid concentration^{30,31} and serves to reduce osmotic shock and shape change in the specimen. However, this method is not appropriate for high-resolution SEM of nanometer-sized structures since the drying procedure removes the hydration shell from bioorganic molecules that could thus collapse over the 1–10 nm range. The last step consists in coating the sample with a thin layer of metal; in the experiments reported in this thesis work few nanometres of gold sputtered in a saturated atmosphere of argon were used.

2.3 Immuno-fluorence assays

Immunofluorescence (IF) is a common assay commonly used in almost all fields of life science. This technique based on the pioneering work by Coons and Kaplan^{32,33}, and later by Mary Osborne³⁴, has been widely used both in research and clinical diagnostics. IF techniques can be used on both fresh and fixed samples. In IF, antibodies are chemically conjugated to fluorescent dyes such as fluorescein isothiocyanate (FITC) or tetramethyl rhodamine isothiocyanate (TRITC). These labeled antibodies bind (directly or indirectly) to the antigen of interest which allows for antigen detection through fluorescence techniques. The fluorescence can then be quantified using a flow cytometer, an array scanner or an automated imaging instrument, or visualized using fluorescence or confocal microscopy. The two main methods of

immunofluorescent labeling are direct and indirect.

In direct immunofluorescence the antibody against the molecule of interest is directly conjugated to a fluorescent dye. The advantages of this approach include shorter sample staining times and simpler multiple labeling procedures. When dealing with multiple antibodies raised in the same species, for example two mouse monoclonals, a direct labeling may be necessary. Among the possible drawbacks of direct immunofluorescence one can list: lower signals, generally higher cost, lack of flexibility and difficult labeling procedure when commercially labeled direct conjugates are unavailable.

In indirect immunofluorescence, the antibody specific for the molecule of interest (called the primary antibody) is unlabeled, and a second anti-immunoglobulin antibody directed toward the constant portion of the first antibody (called the secondary antibody) is tagged with the fluorescent dye (Figure 2.11). Indirect immunofluorescence has greater sensitivity compared to direct immunofluorescence. An amplification of the signal takes place in indirect immunofluorescence because more than one secondary antibody can bind to each primary (see Figure 2.11). Commercially produced secondary antibodies are relatively economic, available in an array of colors, and quality controlled. Disadvantages of indirect immunofluorescence include the potential for cross-reactivity and the need to find primary antibodies that are not raised in the same species or of different isotypes when performing multiple-labeling experiments. Samples with endogenous immunoglobulin may exhibit a high background.

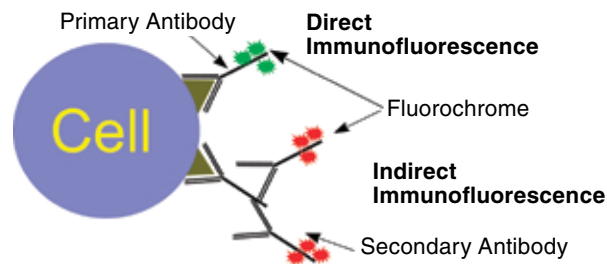


Figure 2.11: Schematic of direct and indirect immunofluorescence.

Fluorescence Microscopy

In this thesis we have observed both the direct and indirect immunofluorescence. Imaging was performed using a microscope Nikon Eclipse i80. The basic function of a fluorescence microscope is to irradiate the specimen with a specific wavelength, and then to separate the weaker emitted fluorescence from the excitation light. In a properly configured microscope, only the emission light should reach the eye or detector so that the resulting fluorescent structures are superimposed with high contrast against a very dark background. The limits of detection are generally governed by the darkness of the background, and the excitation light is typically several hundred thousands to a million times brighter than the emitted fluorescence.

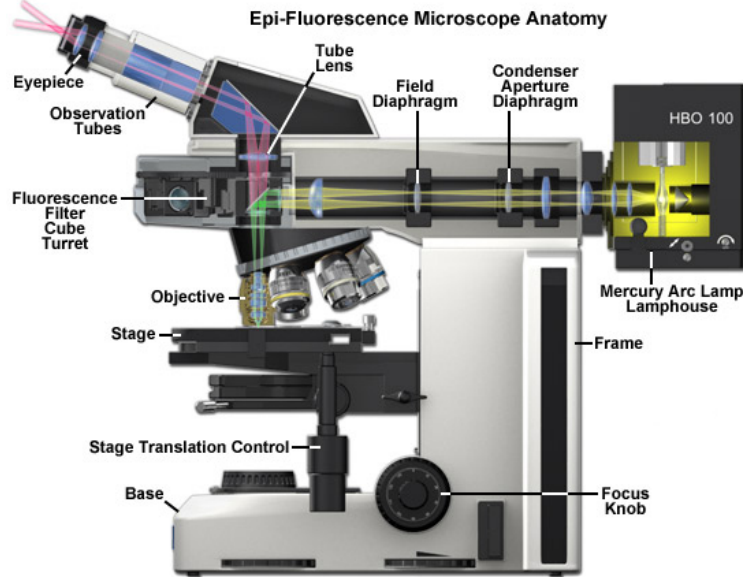


Figure 2.12: Schematic representation of Epi-Fluorescence Microscope

A schematic representation of the epi-fluorescence microscope is illustrated in figure 2.12. The vertical illuminator in the center of the diagram has the light source positioned at one end labeled the Mercury Arc Lamp lamphouse and the filter cube turret at the other. The design consists of a basic reflected light microscope in which the wavelength of the reflected light is longer than that of the excitation. Johan S. Ploem is credited with the development of the vertical illuminator for reflected light fluorescence microscopy. In a fluorescence vertical illuminator, light of a specific wavelength (or defined band of wavelengths), often in the ultraviolet, blue or green regions of the visible spectrum, is produced by passing multispectral light from an arc-discharge lamp or other sources through a wavelength selective excitation filter. Wavelengths passed by the excitation filter reflect from the surface of a dichromatic (also termed a dichroic) mirror or beamsplitter, through the microscope objective and reach the specimen with intense light. If the specimen fluoresces, the emission light gathered by the objective passes back through the dichromatic mirror and is subsequently filtered by a barrier (or emission) filter, which blocks the excitation wavelengths. It is important to note that in fluorescence microscopy specimen, subsequent to excitation, produces its own light. The emitted light re-radiates spherically in all directions, regardless of the excitation light source direction.

Limitations of IF Techniques

Photobleaching as with most fluorescence techniques, a relevant problem of immunofluorescence is photobleaching (and phototoxicity). Photobleaching is the photochemical destruction of a fluorophore due to the generation of reactive oxygen species in the specimen as a byproduct of fluorescence excitation. Photobleaching can be minimized by: (a) decreasing the excitation light in both intensity and duration, (b) reducing the availability of singlet oxygen by the addition of singlet oxygen scavengers (= antifade reagents), and (c) using a low concentration of

fluorochromes with high-quantum efficiency.

Autofluorescence: Biological autofluorescence in mammalian cells, due to flavin coenzymes and reduced pyridine nucleotides, can be problematic in the detection of fluorescence probes in tissues and cells. Fixation with aldehydes, particularly glutaraldehyde, can result in high levels of autofluorescence. This can be minimized in fixed cells by washing with 0.1% sodium borohydride in phosphate-buffered saline³⁵ prior to antibody incubation. Issues due to autofluorescence can be minimized by selecting probes and optical filters that maximize the fluorescence signal relative to the autofluorescence.

Fluorescence Overlap: one of the problems that must be dealt with when measuring fluorescence of more than one color is the possibility that the emission signals overlap. It is thus necessary to remove the overlapping signal or it will give a false level for one or more colors. If band-pass optical filters will allow photons within this overlapping range to reach the detector these must be electronically removed otherwise the measurement for each detector will overestimate the actual signal. This process is called fluorescence compensation and can be automatically calculated in many detection systems using single positive controls.

Samples Preparation

In this thesis, we used two immunofluorescence protocols: Actin Cytoskeleton and Focal Adhesion Staining (to investigate the adhesion of cells on the fabricated scaffolds) and β -III Tubulin Antibody Staining (to mark the network of neuronal cells from stem).

Actin Cytoskeleton and Focal Adhesion Staining Protocol

The actin cytoskeleton is a highly dynamic network composed of actin polymers and a large number of associated proteins. The function of the actin cytoskeleton is to mediate essential biological functions in all eukaryotic cells, including intra- and extra-cellular movement and structural support. To perform these functions, the organization of the actin cytoskeleton must be tightly regulated both temporally and spatially^{36,37}. The actin cytoskeleton is a dynamic structure that rapidly changes shape and organization in response to stimuli and cell cycle progression. Orientational distribution of actin filaments within a cell is, therefore, an important determinant of cellular shape and motility. Focal adhesion and adherens junctions are membrane-associated complexes that serve as nucleation sites for actin filaments and as cross-linkers between the cell exterior, plasma membrane and actin cytoskeleton³⁸. The function of focal adhesions is structural, linking the extracellular matrix outside the cells to the actin cytoskeleton inside. They are also sites of signal transduction, initiating signaling pathways in response to adhesion. Focal adhesions consist of integrin-type receptors that are attached to the extracellular matrix and are intracellularly associated with protein complexes containing vinculin (universal focal adhesion marker), talin, alpha-actinin, paxillin, tensin and focal adhesion kinase^{39,40}. During these immunofluorescence protocols we have also always stained the cell nuclei with 4',6-diamidino-2-phenylindole (DAPI) to get a more clear information about the cell shape and status. DAPI is a

fluorescent stain extensively used in fluorescence microscopy that binds strongly to A-T rich regions in DNA. It can pass through an intact cell membrane therefore it can be used to stain both live and fixed cells⁴¹. In the immunofluorescence assays reported here the marked targets were: the focal adhesion proteins using antibodies against vinculin, cytoskeletal elements by the TRITC-conjugated Phalloidin and nuclei by DAPI. The detailed steps of the protocol are the following:

1. Fix cultured cells with 4% paraformaldehyde in 1x PBS for 15-20 minutes at room temperature.
2. Wash twice with 1x washing buffer.
3. Permeabilize cells with 0.1% Triton X-100 in 1x PBS for 1-5 minutes at room temperature.
4. Wash twice with 1x washing buffer.
5. Apply blocking solution for 30 minutes at room temperature.
6. Dilute primary antibody (Anti-Vinculin) to a working concentration in blocking solution, and incubate for 1 hour at room temperature.
7. Wash three times (5-10 minutes each) with 1x washing buffer.
8. Dilute secondary antibody in 1x PBS just before use and incubate for 30-60 minutes at room temperature. For double labeling TRITC- conjugated Phalloidin can be incubated simultaneously with the secondary antibody for 30-60 minutes at room temperature.
9. Wash three times (5-10 minutes each) with 1x wash buffer.
10. Following this washing step, nuclei counterstaining can be performed by incubating cells with DAPI for 1-5 minutes at room temperature, followed by washing cells three times (5-10 minutes each) with 1x wash buffer.

Fluorescence images can then be visualized with a fluorescence microscope.

β -Tubulin III Antibody Staining

Tubulins, the major components of cellular cytoskeleton, form microtubules that are critical for cellular structure, migration, cell division, and intracellular trafficking. There are at least three types of tubulins: alpha, beta, and gamma. Each has a molecular weight of approximately 55 kDa. Microtubules are large structures (30 nm in diameter) composed of alternating alpha and beta subunits. Compounds that block microtubule formation, such as Taxol and the vinca alkaloids, inhibit cell division and are effective anti-cancer agents. Class III β -tubulin is a microtubule element expressed exclusively in neurons, and is a popular marker specific for this kind of cells. It contributes to microtubule stability in neuronal cell bodies and axons, and plays a role in axonal growth^{42,43}. The detailed steps of the staining protocol are:

1. Fix cultured cells with 4% paraformaldehyde in 1x PBS for 15-20 minutes at room temperature.
2. Wash twice with 1x washing buffer.

3. Permeabilize cells with 0.1% Triton X-100 in 1x PBS for 1-5 minutes at room temperature.
4. Wash twice with 1x washing buffer.
5. Apply blocking solution for 30 minutes at room temperature.
6. Dilute primary antibody (Anti- β -Tubulin III) to the working concentration in blocking solution, and incubate for 1 hour at room temperature.
7. Wash three times (5-10 minutes each) with 1x wash buffer.
8. Dilute secondary antibody (Alexa fluor 594) in 1x PBS just before using and incubate for 30-60 minutes at room temperature.
9. Wash three times (5-10 minutes each) with 1x washing buffer.
10. Following this washing step, nuclei counterstaining can be performed by incubating cells with DAPI for 1-5 minutes at room temperature, followed by washing cells three times (5-10 minutes each) with 1x washing buffer.

Fluorescence images can then be visualized with a fluorescence microscope.

2.4 Atomic Force Microscopy

The last microscopy technique used during this thesis work is Scanning Probe Microscopy and in particular Atomic Force Microscopy (AFM). The principles of AFM are herein briefly described. An atomically sharp tip placed at the end of a soft cantilever is scanned over a surface. The interaction force between the tip and the sample is measured by mean of the deflection of the cantilever, a feedback loop enables the piezoelectric scanner to maintain a constant tip-sample force (to obtain height information), or constant tip height (to obtain force information) above the sample surface. The piezoelectric effect is the well known generation of a potential difference across the opposite faces of specific non-conducting crystals as a result of the application of stresses and it is highly sensitive. The electrical polarization produced is proportional to the stress. The polarization changes sign if the stress changes from compression to tension. The reverse piezoelectric effect, the opposite phenomenon, is the one employed by the AFM scanners. The opposite faces of a piezoelectric crystal are subject to a potential difference, inducing a change of shape of the crystal⁴⁴. The AFM head includes an optical detection system. A diode laser is focused onto the rear side of a reflective cantilever. As the tip scans the surface of the sample, the laser beam is reflected by the cantilever into a dual element photodiode. The photodetector thus measures the vertical deflection of the cantilever by measuring the difference in light intensities between the upper and lower photodetectors. Feedback from the photodiode difference signal, through software control from the computer, enables the tip to maintain either a constant force or constant height above the sample. In the constant force mode the piezoelectric transducer monitors in real time the tip-sample interaction force and keeps it constant changing the sample vertical position by the piezoelectric scanner. In this work a Smena Scanning Probe Microscopy (Figure 2.13b) consisting of stand alone head, where the piezo scanner is positioned

inside the head has been used. The geometry of the piezo consists of three blocks of piezoelectric ceramic, allowing the movement of the tip along the three orthogonal directions x , y , z .

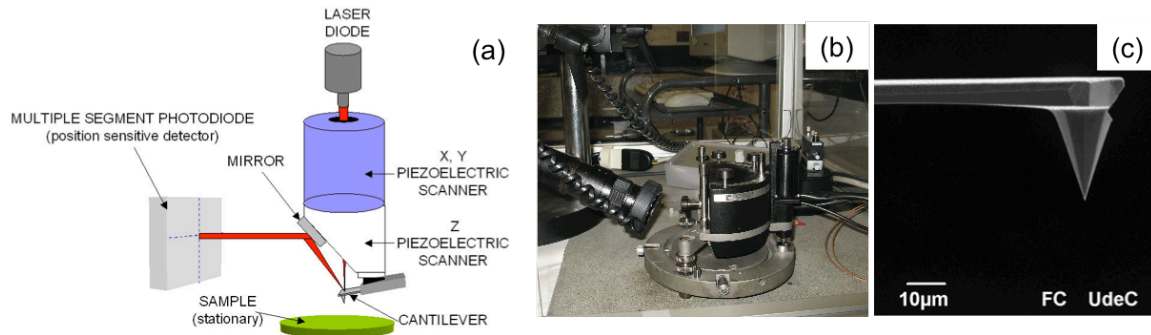


Figure 2.13: (a) Schematic representation of AFM equipment. (b) NT-MDT™ Smena Standalone head (Institute for the study of Nanostructured Materials, CNR-Bologna, Italy), (c) Image of cantilevers taken by Scanning Electron Microscope.

Probes

The first and most important part of the AFM is the probe that locally sense the interaction force; an electron micrograph of an AFM tip is shown in the figure 2.13c. The tip consists of a micro-fabricated, extremely sharp spike mounted at the end of a cantilever. The sharpness of the spike determines the resolving power of the instrument. The cantilever on which it is mounted allows the tip to move up and down as it is scanned over the sample. The tips used in this work, are distributed by Molecular Devices and Tools for Nanotechnology (NT-MDT). The cantilever typically has a very low force constant enabling the AFM to measure and control with great precision very small forces between the tip and the sample. The cantilever-tip assembly is generally made of silicon or silicon nitrate, these materials being hard, and resistant, and thus ideally suited for micro-fabrication. In the literature it has been shown how AFM tips can be functionalized, thus both the physical-chemical properties of their surface can be changed and specific bio-probes can be fabricated by immobilizing biological molecules onto them.

Modes of operation

The dominant interactions at short probe-sample distances in the AFM are Van der Waals (VdW) interactions. However long-range interactions (i.e. capillary, electrostatic, magnetic) are also relevant further away from the surface. The latter are important in other SPM modes of operation and analysis. In contact with the sample, the probe predominately experiences repulsive Van der Waals forces (contact mode). This leads to the cantilever positive deflection. As the tip moves away from the surface attractive Van der Waals forces become dominant (non-contact mode) Figure 2.14 and the cantilever deflect in the negative direction.

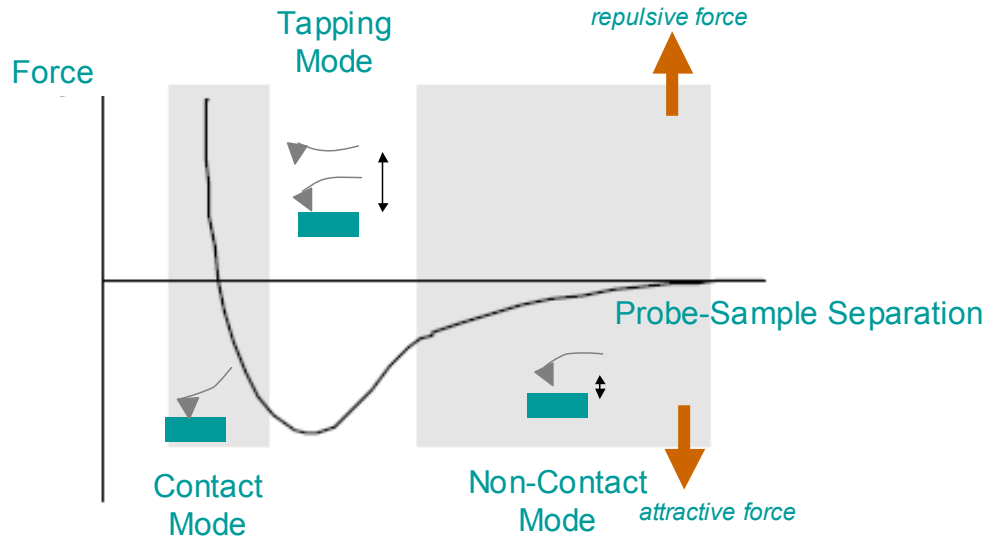


Figure 2.14: Plot of force as a function of probe-sample separation.

Contact Mode AFM: (repulsive VdW) When the spring constant of cantilever is smaller than the surface one the cantilever bends. The force on the tip is thus repulsive. By maintaining a constant cantilever deflection (using the feedback loops) the force between the probe and the sample remains constant and an image of the surface is obtained. Advantages: faster scanning, friction analysis, good for rough samples. Disadvantages: the mechanical load can damage/deform soft samples (however imaging in liquids often resolves this issue).

Intermittent Mode (Tapping): The imaging is similar to contact but in this mode the cantilever is oscillated at its resonant frequency. The probe lightly “taps” on the sample surface during scanning, touching the surface at the bottom of its swing. By maintaining constant oscillation amplitude a constant tip-sample interaction is maintained and an image of the surface is obtained. Advantages: allows high resolution of soft samples that can be easily damaged and/or loosely held to a surface; good for biological samples. Disadvantages: more challenging to image in liquids, slower scan speeds needed.

Non-contact Mode: (attractive VdW) The probe does not touch the sample surface, it oscillates above the adsorbed fluid layer on the surface during scanning. Using a feedback loop to monitor changes in the amplitude due to attractive VdW forces the surface topography can be measured. Advantages: very low force exerted on the sample, extended probe lifetime. Disadvantages: generally lower resolution; contaminant layer on surface can interfere with oscillation.

Image types

Several image types we can be obtained during a single scan; in this work we collected the following:

Topographical: This is by far the most common way of recording images using the AFM. The information used by the instrument software to create an image is simply the vertical movements of the piezoelectric tube. Ideally the whole scan should be performed with a constant applied

force, i.e. a constant deflection or a constant oscillation amplitude of the cantilever, and the way of compensating for any variation due to the local topography is to move the sample or tip up and down via the piezoelectric tube. From this type of image it is possible to measure the heights of object in the image.

Phase: Phase is a quantity that can be recorded in the AC modes such as intermittent contact or non-contact mode. In those modes the control loop uses the drop in amplitude of the oscillating cantilever to determine the vertical movement of the piezoelectric tube. When the tip actually strikes the sample, its phase of oscillation is disturbed and it is no longer precisely in the step with the phase of the electrical oscillator that is driving it. This is principally because each time the tip strikes the sample, it transfers a small amount of energy to it. A reasonable level of contrast in a phase image is primarily dependent on the presence of two component in the sample with sufficiently different viscoelastic properties.

Image artifact

Several image artifacts can come from AFM imaging, the most common is known as a 'double tip'. The sharp point at the very apex of the tip can sometimes be accompanied by other asperities, usually result of damage or contamination. In theory there can be any number of extra tips but, in the majority of cases, no more than a total of two are actually observed. This produces two copies of the image, offset by distance equal to the gap between the tips. Whilst this sounds like a serious source of artifact, it is reassuringly easy to determine when a double tip is present because the image adopts an obvious symmetry. If the double tip is caused by contamination it can sometimes be rectified by scanning over a large area at high speed. This can mechanically remove the contaminants, improving the subsequent images⁴⁴.

2.5 Cell culture

In this thesis, we studied adhesion, proliferation and differentiation of four cell lines (NIH-3T3, 1321N1, SH-SY5Y and NE-4C) in response to external signals, including chemical and topographical signals, and they are specific to the scaffold.

NIH-3T3 mouse embryonic fibroblast cells come from a cell line isolated and initiated in 1962 at the New York University School of Medicine Department of Pathology. The NIH-3T3 (Cell Biolabs, Inc. AKR-214) cells are established from a NIH Swiss mouse embryo. The NIH-3T3 were cultured in Dulbecco's modified Eagle Medium (high glucose), 10% fetal bovine serum, 0.1mM non-essential amino acids, 2mM L-glutamine, 1% streptomycin and 10 μ g ml⁻¹ Blasticidin⁴⁵.

1321N1 is a human astrocytoma cell line isolated in 1972 as a sub clone of the cell line 1181N1 which in turn was isolated from the parent line U-118 MG (one of a number of cell lines derived from malignant gliomas by J Ponten). 1321N1 has been shown to have very similar STR profile data to U-118 MG. 1321N1 cells (purchased from ECACC no. 86030402) were cultured in

Dulbecco's modified Eagle medium: nutrient mixture F-12, supplemented with 10% fetal bovine serum, 2mM L-glutamine, 100Uml⁻¹ penicillin and 100µg ml⁻¹ streptomycin.

NE-4C cells were cloned from primary brain cell cultures prepared from the fore- and midbrain vesicles of 9-day-old transgenic mouse embryos lacking functional p53 tumor suppressor protein. The NEuroectodermal NE-4C cells divide continuously if maintained under normal tissue culture conditions and display several characteristics of neural stem cells, such as nestin and SSEA1 immunoreactivity, self renewal and differentiation into distinct neural cell types upon appropriate induction. Cell culture maintenance of the murine neural NE-4C stem cell line were carried out according to the published protocol⁴⁶. The cells were cultured in Minimum Essential Medium Eagle containing 10% FBS, 4 mM glutamine, 40 mg ml⁻¹ gentamicin and 2.5 mg ml⁻¹ amphotericin.

SH-SY5Y is a thrice-cloned sub-line of bone marrow biopsy-derived line SK-N-SH (Sigma catalogue no. 86012802). SH-SY5Y has dopamine-β-hydroxylase activity and can convert glutamate to the neurotransmitter GABA. Will form tumours in nude mice in approximately 3-4 weeks. The loss of neuronal characteristics has been described with increasing passage numbers⁴⁷. The base medium for this cell line is a 1:1 mixture of Dulbecco's modified Eagle Medium (high glucose) and nutrient mixture F-12, supplemented with 10% fetal bovine serum, 2mM L-glutamine, 100Uml⁻¹ penicillin and 100 µg ml⁻¹ streptomycin.

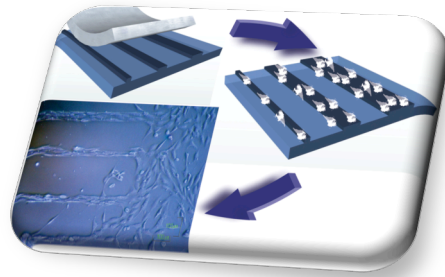
All cell lines were incubated under the standard cell culture conditions (37°C, 5% CO₂ and 95% relative humidity).

Bibliography

- 1 Hudson, T. J. *et al.* An STS-based map of the human genome. *Science* **270**, 1945-1954, (1995).
- 2 Stephen A. Chervitz, L. A., Gavin Sherlock, Catherine A. Ball, Eugene V. Koonin, Selina S. Dwight, Midori A. Harris, Kara Dolinski, Scott Mohr, Temple Smith, Shuai Weng, J. Michael Cherry and David Botstein. Comparison of the Complete Protein Sets of Worm and Yeast: Orthology and Divergence. *Science* **282**, 2022-2028, (1998).
- 3 Adams, M. D. *et al.* The genome sequence of *Drosophila melanogaster*. *Science* **287**, 2185-2195, (2000).
- 4 Fodor, S. P. A. *et al.* Light-Directed, Spatially Addressable Parallel Chemical Synthesis. *Science* **251**, 767-773, (1991).
- 5 Lam, K. S. *et al.* A New Type of Synthetic Peptide Library for Identifying Ligand-Binding Activity. *Nature* **354**, 82-84, (1991).
- 6 Westin, L. *et al.* Anchored multiplex amplification on a microelectronic chip array. *Nat Biotechnol* **18**, 199-204, (2000).
- 7 Schena, M., Shalon, D., Davis, R. W. & Brown, P. O. Quantitative monitoring of gene expression patterns with a complementary DNA microarray. *Science* **270**, 467-470, (1995).

- 8 Lockhart, D. J. *et al.* Expression monitoring by hybridization to high-density oligonucleotide arrays. *Nat Biotechnol* **14**, 1675-1680, (1996).
- 9 Chen, C. S., Mrksich, M., Huang, S., Whitesides, G. M. & Ingber, D. E. Geometric control of cell life and death. *Science* **276**, 1425-1428, (1997).
- 10 James, C. D. *et al.* Patterned protein layers on solid substrates by thin stamp microcontact printing. *Langmuir* **14**, 741-744, (1998).
- 11 Singhvi, R. *et al.* Engineering Cell-Shape and Function. *Science* **264**, 696-698, (1994).
- 12 Xia, Y. N. & Whitesides, G. M. Soft lithography. *Annu Rev Mater Sci* **28**, 153-184, (1998).
- 13 Xia, Y. N. *et al.* Complex optical surfaces formed by replica molding against elastomeric masters. *Science* **273**, 347-349, (1996).
- 14 Zhao, X. M., Xia, Y. N. & Whitesides, G. M. Soft lithographic methods for nanofabrication. *J Mater Chem* **7**, 1069-1074, (1997).
- 15 Cavallini, M. & Biscarini, F. Nanostructuring conjugated materials by lithographically controlled wetting. *Nano Lett* **3**, 1269-1271, (2003).
- 16 Cavallini, M., Gentili, D., Greco, P., Valle, F. & Biscarini, F. Micro- and nanopatterning by lithographically controlled wetting. *Nat Protoc* **7**, 1668-1676, (2012).
- 17 McDonald, J. C. & Whitesides, G. M. Poly(dimethylsiloxane) as a material for fabricating microfluidic devices. *Accounts of chemical research* **35**, 491-499, (2002).
- 18 Chaudhury, M. K. & Whitesides, G. M. Correlation between surface free energy and surface constitution. *Science* **255**, 1230-1232, (1992).
- 19 Lahiri, J., Ostuni, E. & Whitesides, G. M. Patterning ligands on reactive SAMs by microcontact printing. *Langmuir* **15**, 2055-2060, (1999).
- 20 Campana, A. *et al.* Facile maskless fabrication of organic field effect transistors on biodegradable substrates. *Appl Phys Lett* **103**, (2013).
- 21 P.-G. de Gennes, F. B.-W., D. Quere., *Capillarity and Wetting Phenomena: Drops, Bubbles, Pearls, Waves.* (Springer, 2004).
- 22 Kim, E., Xia, Y. & Whitesides, G. M. Polymer microstructures formed by moulding in capillaries. *Nature* **376**, 581-584, (1995).
- 23 Kim, E. & Whitesides, G. M. Imbibition and flow of wetting liquids in noncircular capillaries. *J Phys Chem B* **101**, 855-863, (1997).
- 24 Huang, W. F., Liu, Q. S. & Li, Y. Capillary filling flows inside patterned-surface microchannels. *Chem Eng Technol* **29**, 716-723, (2006).
- 25 Davidson M. W. & A., M. *Encyclopedia of Imaging Science and Technology.* (2002).
- 26 Well O. C. *Scanning Electron Microscopy.* (McGraw-Hill, 1974).
- 27 Wischnitzer, S. *Introduction to Electron Microscopy.* (Pergamon Press, 1970).
- 28 Goldstein, D. N., D. Joy, C. Lyman, P. Echlin, E. Lifshin, L. Sawyer, and J. Michael, . *Scanning Electron Microscopy and X-Ray Microanalysis, 3rd edn* (Kluwer Academic/Plenum Publishers, , 2003).
- 29 Tanaka, K., Mitsushima, A., Kashima, Y., Nakadera, T. & Osatake, H. Application of an ultrahigh-resolution scanning electron microscope (UHS-T1) to biological specimens. *Journal of electron microscopy technique* **12**, 146-154, (1989).
- 30 Peters, K. R. Improved handling of structural fragile cell-biological specimens during electron microscopic preparation by the exchange method. *Journal of microscopy* **118**, 429-441, (1980).

- 31 Apkarian, R. & Curtis, J. C. SEM cryofracture study of ovarian follicles of immature rats. *Scanning electron microscopy* **4**, 165-172, (1981).
- 32 Coons aH, e. a. Immunological properties of an antibody containing a fluorescent group. . *Proc Soc exp Biol Med* **47**, 200-202, (1941).
- 33 MH, C. a. a. K. Localization of antigen in tissue cells. . *Journal of exp Med* **91**, (1950).
- 34 Weber K, e. a. Specific visualization of tubulin-containing structures in tissue culture cells by immunofluorescence. Cytoplasmic microtubules, vinblastine-induced paracrystals, and mitotic figures. . *Cell Res* **95**, 111-120, (1975).
- 35 Bacallao R, e. a. *Guiding principles of specimen preservation for confocal fluorescence microscopy. I.* (J.B. Pawley. ed, 2006).
- 36 Dubreuil, R. R. Structure and Evolution of the Actin Cross-Linking Proteins. *Bioessays* **13**, 219-226, (1991).
- 37 Matsudaira, P. Modular Organization of Actin Cross-Linking Proteins. *Trends Biochem Sci* **16**, 87-92, (1991).
- 38 Yamada, K. M. & Geiger, B. Molecular interactions in cell adhesion complexes. *Curr Opin Cell Biol* **9**, 76-85, (1997).
- 39 Turner CE, B. K. Transmembrane molecular assemblies in cell-extracellular matrix interactions. *Curr Opin Cell Biol* **3**, 849-853, (1991).
- 40 Burridge, K. *et al.* Actin Membrane Interaction in Focal Adhesions. *Cell Differ Dev* **32**, 337-342, (1990).
- 41 Kapuscinski, J. Dapi - a DNA-Specific Fluorescent-Probe. *Biotech Histochem* **70**, 220-233, (1995).
- 42 Zachariah, R. M., Olson, C. O., Ezeonwuka, C. & Rastegar, M. Novel MeCP2 Isoform-Specific Antibody Reveals the Endogenous MeCP2E1 Expression in Murine Brain, Primary Neurons and Astrocytes. *Plos One* **7**, (2012).
- 43 Galan, L. *et al.* Subventricular zone in motor neuron disease with frontotemporal dementia. *Neurosci Lett* **499**, 9-13, (2011).
- 44 Gunning, A. K. a. A. *Atomic Force Microscopy for Biologists.* . (2004).
- 45 J, T. G. & H, G. Quantitative studies of the growth of mouse embryo cells in culture and their development into established lines. . *J. Cell Biol.* **17**, 299-313, (1963).
- 46 Jelitai, M., Anderova, M., Chvatal, A. & Madarasz, E. Electrophysiological characterization of neural stem/progenitor cells during in vitro differentiation: study with an immortalized neuroectodermal cell line. *J. Neurosci. Res.* **85**, 1606-1617, (2007).
- 47 Biedler, J. L., Helson, L. & Spengler, B. A. Morphology and growth, tumorigenicity, and cytogenetics of human neuroblastoma cells in continuous culture. *Cancer Res.* **33**, 2643-2652, (1973).



Chapter 3

Neural cell alignment by patterning gradients of extracellular matrix protein: a laminin 2D scaffold

In this chapter the fabrication of a 2D scaffold is reported. Surface of polystyrene TC dishes were patterned with human laminin without any previous chemical and physical modification of the surface properties to achieve accurate cell guidance. Micro Molding in Capillaries (MIMICs) was applied to transfer the protein pattern onto the surface. Immunofluorescence analysis of the patterned laminin shows a decreasing gradient of concentration along the longitudinal direction of the stripes indicating that the protein concentration decreases from the entrance of the channels in contact with the reservoir towards the end. Neural cells were randomly seeded and shown to selectively adhere to the pattern. In the control experiment, cells on the unpatterned laminin film exhibited no preferential orientation. This implies that the anisotropy of laminin stripes is an effective chemical stimulus for cell recruiting and alignment. Quantification of the response of neural cells to gradients of guidance cues is an important issue. We propose a quantitative assessment of the effect of laminin gradients based on the immunofluorescence and optical microscopy images, to demonstrate that the patterning method indeed yields selective confinement and guidance of neural cell proliferation onto the surface, and affects the spatial organization of the cells¹.

3.1 Introduction

Cell adhesion, proliferation and recruitment, tissue growth onto technological surfaces are central phenomena in medical applications and biomedical devices, including tissue engineering, stem-cell-based therapies, biosensing and drug screening²⁻⁵. Cells respond to a variety of stimuli: topographical, physical, electrical, mechanical and chemical, both short and long ranged, cooperating over multiple length scales⁶⁻¹¹. Smooth gradients of proteins or peptides from the extracellular matrix (ECM) as well as soluble factors such as growth factors and chemokines, are known to affect adhesion, migration, proliferation and differentiation of different cell types¹²⁻¹⁸.

We designed and fabricated a multiscale gradient of laminin by soft lithography. We chose laminin (Figure 3.1), because is a key protein in the basal lamina which is the protein network foundation for most cells and organs. Laminins are trimeric proteins that contain a α -chain, a β -chain, and a γ -chain, found in five, four, and three genetic variants, respectively. The

trimeric proteins intersect to form a cross-like structure that can bind to other cell membrane and extracellular matrix molecules¹⁹. The three shorter arms are particularly important to bind to other laminin molecules and thus to form layers. The long arm is binding to cells and it helps the anchoring of organized tissue cells to the membrane. Laminins are an important and biologically active part of the basal lamina, influencing cell differentiation, migration, and adhesion, as well as phenotype and survival²⁰.

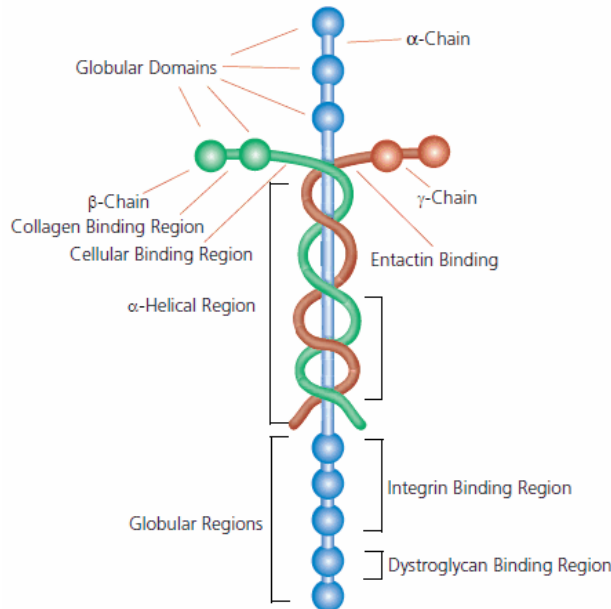


Figure 3.1: The structure of Laminin (from Molecular Biology of the Cell).

The substrate chosen for this work is the polystyrene (PS), a thermoplastic aromatic polymer with a linear structure widely used for manufacturing cell culture dishes. At room temperature PS is a glassy solid; above its glass transition temperature $T_g \approx 100^\circ\text{C}$, PS acquires plasticity and it is capable of flowing (e.g. in moulding/extrusion processes); PS begins to degrade at a temperature of 270°C . PS is chemically inert with respect to many corrosive agents, and soluble in chlorinated organic solvents (such as dichloromethane and chloroform), in acetone and in some aromatic solvents such as benzene and toluene²¹. PS is used for many applications thanks to its mechanical and electrical properties. In particular, PS is the most common material used for cell culture *in vitro*. The polystyrene plastic tissue culture (TC) dishes are chemically treated to increase the adhesion of cells²², because the non-adhesive nature of polystyrene^{23,24}. In this work we have used PS plates not chemically treated that do not favour the adhesion of cells.

Human astrocytoma 1321N1 cells were chosen in the frame of neural cells because they display very good adhesion and migration thus are suitable for assessing the effect of a surface modification such as the presence of laminin gradients on their adhesion and orientation.

3.2 Fabrication and characterization of laminin patterns

Human laminin (Sigma-Aldrich) was patterned on the surface of commercial polystyrene TC dishes (Corning, Sigma-Aldrich) by MIMICs. Polydimethylsiloxane (PDMS) stamps were prepared by replica moulding of a master fabricated as reported in chapter 2. The PDMS stamp has 22 parallel channels, whose length and height are 1.5µm is 8mm, and whose width and spacing ranges from 15 to 70µm, and 160 and 230µm respectively. The PDMS stamp was placed on the substrate surface and adhered by soft pressure on the top. A droplet (5µl volume) of laminin solution (20µg ml⁻¹ in cell culture medium without serum) poured at an open end of the channels filled the channels upon the action of Laplace pressure. Upon the complete evaporation of the medium (2h, RT), the stamp is gently peeled-off, leaving a pattern of laminin deposited on the polystyrene surface. Immunofluorescence assays (see Chapter 2) were performed to visualize the local distribution of laminin on the substrate and evaluate the occurrence of stable functional binding. To assess the stability of the protein pattern, some samples were incubated in the presence of the cell culture medium under standard cell culture conditions (37°C, 5% CO₂, humidified atmosphere) for at least 24h before performing immunofluorescence assays.

In figure 3.2, a description of the surface patterning using MIMICs is reported. The principle of this soft lithography technique is illustrated in figure 3.1a, and the mask layout used for stamp replica moulding is shown in figure 3.1b. The length scales of the pattern were chosen because they match the characteristic size of a neural cell such as the glial cell line used in these experiments (*ca* 10µm). The laminin patterns have been imaged by a combination of optical, fluorescence and scanning probe microscopies (Figure 3.1c, d and e, respectively). The laminin stripes reproduce the motif and the lateral sizes of the stamp channels (Figure 3.1c,d). The maximum height of the protein stripes, upon fabrication, was approximately 1.5µm as evidenced by the SPM image profile analysis (Figure 3.1e), and stripe widths vary consistently with the lateral size of the stamp channels. The immunofluorescence assays performed after 24 h of incubation in cell culture medium show that the laminin pattern remains stable under cell culture conditions (Figure 3.1d), indicating a good absorption of the protein onto the surface. The specificity of fluorescence labelling is demonstrated by the absence of fluorescence signals between the stripes and in control samples incubated in the absence of the primary anti-laminin antibody. The recognition of epitopes of laminin molecules by anti-laminin antibody indicates that laminin retains its conformational structure upon absorption onto the plastic surface.

These results demonstrated that MIMICs is a suitable method to fabricate a stable laminin pattern onto TC dishes, with no need of grafting or chemically modifying the substrate.

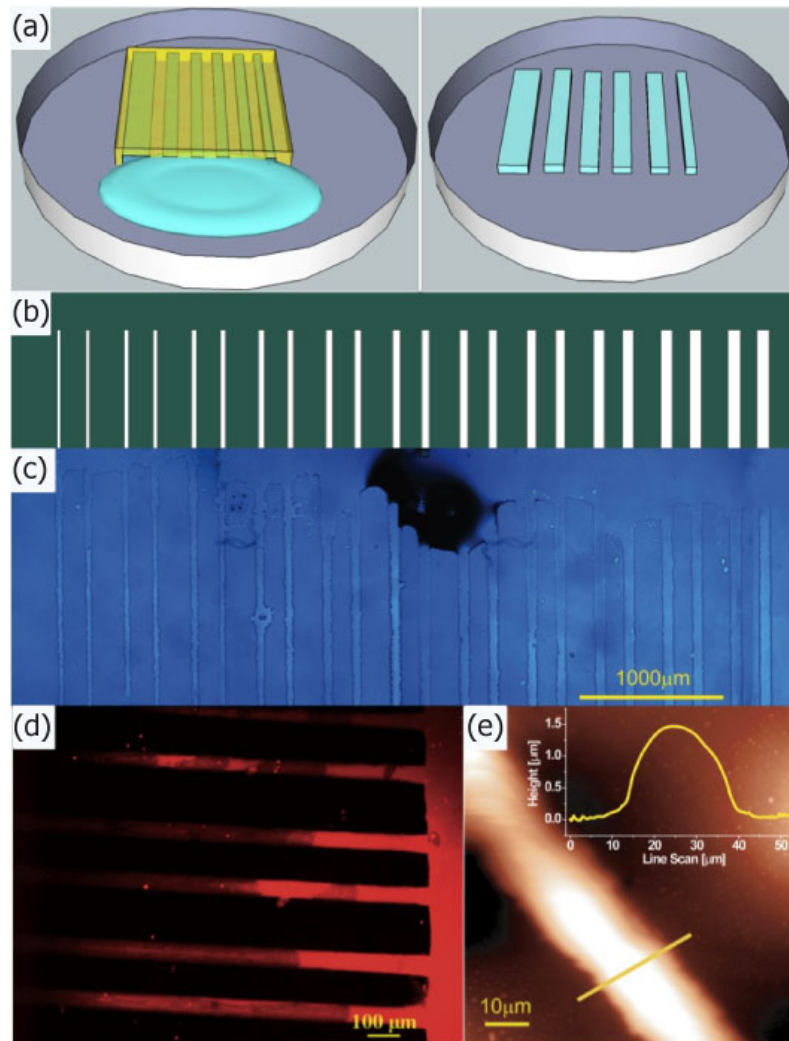


Figure 3.2: Patterning laminin on polystyrene TC dishes. (a) Schematic drawing of MIMICs; (b) layout of the mask used for lithography: white lanes represent the channels at increasing widths (c) optical (d) immunofluorescence and (e) scanning probe micrographs with line profile (inset) of the patterned laminin stripes.

3.3 Analysis of patterned protein gradients

In order to quantify the concentration gradient of laminin on polystyrene TC dishes along the patterned stripes, surface density analysis from fluorescence images was performed. Fluorescence pixel intensity values were estimated for all captured images with the software GIMP v. 2.6.7 (GNU image manipulation program; Spencer Kimball, Peter Mattis) by using the function histogram luminosity that exploits *K*-means clustering. The analysis was performed by subdividing each stripe length into longitudinal regions 10 μ m long (comparable with the average dimension of a neural cell) and variable widths corresponding to the lateral channel dimension. The pixel intensity unit was normalized, 100% represents the highest intensity on the substrate, and 0% corresponds to no fluorescence signal. The fluorescence intensity carries information about the local amount of the protein adsorbed onto the surface²⁵.

Gradient analysis was performed for each stripe as follows: the normalized fluorescence intensity was plotted against the relative position along each stripe. The monotonic decrease of the fluorescence intensity versus the distance from the channel entrance, as depicted in the representative result in figure 3.3 (black dots), evidences the laminin gradient formation.

We observed that the decrease of the fluorescence intensity along each stripe exhibits a double exponential decay: the first one accounting for the steeper slope (k_2) at distances approximately up to $100\mu\text{m}$, the latter (k_1) for the milder decreases at distances larger than $100\mu\text{m}$. We extracted the two parameters characterizing the decays for each stripe width and we plotted them in the graph of figure 3.4. The mean values for the inverse of decay length accounting for large distances and corresponding to $k_1 = -0.0013 (\pm 0.0003) \mu\text{m}^{-1}$ do not significantly change as a function of the stripe width while a marked instability versus width is observed in the region less than $100\mu\text{m}$ (closer to the reservoir), because $k_2 = 0.037 (\pm 0.0143) \mu\text{m}^{-1}$. Assuming that the fluorescence intensity depends on the local density of laminin deposited on the surface, we can explain this result by a simple model where the laminin solution infills the capillaries upon the action of Laplace pressure, then the solute diffuses to the substrate. The density of deposited laminin reflects the concentration profile of the solution in the capillary.

Finite-element method (FEM) was carried out on the section of the microchannel involved in the MIMICs process. The model domain has been simplified into a two-dimensional section of single PDMS microchannel, including the elastomeric wall and the TC dish for the cell culture as lower boundary. The velocity field was calculated by the Navier–Stokes equation, adapted to take into account the effect of surface tension acting along the channel boundaries. The transport of protein is governed predominantly by convection during the infilling (Figure 3.3) and by diffusion at later stages when the microchannel is filled up, and there is no replenishment by fresh protein solution. The density ρ of laminin adsorbed onto the TC dish surface (continuous thin lines in figure 3.3 at different times) was determined assuming surface diffusivity and kinetic equilibrium at the solid–liquid interface. The diffusion coefficient for laminin in cell culture medium was calculated using the Einstein–Stokes equation and equals $1.14 \times 10^{-7} \text{ cm}^2 \text{ s}^{-1}$ in the FEM model. This value is in the same range of that reported in the literature¹². The velocity profile induced by surface tension differs from the standard Poiseuille parabolic distribution: it is not constant in time, and is locally modified by the change of the wetting properties upon adsorption. FEM analysis yields an amount of adsorbed laminin that increases with time. Concentration is always higher at the entrance of the microchannels and decreases along the longitudinal axis of the channel. A comparison between the local density estimated from the simulation (Figure 3.3, continuous thin lines) and the fluorescence intensity of laminin revealed by immunofluorescence staining (Figure 3.3, black marker) supports the evidence that MIMICs generates a gradient of laminin along the main axis of the microfluidics channels. Capillary flow is responsible for the formation of the initial gradient of concentration inside the microchannel. After this, adsorption is mainly ruled by diffusion from the solution to the surface.

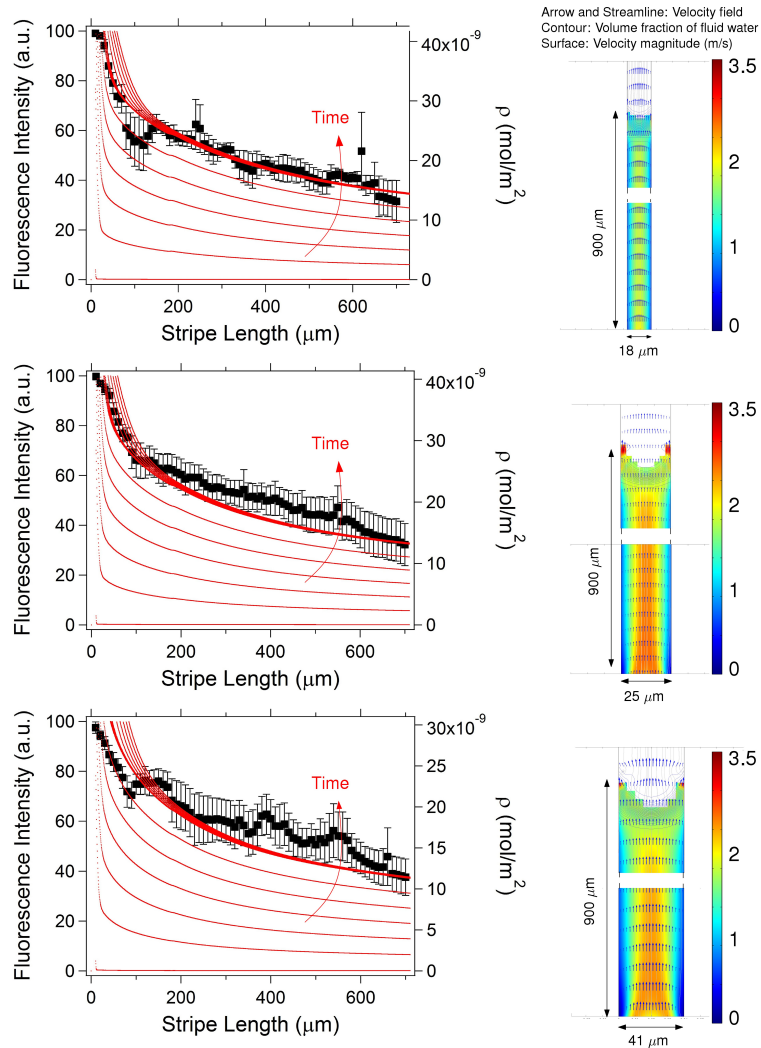


Figure 3.3: Laminin gradient analysis of immunofluorescence data by FEM. (left panel) representative data of laminin fluorescence intensities (y-axis, left) versus stripe length are shown for the same stripes. The black dots outline the decrease in fluorescence intensity. Concentration of adsorbed laminin (y-axis, right), obtained from finite-element calculation, is plotted versus stripe length (continuous lines). The concentration gradient is increasing with time during MIMICs deposition; (right panel) Velocity fields calculated on the horizontal plane of microchannels whose width equals to 18, 25 and 41 μm .

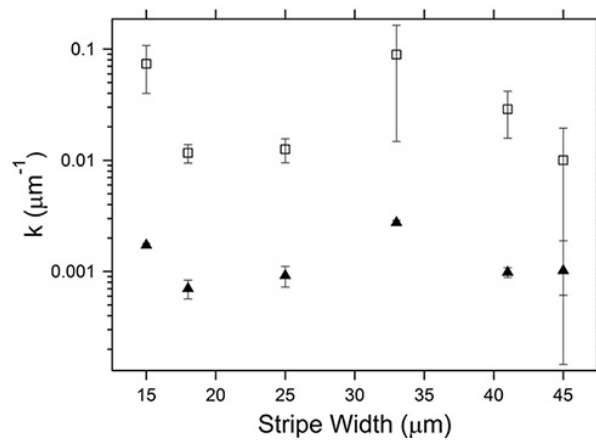


Figure 3.4: Inverse decay lengths of the double exponential fit extracted from the analysis of laminin fluorescence intensity. k_1 describes the slope of gradient at large distances from the reservoir (solid symbol), whereas k_2 regulates the second slope close to the reservoir (empty symbol). Values are expressed as mean \pm s.e.m.

In figure 3.4, we report the two parameters k_1 and k_2 describing the double exponential decay of the gradient as a function of the channel width. These data show the behaviour of the two constants does not depend on the channel width.

3.4 Analysis of cell nuclei orientation

The ability of the laminin pattern to guide neural cell adhesion and proliferation was investigated through the analysis of nuclei orientation and cellular density. The 1321N1 astrocytoma cells were randomly seeded onto laminin-patterned substrates and they were let to proliferate under standard cell culture conditions in the presence of serum-containing medium. To visualize the nuclei, the cells were fixed and subsequently stained with the specific nuclei dye DAPI (see Chapter 2 for protocol). Representative results after 6 days of incubation are reported in figure 3.5. To visualize cell shape, optical micrographs were collected, and sample images are reported in figure 3.4 c,e.

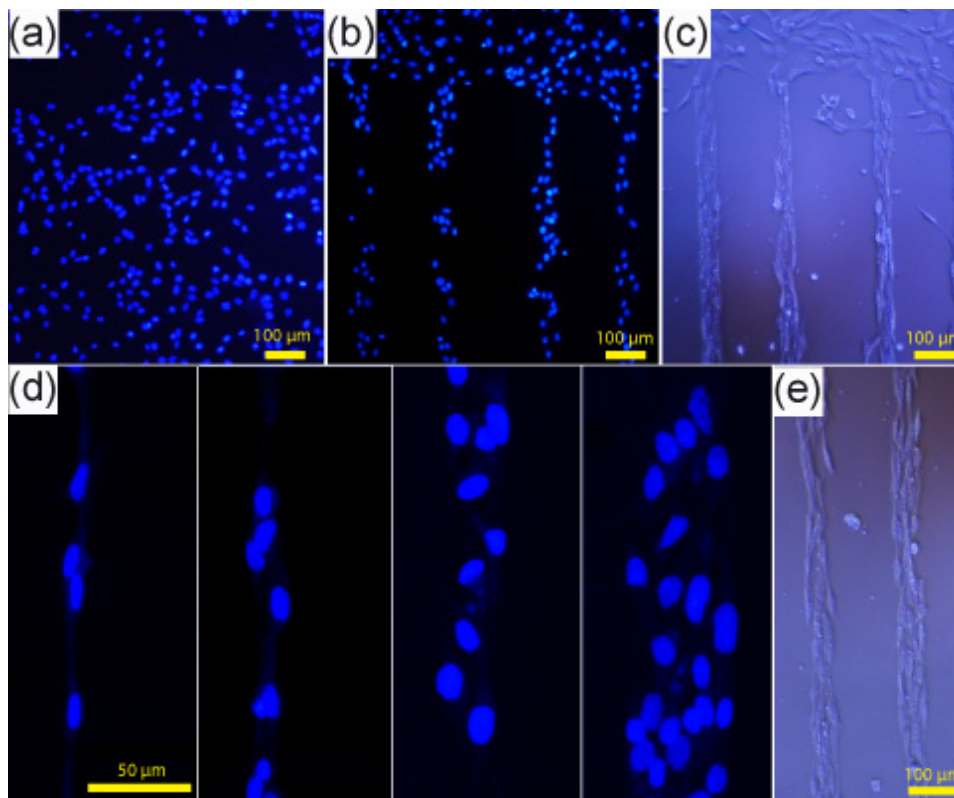


Figure 3.5: Optical and fluorescence micrographs of 1321N1 astrocytoma cells after 6 days of incubation under standard cell culture conditions. Nuclei of 1321N1 astrocytoma cells stained with DAPI on laminin unpatterned (a) and patterned (b) regions of polystyrene TC dishes; (d) higher magnification images showing details of nuclei organization in parallel lanes onto laminin stripes with increasing widths. In (c,e), optical micrographs of the patterned culture where the whole cell shape can be appreciated.

On laminin-patterned TC dishes, selective adhesion of the neural cells along patterned stripes was observed (figure 3.5b), whereas on unpatterned regions, cells proliferated without any preferential orientation and position on the surface (Figure 3.5a). The latter cell behaviour, that is the control experiment, was observed on bare TC in the presence of serum in the culture medium even at prolonged cell incubation times. The comparison of figure 3.5a with

figure 3.5b clearly shows that the proliferation of cells in figure 3.5b follows the geometrical distribution of the laminin pattern onto the surface. Cell nuclei are visible over the laminin-patterned areas. They are accommodated in almost parallel lanes within a stripe (Figure 3.5d). The number of cells across the stripe scales proportionally to the stripe width, ranging from a single cell lane in the case of the smaller stripes (15 μ m; figure 3.5d, left panel) up to four parallel lanes for the larger ones (45 μ m; figure 3.5d, right panel). Interestingly, no cells are found between the laminin stripes, independently of the spacing between the stripes. This indicates that during the culture, all adhered cells migrate preferentially towards the protein stripes and proliferate onto them¹⁸. This happens without any previous anti-fouling passivation processes of the surface between the stripes. We infer that the adhesion propensity contrast between polystyrene surface and laminin pattern creates adjacent cell-adhesive/cell-repulsive regions on the substrate. As the cells are seeded homogeneously on the surface, they are driven towards the laminin lines by a lateral gradient that is possibly generated by a slow dissolution/partition of laminin from the patterned lines with subsequent lateral diffusion.

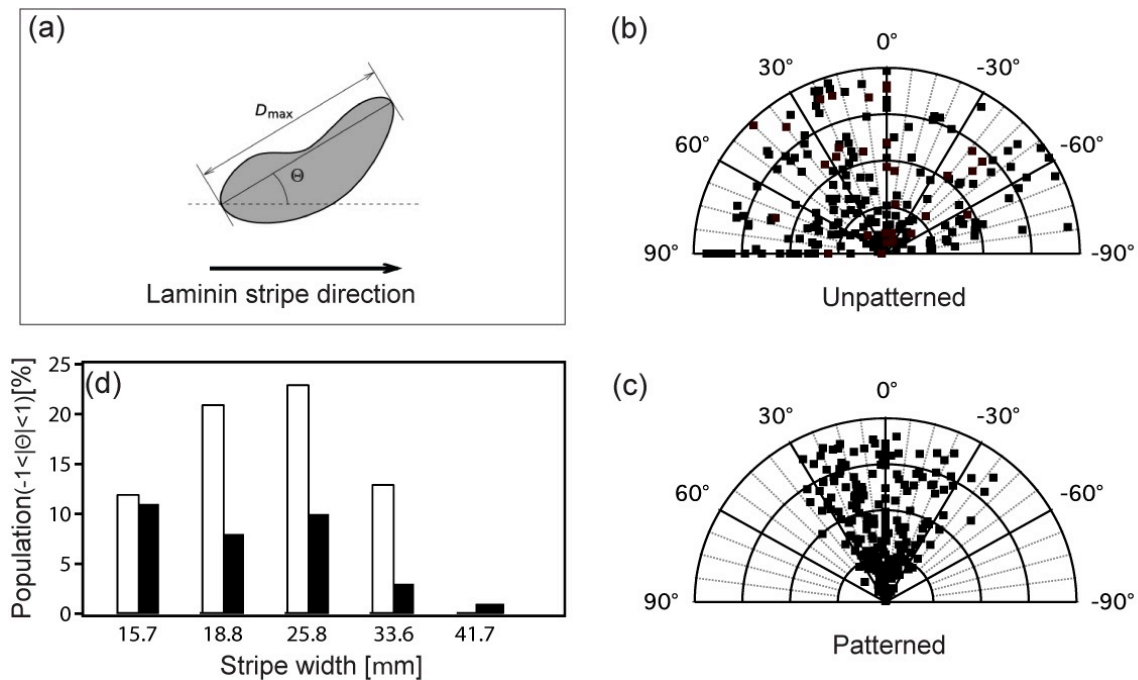


Figure 3.6: Analysis of the orientation of 1321N1 cell nuclei: (a) Definition of the orientation angle θ of nucleus along the laminin stripe direction. Polar plots of angle θ values for cells on laminin unpatterned (b) and patterned (c) regions of TC dishes (representative example for stripe with 25.8 μ m nominal width is shown). (d) Percentage population of nuclei with angle values $-1^\circ < \theta < 1^\circ$ (indicating high grade of alignment) versus stripe width, estimated in region closer (white bars) and further from the reservoir (black bars).

After incubation, the alignment of the cells was statistically analysed from fluorescence images by measuring the orientation angle of DAPI-stained nuclei using GWYDDION image software. The analysis was performed both on laminin-patterned and unpatterned regions on the surface. Each analysis was performed on fluorescence images at the same magnification, with the grain analysis function used to identify the stained nuclei. The contour of each cell nucleus is fitted with an ellipse whose major and minor axes are identified. For the k th cell, $\theta_{k,x}$ is the angle measured between the major axis and an arbitrary direction of the image, which we chose as the horizontal (x -axis; figure 3.6a). The θ_x values in degrees were reported in polar plots whose azimuth ranges from -90° to 90° , and the 0° corresponds to the direction

of the patterned stripes. The distribution of θ_x values was analysed along the stripes up to a distance of 700 μm from the channel entrance (taken as $L=0$), and up to 200 μm for the unpatterned region. Both distances were extracted from the fluorescence micrographs.

The influence of laminin gradient on neural cell alignment was thus assessed. The orientation of the neural cell nuclei was quantitatively analysed in both laminin unpatterned and patterned areas by measuring the orientation of the nucleus. For the laminin patterned surface, the angle θ is defined as the angle between the direction of the laminin stripe and the major axis of the cell nucleus, as shown in figure 3.6a. The distribution of θ angles was analysed along the stripes for each width. Representative polar plots for laminin unpatterned and patterned regions are shown in figure 3.6b and c, respectively. The data revealed a random distribution for cells grown on unpatterned areas with an angle mean value = $44^\circ \pm 2^\circ$. On laminin-patterned surfaces, the values of θ angles were mainly distributed in the $-20^\circ / +20^\circ$ range. More specifically, in figure 3.6d, we plot the percentile population of cell nuclei aligned within $-1^\circ < \theta < 1^\circ$ versus stripe width for various distances from the reservoir. The population showing θ angles in this range was always higher in the region closer to the reservoir (white column), which is characterized by the higher laminin immunofluorescence intensity and a steeper gradient slope. This trend was observed for each stripe width. The narrower channels yield a higher percentage of aligned cells with a maximum of 25% corresponding to the stripe with 25.8 μm nominal width. The population of aligned cells tends to decrease with increasing stripe width down to only 2% for 41.5 μm nominal width. This indicates that the aligning effect of the gradient is more relevant when the stripe can host only one cell inducing also a lateral confinement.

3.5 Correlation between laminin gradient and orientation order parameter

Analysis of the alignment of cell nuclei was then performed by estimating the order parameter that quantifies the average orientation of the nuclei²⁶. In the azimuthal plane (two-dimensional), the order parameter is estimated using the procedure described in Biscarini et al²⁷. First, we construct the 2 x 2 order matrix \mathcal{S} whose entry $S_{xy} = [2\langle \cos \theta_x \cos \theta_y \rangle - \delta_{xy}]$ where δ_{xy} is Kronecker's delta, brackets indicate the arithmetic mean of the product of direction cosines, and $\theta_y = 90^\circ - \theta_x$. Then we diagonalize the \mathcal{S} matrix to yield the main alignment axis (director) as the one corresponding to the largest eigenvalue $S_{xx} = \langle \cos 2\theta \rangle$. The order parameter S_{xx} is equal to 1 when the nuclei are perfectly aligned along the director, whereas S is 0 when the orientation of the cell nuclei is random or the nucleus has an isotropic contour.

In Figure 3.7 we plot the order parameter $S = \langle \cos 2\theta \rangle$ vs gradient slope, for short (k_2 , squares) and long (k_1 , triangles) distances from the reservoir. First of all, it is crucial that the S -values on patterned stripes are much higher than the ones on the laminin-unpatterned regions ($S=0.128 \pm 0.057$). The order parameter tends to decrease from 0.8 to 0.65 as the stripe width increases close to the reservoir (identified by the inverse characteristic length scale k_2), whereas it is almost constant in the region far from the reservoir (identified by the inverse

characteristic length scale k_l) with values ranging from 0.65 to 0.7. Owing to the weak correlation found between the mean gradient at both length scales and the stripe width in the range explored (Figure 3.4), we cannot establish without uncertainty a correlation between the orientational order parameter and the laminin gradient. We notice that the order parameter values in the region closer to the reservoir are more spread out than their counter parts in the region far from the reservoir. The existence of such a correlation is suggested by the data in figure 3.7, at least for the steeper regions of the gradient where the local laminin concentration varies over distances comparable with the cell size ($\approx 15\mu\text{m}$).

These results support the hypothesis that the laminin concentration gradient along the stripe promotes cellular recruitment and adhesion at the patterned regions, as well as their anisotropic alignment along the patterned stripes. The steeper laminin gradient observed in the initial $100\mu\text{m}$ might enhance the alignment.

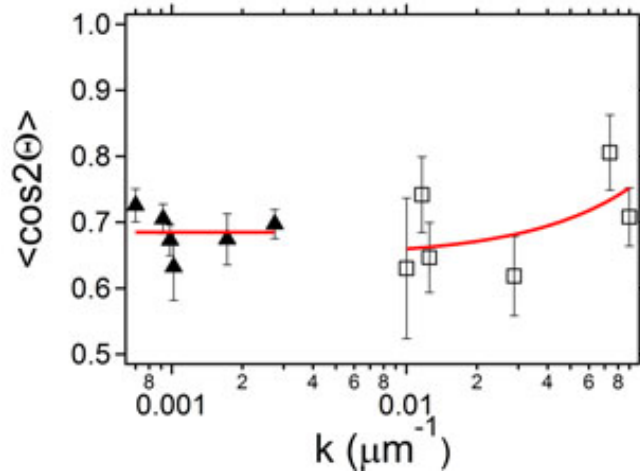


Figure 3.7: Correlation between order parameter $S = \langle \cos 2\Theta \rangle$ versus exponential decay length (k_1 and k_2) of the gradients. Values corresponding to the region close to (squares) and far from (triangles) the reservoir.

3.6 Conclusions

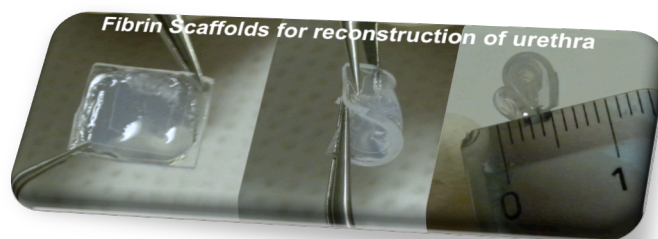
We have demonstrated an easy method for fabricating gradients of an ECM protein, laminin, with a controlled and reproducible geometry. The resulting patterns guide neural cell growth and orient cells along the pattern direction. We have shown that stringent control can be achieved even on a plastic, non-anti-fouling surface through a simple technological method to pattern laterally confined laminin gradients as the chemical cell guidance cue. Our approach does not require any background passivation step, whereas many other methods use surface pre-treatment with an anti-cell-adhesion layer such as poly(-ethylene glycol) (PEG) to enhance compositional contrast^{28,29} or by creating double-cue opposing gradients³⁰. Here, we have exploited the surface tension feature of the polystyrene substrate (contact angle = $67.3^\circ \pm 1.5^\circ$) to maintain the cell culture confinement for a prolonged time in the presence of serum-containing medium. In fact, the uncharged and mildly hydrophobic surface of untreated polystyrene TC dishes used in this work is reported to partially prevent the adsorption of proteins and other biomolecules contained in the cell culture medium; cells and biomolecules bind this surface only through passive hydrophobic interactions²². Hydrophilic (wettable) surfaces such as those of polylysine-coated glass slides³¹ as well as positive surface

charges have a beneficial effect on cell adhesion^{32,33}. This study shows that is possible to achieve directional and spatial control of neural cell growth over long periods of time by means of patterned protein gradients. Patterning is an effective tool to govern the chemical stimuli-induced organization of different cell phenotypes, also in co-culture studies. It could open up a way for fabricating arrays or multi-layer architectures of multiple cell types to investigate cell–cell interactions, signalling cross-talk and cell response to toxic and/or pharmacological agents with potential applications in pharmaceuticals, diagnostics and toxicology as well as in implant technology, including tissue engineering.

Bibliography

- 1 B Chelli, M. B., F Valle, P Greco, E Bystrenova, M Bianchi and F Biscarini. Neural cell alignment by patterning gradients of the extracellular matrix protein laminin. *Interface Focus* **4**, 20130041, (2013).
- 2 Dado, D. & Levenberg, S. Cell-scaffold mechanical interplay within engineered tissue. *Semin Cell Dev Biol* **20**, 656-664, (2009).
- 3 Lee, M. R. *et al.* Direct differentiation of human embryonic stem cells into selective neurons on nanoscale ridge/groove pattern arrays. *Biomaterials* **31**, 4360-4366, (2010).
- 4 Omstead, D. R. *et al.* Voluntary guidance for the development of tissue-engineered products. *Tissue Eng* **4**, 239-266, (1998).
- 5 Timko, B. P., Cohen-Karni, T., Qing, Q., Tian, B. Z. & Lieber, C. M. Design and Implementation of Functional Nanoelectronic Interfaces With Biomolecules, Cells, and Tissue Using Nanowire Device Arrays. *Ieee T Nanotechnol* **9**, 269-280, (2010).
- 6 Bettinger, C. J., Langer, R. & Borenstein, J. T. Engineering Substrate Topography at the Micro- and Nanoscale to Control Cell Function. *Angew Chem Int Edit* **48**, 5406-5415, (2009).
- 7 Discher, D. E., Mooney, D. J. & Zandstra, P. W. Growth Factors, Matrices, and Forces Combine and Control Stem Cells. *Science* **324**, 1673-1677, (2009).
- 8 Gauvin, R. & Khademhosseini, A. Microscale Technologies and Modular Approaches for Tissue Engineering: Moving toward the Fabrication of Complex Functional Structures. *Acs Nano* **5**, 4258-4264, (2011).
- 9 Geiger, B., Spatz, J. P. & Bershadsky, A. D. Environmental sensing through focal adhesions. *Nat Rev Mol Cell Bio* **10**, 21-33, (2009).
- 10 Ochsner, M., Textor, M., Vogel, V. & Smith, M. L. Dimensionality Controls Cytoskeleton Assembly and Metabolism of Fibroblast Cells in Response to Rigidity and Shape. *Plos One* **5**, (2010).
- 11 Roeder, I., Loeffler, M., Glauche, I. & Participants, O. Towards a quantitative understanding of stem cell-niche interaction: Experiments, models, and technologies. *Blood Cell Mol Dis* **46**, 308-317, (2011).
- 12 Cai, K. Y. *et al.* Inkjet printing of laminin gradient to investigate endothelial cellular alignment. *Colloid Surface B* **72**, 230-235, (2009).
- 13 DeLong, S. A., Moon, J. J. & West, J. L. Covalently immobilized gradients of bFGF on hydrogel scaffolds for directed cell migration. *Biomaterials* **26**, 3227-3234, (2005).

- 14 Dertinger, S. K. W., Jiang, X. Y., Li, Z. Y., Murthy, V. N. & Whitesides, G. M. Gradients of substrate-bound laminin orient axonal specification of neurons. *P Natl Acad Sci USA* **99**, 12542-12547, (2002).
- 15 Liu, L. Y., Ratner, B. D., Sage, E. H. & Jiang, S. Y. Endothelial cell migration on surface-density gradients of fibronectin, VEGF, or both proteins. *Langmuir* **23**, 11168-11173, (2007).
- 16 Sant, S., Hancock, M. J., Donnelly, J. P., Iyer, D. & Khademhosseini, A. Biomimetic Gradient Hydrogels for Tissue Engineering. *Can J Chem Eng* **88**, 899-911, (2010).
- 17 Smith, J. T., Elkin, J. T. & Reichert, W. M. Directed cell migration on fibronectin gradients: Effect of gradient slope. *Exp Cell Res* **312**, 2424-2432, (2006).
- 18 Ventre, M., Valle, F., Bianchi, M., Biscarini, F. & Netti, P. A. Cell Fluidics: Producing Cellular Streams on Micropatterned Synthetic Surfaces. *Langmuir* **28**, 714-721, (2012).
- 19 Hassell, M. A. H. a. J. R. *Extracellular matrix: a practical approach*. Ithaca, N.Y: IRL Press. (Ithaca, 1995).
- 20 Timpl, R. *et al.* Laminin-a glycoprotein from basement membranes. *The Journal of biological chemistry* **254**, 9933-9937, (1979).
- 21 Wunsch, J. R. *Polystyrene : synthesis, production and applications* (iSmithers Rapra Publishing, 2000).
- 22 Curtis, A. S. G., Forrester, J. V., Mcinnes, C. & Lawrie, F. Adhesion of Cells to Polystyrene Surfaces. *J Cell Biol* **97**, 1500-1506, (1983).
- 23 Grinnell, F. Cellular adhesiveness and extracellular substrata. *International review of cytology* **53**, 65-144, (1978).
- 24 Amstein, C. F. & Hartman, P. A. Adaptation of Plastic Surfaces for Tissue-Culture by Glow-Discharge. *J Clin Microbiol* **2**, 46-54, (1975).
- 25 Loschinger, J., Weth, F. & Bonhoeffer, F. Reading of concentration gradients by axonal growth cones. *Philos T Roy Soc B* **355**, 971-982, (2000).
- 26 JP., S. Ordered phases of a liquid of biaxial particles. . *Phys. Rev. A* **10** , 1881 – 1887., (1974).
- 27 Biscarini, F., Greco, O., Lauria, A., Zamboni, R. & Taliani, C. Orientational ordering of domains in vacuum-grown oligomer thin films: A Scanning Force Microscopy study. *Mol Cryst Liq Cryst A* **290**, 203-212, (1996).
- 28 Krsko, P. *et al.* Length-scale mediated adhesion and directed growth of neural cells by surface-patterned poly(ethylene glycol) hydrogels. *Biomaterials* **30**, 721-729, (2009).
- 29 Rolli, C. G. *et al.* Switchable adhesive substrates: Revealing geometry dependence in collective cell behavior. *Biomaterials* **33**, 2409-2418, (2012).
- 30 Li, G. N., Liu, J. & Hoffman-Kim, D. Multi-molecular gradients of permissive and inhibitory cues direct neurite outgrowth. *Ann Biomed Eng* **36**, 889-904, (2008).
- 31 Lakard, S. *et al.* Adhesion and proliferation of cells on new polymers modified biomaterials. *Bioelectrochemistry* **62**, 19-27, (2004).
- 32 Hallab, N. J., Bundy, K. J., OConnor, K., Clark, R. & Moses, R. L. Cell adhesion to biomaterials: Correlations between surface charge, surface roughness, adsorbed protein, and cell morphology. *J Long-Term Eff Med* **5**, 209-231, (1995).
- 33 Liu, B. F., Ma, J., Xu, Q. Y. & Cui, F. Z. Regulation of charged groups and laminin patterns for selective neuronal adhesion. *Colloid Surface B* **53**, 175-178, (2006).



Chapter 4

Fibrin 3D-scaffolds for reconstruction of urethra

This chapter describes the fabrication, characterization and analysis of scaffolds to be used as supports for the reconstruction of the whole or portions of human urethra in the perspective of a novel treatment of urethral strictures. The supports have been made of fibrin gel, which is a biocompatible and biodegradable material already widely used in clinical stage that is suitable for achieving a tubular geometry. We observed cell growth on both scaffold with random orientation on both substrates manufactured with a preferred orientation. We have paid particular attention to the implementation of a micro-frame acting as a handling tool to allow in the future an easy manipulation by the surgeon. An important goal was to fabricate 3D scaffolds with a well-defined morphology being the topographic signal an important toolbox for guiding the cell behaviour. We have characterized the material using the scanning electron microscope (SEM) to assess qualitatively and quantitatively the physical architecture of the samples. To understand the morphology of the fibrin network, the power spectrum density of the images has been computed and then analysed to identify the presence of correlation lengths that represent the characteristic lengths of the network. The characterization of the fibrin network by SEM has helped us to understand how the morphology of the fibrin network could affect cell growth. Indeed, the different correlation lengths are important because they influence different requirements of cell proliferation.

4.1 Introduction

The male urethra extends from the internal urethral orifice in the urinary bladder to the external urethral orifice at the end of the penis. Its length varies from 17.5 to 20 cm; and it is divided into three portions, the prostatic, membranous, and cavernous, the structure and relations of which are essentially different. Except during the passage of the urine or semen, the greater part of the urethral canal is a mere transverse cleft or slit, with its upper and lower surfaces in contact; at the external orifice the slit is vertical, in the membranous portion irregular or stellate, and in the prostatic portion somewhat arched (Figure 4.1)¹.

The prostatic portion (*pars prostatica*), the widest and most dilatable part of the canal, is about 3 cm. long. It runs almost vertically through the prostate from its base to its apex, lying nearer its anterior than its posterior surface; the form of the canal is spindle-shaped, being wider in the middle than at either extremity, and narrower below, where it joins the membranous portion. Upon the posterior wall or floor there is a narrow longitudinal ridge, the urethral crest (*verumontanum*), formed by an elevation of the mucous membrane and its

subjacent tissue. On either side of the crest a slightly depressed fossa is present, the prostatic sinus, the floor of which is perforated by numerous apertures, the orifices of the prostatic ducts from the lateral lobes of the prostate; the ducts of the middle lobe open behind the crest. At the forepart of the urethral crest, below its summit, there is a median elevation, the colliculus seminalis, upon or within the margins of which are the orifices of the prostatic utricle and the slit-like openings of the ejaculatory ducts¹. The prostatic utricle (*sinus pocularis*) forms a cul-de-sac about 6 mm long, which runs upward and backward in the prostate behind the middle lobe. Its walls are composed of fibrous tissue, muscular fibers, and mucous membrane; a number of small glands open on its inner surface.

The membranous portion (*pars membranacea*) is the shortest, least dilatable and, with the exception of the external orifice, the narrowest part of the canal. It extends downward and forward, with a slight anterior concavity, between the apex of the prostate and the bulb of the urethra, perforating the urogenital diaphragm about 2.5cm below and behind the pubic symphysis. The membranous portion of the urethra is completely surrounded by the fibers of the Sphincter urethra membranacea. The cavernous portion (*pars cavernosa*; penile or spongy portion) is the longest part of the urethra, and is contained in the corpus *cavernosum* urethra. It is about 15cm. long, and extends from the termination of the membranous portion to the external urethral orifice. The external urethral orifice (*orificium urethra externum*; *meatus urinarius*) is the most contracted part of the urethra; it is a vertical slit, about 6 mm. long, bounded on either side by two small labia.

The urethra is composed of mucous membrane, supported by a submucous tissue which connects it with the various structures through which it passes (Figure 4.1). The mucous coat forms part of the genito-urinary mucous membrane. It is continuous with the mucous membrane of the bladder, ureters, and kidneys; externally, with the integument covering the glans penis; and is prolonged into the ducts of the glands which open into the urethra, viz., the bulbo-urethral glands and the prostate; and into the ductus deferentes and vesicula seminales, through the ejaculatory ducts. In the cavernous and membranous portions the mucous membrane is arranged in longitudinal folds when the tube is empty. Small papilla are found upon it, near the external urethral orifice; its epithelial lining is of the columnar variety except near the external orifice, where it is squamous and stratified¹.

The submucous tissue consists of a vascular erectile layer; outside this is a layer of unstripped muscular fibers, arranged, in a circular direction, which separates the mucous membrane and submucous tissue from the tissue of the corpus cavernosum urethra.

In medicine, there are many non-lethal diseases having a highly negative impact on the quality of life. Many of these diseases have no realistic alternative treatments because the results produced by the interventions of traditional medicine are not sufficient as they are likely to produce more severe worsening or recurrence of the original disease. Some pathologies of the mucosal epithelia or internal belong to this category, such as certain aberrations such as hypospadias and strictures^{2,3}. Hypospadias is a malformation of the external urethral meatus that instead of being located at the apex of the glans of the penis is located at different positions. Hypospadias may be associated with a malformation of the corpora cavernosa, with the presence of curvature of the penis in erection or to a anomalous arrangement of the skin of the penis and prepuce.

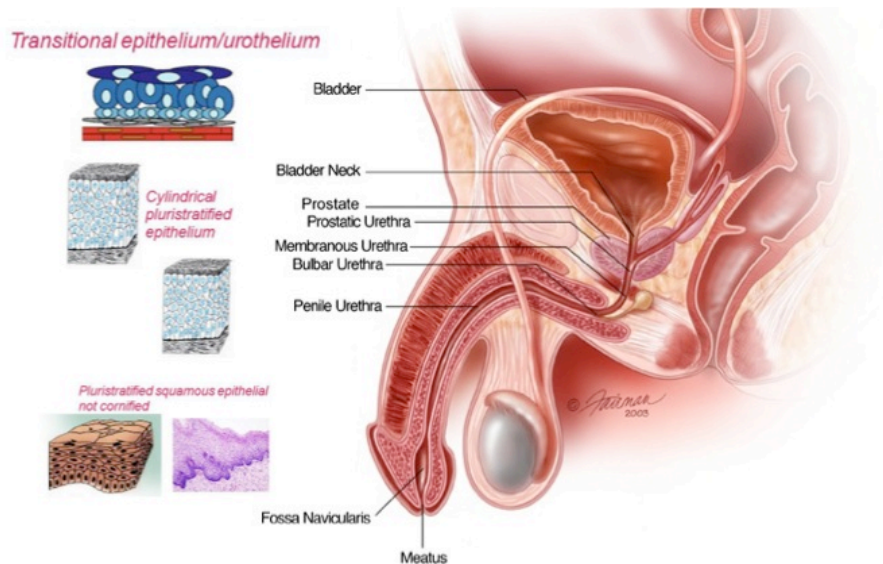


Figure 4.1: Urethra male structure. Scheme summarizing the different types of epithelium.

In some patients, the hypospadias may be associated with a stenosis of the urethral meatus or a penile or bulbar urethral strictures^{4,5}. The urethral canal may present a reduction or a complete obstruction of his caliber called urethral stricture. The male urethral stricture may be due to congenital malformations such as hypospadias described above, or to acquired diseases, which have arisen, at various ages. The development of this disease leads to serious consequences for the patient, in the first instance due to the inability to properly eject semen and urine. The treatment is essentially surgical urethral stenosis^{6,7}: in the first instance one proceed to a progressive dilatation of the urethral caliber, periodically performed as an outpatient procedure using disposable catheters. At relapse of the problem an urethrotomy is carried out, which consists of endoscopic incision of the stenotic tract. Frequently, however, the disease recurs, then the last option is a urethroplasty. The urethra is completely sectioned at the level of the stenotic tract. The scar tissue that created the stenosis is removed and the two dies are brought together and sutured. If it is not possible to proceed in this way a two-stage urethroplasty with buccal mucosa graft is performed: the urethra is opened longitudinally at the level of the stenotic tract and the canal is enlarged with a strip of buccal mucosa, taken from inside the cheek or tongue. It is a real auto-transplantation, as the strip of mucosa is completely detached from the inside of the mouth or the tongue and sutured on the urethra⁸⁻¹⁰. In bulbar urethral strictures, during the first surgery, the urethra is opened below the scrotum and urine escapes from this new ostomy, forcing the patient to urinate in a sitting position. When possible, this perineal stoma may be closed, allowing the patient to urinate again through the penis. In other cases, the perineostomy is final, not being possible to regain the patient urination through the penis. The exact incidence of male urethral strictures is unknown, although they have significant negative effects on the quality of life of those who are affected. From the above description it is clear how the interventions to solve this problem are associated to a number of complications, in addition to being extremely invasive and frequently incurring in recurrences. The endoscopic urethrotomie may be associated with complications such as bleeding in the 4% -6% of cases, infection in 8% -9%, incontinence and impotence in 1% of cases, with a recurrence rate of stenosis that can reach 100% cases. Following endoscopic urethrotomie or dilatation, stenosis tend to recur until it is used in

therapy with urethroplasty definitive, which implies the impotence of the patient. Even after the urethroplasty potential complications for the patient are present. Surgical complications affects up to 7% of the end-to-end urethroplasty and up to 33% of the fasciocutaneous graft urethroplasty. In addition, it has been shown that the rate of erectile dysfunction after an end-to-end urethroplasty can be up to 27%. The use of autologous urethral tissue then is not often associated with complications, prolonged hospitalization and morbidity in the area. Regenerative medicine uses innovative therapies aimed at restoring permanent tissues or organs damaged by the growth of the patient's own stem cells^{11,12} on a biocompatible scaffold. In this framework we decided to use the fibrin gel to fabricate the biocompatible scaffold to be used for the reconstruction of portions of the human urethra.

Fibrin

Fibrin is an important element in tissue engineering because of its use as a scaffold material. Compared to synthetic polymers and collagen gels it is better in terms of cost, inflammation, immune response, toxicity and cell adhesion¹³. When there is a trauma in body, cells at the site start the cascade process of blood clotting and fibrin is the first scaffold formed¹⁴. To achieve its clinical use as a scaffold, the fast and entire incorporation into host tissue is essential¹⁵. Regeneration of the tissue and the degradation of the scaffold should be tuned in terms of rate, surface area and interaction to achieve an ideal templating¹⁶. Fibrin satisfies many requirements of scaffold functions. Biomaterials made up of fibrin can attach many biological surfaces with high adhesion. Its biocompatibility comes from being not toxic, allergenic or inflammatory^{16,17}. Fibrinogen and fibrin play important, overlapping roles in blood clotting, fibrinolysis, cellular and matrix interactions, inflammation, wound healing, and neoplasia. These events are regulated to a large extent by the fibrin formation process and by interactions between specific sites on fibrinogen or fibrin and extrinsic molecules such as proenzymes, clotting factors, growth factors, enzymes inhibitors, and cell receptors. Fibrinogen molecules are elongated 45-nm structures consisting of two outer D domains, each connected by a coiled-coil segment to a central E domain. Fibrinogen circulates at ~3mg/mL in the blood as a 340kDa glycoprotein comprising a symmetrical pair of three protein chains - α , β and γ (Figure 4.2). Fibrinogen features numerous binding sites for pro-coagulant proteins (thrombin, factor XIII), pro-fibrinolytic proteins (plasminogen, tissue plasminogen activator), anti-fibrinolytic proteins (plasminogen activator inhibitor), growth factors (fibroblast growth factor-2, vascular endothelial growth factor, platelet derived growth factor), extra-cellular matrix components (fibronectin, heparin), and cell receptors (integrins, cadherins)^{18,19}. Fibrin has therefore many favorable biological properties as a scaffold material to be used in tissue engineering and surgical applications^{13,20}. Fibrin network formation, or fibrin polymerization, from its precursor fibrinogen is initiated upon activation of the clotting enzymes, pro-thrombin and FXIII. *In vivo*, pro-thrombin is proteolytically cleaved and activated by activated clotting factor X in the first common step of the intrinsic (or contact factor) and extrinsic (or tissue factor) activation pathways of the coagulation cascade. The activated serine protease, thrombin, catalyzes the removal of fibrinopeptides (FpA, FpB) from the N-terminal regions of the α and β chains of fibrinogen, exposing short peptide sequences known as knob 'A' and knob 'B' that bind to hole 'a' and hole 'b' in the C-termini of neighboring fibrinogen molecules (Figure 4.2).

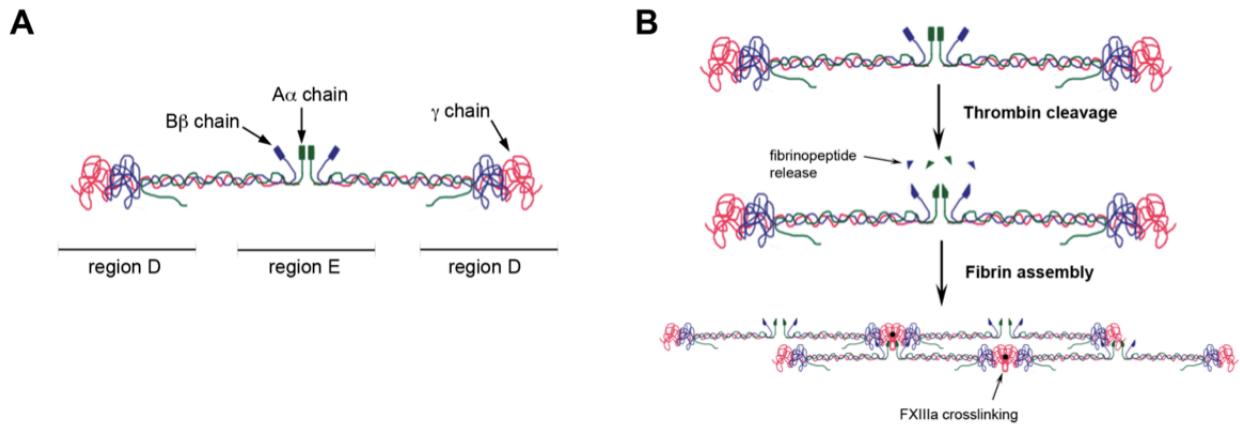


Figure 4.2: Fibrinogen and fibrin polymerization schematic. (A) Illustration of the basic fibrinogen structure depicting the α chain in green, β chain in blue, γ chain in red. (B) Steps involved in fibrin polymerization.

The central location of the knobs in region E, contrasting with the distal location of the holes in region D, results in the formation of half-staggered two-stranded protofibrils that associate to form the fibrin network. Thrombin also activates the clotting factor XIII (FXIII). FXIII, also known as the fibrin stabilizing factor, crosslinks the α and γ chains of fibrinogen, producing a mechanically stronger, more rigid and more elastic clot with increased resistance to fibrinolysis^{21,22}. FXIII circulates in the plasma at a concentration of 14-28 $\mu\text{g/ml}$.

The timescale for the chemical crosslinking of fibrin is typically orders of magnitude (minutes to hours) larger than the assembly of monomers initiated by the release of fibrinopeptides (seconds to minutes). Fibrin network structure is therefore largely dictated by the release kinetics of the fibrinopeptides and concomitant exposure of knobs, whose knob: hole binding kinetics is in turn dependent on factors such as enzyme, substrate and ion concentration.

Differences in clot stiffness can have significant physiological implications, in that highly rigid clots may be prone to thrombosis, while fragile clots may lead to premature lysis and re-opening of the wound²³. Fibrin network structure is typically modified by varying clotting conditions such as fibrinogen and thrombin concentration, buffer ionic strength (typically sodium chloride, NaCl), calcium ion concentration (typically calcium chloride, CaCl_2), pH, and the use of alternative thrombin-like clotting enzymes (e.g. ancrod, batroxobin)^{24,25}. Translucent clots formed at high thrombin or high NaCl concentration are commonly interpreted to be thin, highly-branched networks. Opaque clots are formed at low NaCl or high calcium concentration, conditions that apparently favor lateral aggregation of the fibrin protofibrils, giving rise to thicker bundles that scatter more light. In general, large fiber diameters and lengths were associated with minimal branching and the converse is also true²⁵.

Fibrin glue

Several reviews published in recent years have focused on uses of fibrin glue, also referred to as fibrin tissue adhesive or fibrin sealant, in clinical and surgical practice²⁶⁻²⁹. In the literature, fibrin was first mentioned more than 90 years ago. It has been documented that fibrinogen combined with thrombin was used to improve the adhesion of skin grafts of soldiers with burn injuries during the Second World War²⁸. A commercial product has been available in Europe

and Japan since the 80s, whereas fibrin glue was not FDA approved until 1998 because of possible viral contamination. At the moment, fibrin sealant is considered the most effective physiological tissue adhesive available. There are a number of commercially available fibrin products with different amounts and origins of the components^{26,28,30}. The concentration of fibrinogen, varying between 40 and 125 mg/ml, is directly correlated to the tensile strength of the fibrin clot, whereas the concentration of thrombin influences the degree and speed of clotting. The latter proves useful for quick haemostasis to prevent blood loss (e.g., in suturing of vessels) or in surgical procedures involving careful glue adjustment to fit a tissue or organ²⁶. Within 3 days of application, a preliminary granulation tissue with a large number of wound healing cells is present and is subsequently replaced with collagen fibers one to two weeks later. During normal wound healing the fibrin glue is absorbed within days to weeks depending on the type of sealant and location of application³¹. The majority of glues contain an anti-fibrinolytic component to reduce the degradation rate. A common agent is the protease inhibitor aprotinin, which inhibits human trypsin and plasmin by blocking the active sites of the enzymes.

The most prevalent application of fibrin in clinical practice is its use as a haemostatic agent, especially in heparinized or coagulopathic patients, to reduce operative bleeding, e.g., in cardiovascular surgery. The application is most effective when polymerized prior to the onset of bleeding, for example in surgery of a vascular anastomosis³⁰. When using fibrin sealants or sprays as adjunct to sutures, a better wound healing and optimal wound integrity results in operative locations where the use of conventional sutures is not feasible or would result in intense bleedings^{29,30}. Fibrin polymers play a key role in tissue and organ sealing, particularly in plastic and reconstructive surgery, including skin grafting³⁰. Exact adjustment is possible, bleeding is reduced, fewer sutures are necessary, the length of the operation time is shortened, and fewer post-operative infections occur. Fibrin glue applications are common in other important fields of clinical practice, including thoracic, orthopedic, neuro, and oral surgery^{28,30}.

4.2 Fabrication of scaffold based on fibrin

During this thesis, we fabricated scaffolds made of fibrin glue and fibrin gel. Fibrin glue was prepared using a 2 ml kit of Tisseel[®] (Baxter, Wien, Austria) composed of 95 mg fibrinogen and 500 U.I. thrombin stock solutions. We diluted the solution of fibrinogen at different final concentrations (Table 4.1- fibrin glue). The optimal concentration of fibrin was 10 mg/ml, 0.5 U.I thrombin and 50mM CaCl₂, because we are able to obtain the same degree of porosity and fiber diameter with both the fibrin glue with which the fibrin gel.

Fibrin gel was polymerized by combining the following components: fibrinogen from human plasma (>80% of protein is clottable), thrombin from human plasma >1,000 NIH units/mg protein and 50mM CaCl₂ (all products purchased from Sigma). Different concentrations were tested (see Table 4.1-fibrin gel) and the optimal concentration chose was the same of the fibrin glue.

Table 4.1 Fibrin Concentrations

FIBRIN GLUE		FIBRIN GEL	
Fibrinogen (mg/ml)	Thrombin (U.I.)	Fibrinogen (mg/ml)	Thrombin (U.I.)
10	0.5	10	0.5
40	30	10	30
40	3	40	3

Then, the two solutions of fibrin glue or fibrin gel were mixed in a 1:1 ratio to form the final fibrin. We fabricated two kinds of fibrin gel scaffolds: standing fibrin film and standing fibrin clot. Fibrin gel films have been used to observe the growth of cells on different random networks while fibrin gel clots have then been stretched to observe if the cells growth and migration is influenced by the mechanical orientation of the fibers³².

The film was fabricated using a glass substrate previously cleaned and coated with Teflon-AF to facilitate the release upon polymerization. A drop of fibrin gel solution was placed on the substrate in the centre of a confining Polydimethylsiloxane (PDMS) frame fabricated by replica moulding (see Chapter 2). Then, a second glass surface was placed on the top of the fibrin drop, without any additional pressure. The sample was incubated 24 hours at 4° C and the glasses were then removed, a film of fibrin enclosed in the PDMS frame and thus easy to handle was achieved (Figure 4.3a). These fibrin scaffolds were fixed and dehydrated as described in the chapter 2 for performing the microscopy characterization, figures 4.4-4.5 show the SEM and AFM micrographs of the films.

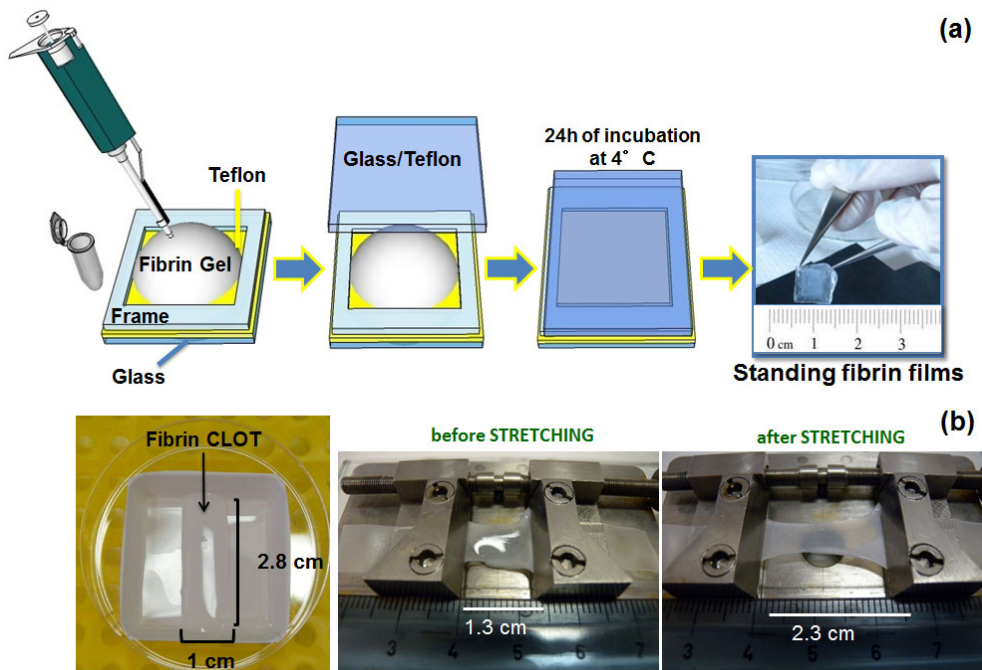


Figure 4.3: Scheme of scaffolds fabricated: (a) film, (b) clot.

The clot was fabricated again using PDMS to confine it but in this case the final result was not expected to stand within the frame, the latter was in act necessary only for shaping the clot. The solutions of fibrinogen and thrombin were mixed with the same procedure used to form the film (final volume: 2ml). The clot was maintained for 2 h at room temperature. It was then incubated for 24 h at 4°C before stretching. The concentrations used for the clot

were two: 10 mg/ml of fibrinogen and 0.5 U.I. of thrombin and 10 mg/ml of fibrinogen and 30 U.I. of thrombin.

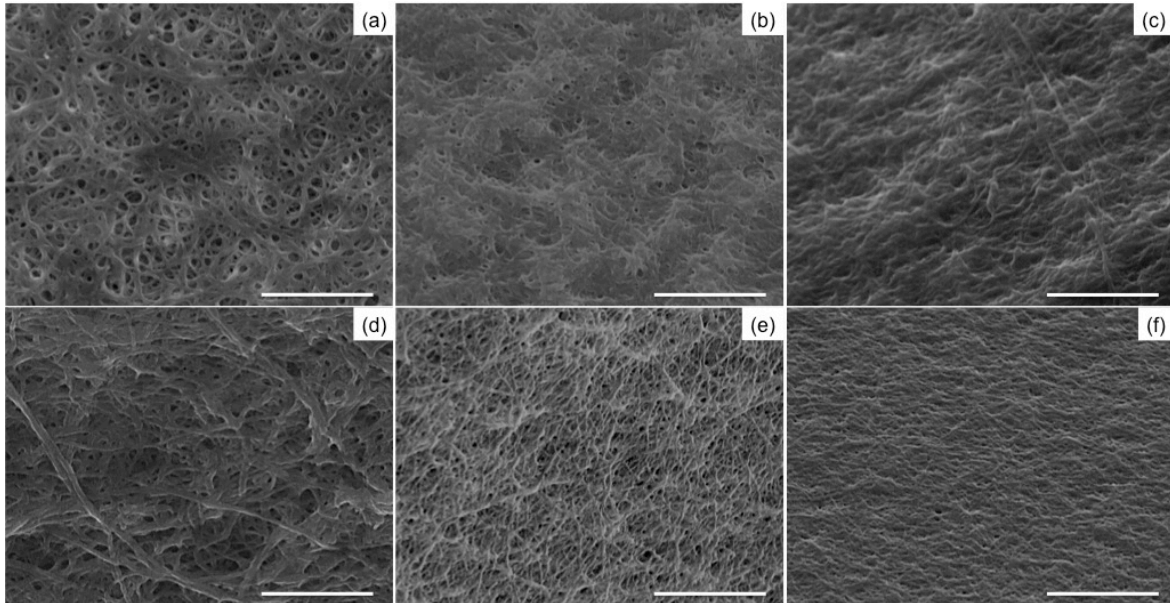


Figure 4.4: SEM micrographs with the morphology of fibrin glue (a) concentration 10 mg/ml + 0.5 U.I., (b) concentration 40 mg/ml + 30 U.I., (c) concentration 40 mg/ml + 3 U.I.; fibrin gel (d) concentration 10 mg/ml + 0.5 U.I., (e) concentration 10 mg/ml + 30 U.I., (f) concentration 40 mg/ml + 3 U.I. Scale 5 μ m

The fibrin clot was positioned within stretching devices (Figure 4.3b) and then the clots were subjected to mechanical stress with a controlled elongation (a spatial resolution of 0.1 mm) and force control. We have made tensile tests both in air and buffer. To measure the force required for the mechanical stress of clots, we tried to use INSTRON 4465. The INSTRON is a materials testing instrument designed to test the strength of a wide variety of materials. The system is made up of a load frame, in which a specimen of the test material is mounted, that applies a tension or compression load to the specimen, and a control console that provides the calibration, test setup, and test operating controls. The measures to Instron have not been successful, because the instrument has a minimum tensile force that does not fit our fibrin samples. The clots, once produced, are subjected to the mechanical stress along the longitudinal direction yielding about 1cm of elongation (Figure 4.3b); during this process they lose water, they become opaque, and microscopically the fibers of fibrin are aligned along a preferential direction (see Figure 4.6)³³.

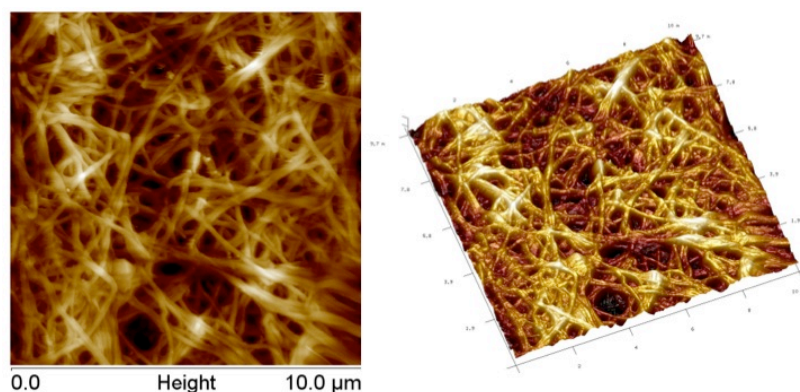


Figure 4.5: AFM micrographs with the morphology of fibrin gel (concentration 10 mg/ml + 0.5 U.I.)

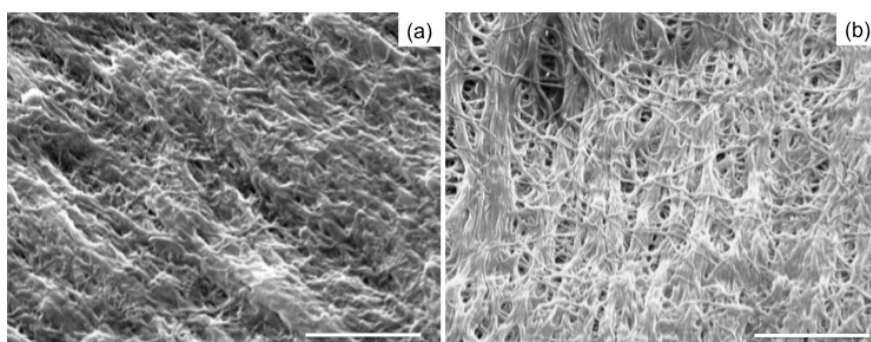


Figure 4.6: SEM micrographs with the morphology of fibrin gel clot (a) concentration 10 mg/ml + 0.5 U.I., (b) concentration 10 mg/ml + 30 U.I. Scale 5 μ m

4.3 Porosity analysis

One goal of these studies was to fabricate three-dimensional scaffolds with well-defined morphology. We employed SEM to qualitatively and quantitatively assess the physical architecture of the scaffolds.

To understand the morphology of fibrin network we calculated the Power Spectrum Density (PSD) of the images. PSD is the norm square of the Fourier transform of the image. From it the characteristic lengths of the image (ξ = correlation length) can be extracted and then quantitatively correlated with the morphological details present in the different images and samples. The analysis of the PSD is a robust method that provides a quantitative measure of the spatial distribution of the fibers. This method can be applied to the study of the morphological effects induced by different experimental parameters playing a role in the fibrin polymerization such as for instance ionic strength, temperature. It is also a versatile method because it can be applied to images obtained by any microscopy techniques, such as scanning electron microscopy or atomic force microscopy³⁴. The analysis of the PSD allows exploring a wide range of frequencies between $\nu_{\text{MIN}} = (1/L)$ where L is the size of the image and $\nu_{\text{MAX}} = (N/2L)$ where N is the number of pixels of the image. In order to carry out a consistent PSD based analysis it is important to capture images of the same size and resolution to always have the same information in terms of frequencies displayed by the PSD plots. In this case the PSD was performed on images obtained through scanning electron microscopy (SEM). From PSD it was possible to identify three correlation lengths ξ_1 , ξ_2 and ξ_3 corresponding to changes in the slope of the PSD in logarithmic scales, representing the characteristic lengths of the fiber network (fiber size, spacing)³⁴.

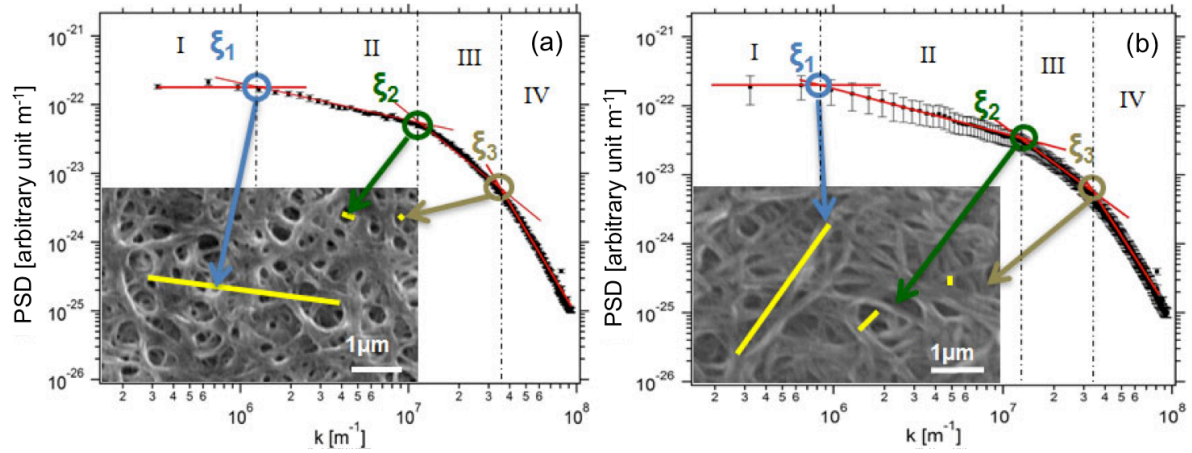


Figure 4.7: Power spectral densities vs wave vector (a) fibrin glue, $\xi_1 = 4.4\mu\text{m} \pm 0.5\mu\text{m}$, $\xi_2 = 0.5\mu\text{m} \pm 0.05\mu\text{m}$, $\xi_3 = 0.2\mu\text{m} \pm 0.02\mu\text{m}$; (b) fibrin gel, $\xi_1 = 4.7\mu\text{m} \pm 1.3\mu\text{m}$, $\xi_2 = 0.5\mu\text{m} \pm 0.02\mu\text{m}$, $\xi_3 = 0.2\mu\text{m} \pm 0.008\mu\text{m}$. The characteristic length scales reported in the figures are the average values estimated over different images. The error is the standard deviation.

In figure 4.7 the morphology of a fibrin glue film (Figure 4.7a) and a fibrin gel film (Figure 4.7b) is shown from SEM micrographs. The samples consist of interconnected and entangled fibres formed by fibrils of different width. The entanglement gives rise to a porous architecture whose multiscale porosity ranges from a few microns to a few hundreds nm. Figures 4.7c and d show the respective power spectral densities vs wave vector. It is evident that the PSDs are characterized by a sequence of distinct spectral regions: a saturated plateau at the lower wave vector range (region I); a decay with a small slope in double-log representation (region II), indicating a power law and separated from region III by a cross-over at 10^7 m^{-1} . This latter decay (region III) is interrupted at larger wave vector values by an additional increase of slope, with a cross-over of $3.5 \times 10^7 \text{ m}^{-1}$ (region III) to the final decay that displays an even steeper exponent (region IV). The crossover wave vectors separating the different regions (i-iv) mark the existence of three characteristic length scales. Their values, obtained by inverting the crossover wave vectors, is associated to the size (more precisely lateral length scale) of well-defined features that can be identified in the micrograph. These features are indicated with thick segments and arrows. They correspond to the larger pore size (viz. the cavities surrounded by bundled fibers with a low curvature), here indicated as ξ_1 , to the smaller pore size ξ_2 (viz. cavities enclosed by smaller fibers with high curvature), and the fibril width ξ_3 . The length scale ξ_1 can be regarded as related to the persistence length of the fibers. The same analysis was performed on all the different concentrations of the fibrin film and characteristics lengths are summarized in table 4.2.

Table 4.2 Correlation lengths fibrin film

Fibrinogen (mg/ml)	Thrombin (U.I.)	$\xi_1 \pm \text{SD} (\mu\text{m})$	$\xi_2 \pm \text{SD} (\mu\text{m})$	$\xi_3 \pm \text{SD} (\mu\text{m})$
10	0.5	4.7 ± 1.3	0.5 ± 0.02	0.2 ± 0.008
10	30	6.3 ± 0.2	1 ± 0.4	0.3 ± 0.01
40	3	2.4 ± 0.4	0.6 ± 0.3	0.2 ± 0.01

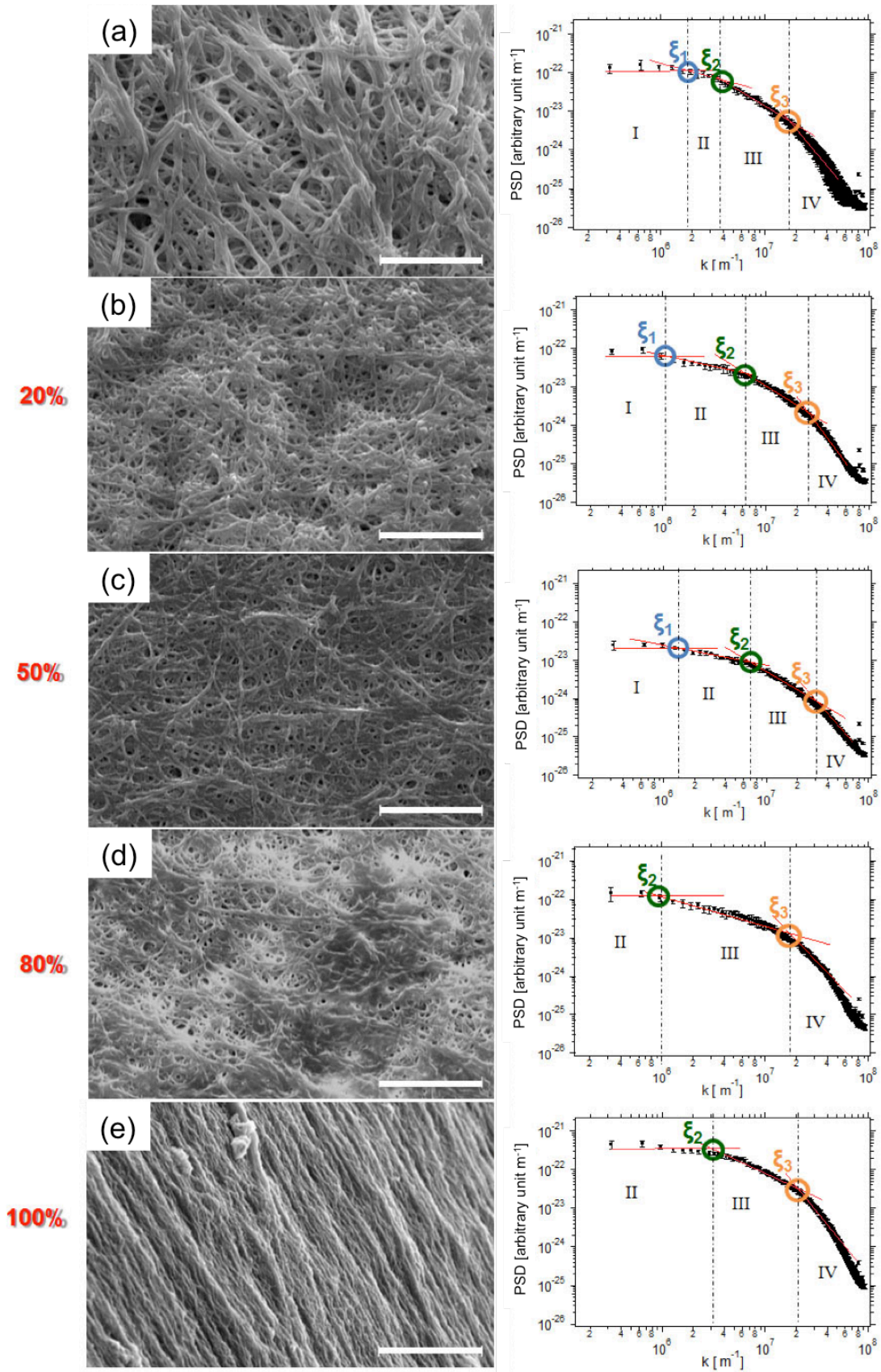


Figure 4.8: (left) SEM micrographs with the morphology of fibrin gel clot: (a) before stretching; (b,c,d,e) after stretching; (right) power spectral densities vs wave vector. The characteristic length scales reported in the figures are the average values over different images. The error is the standard deviation. Scale $10\mu m$

Figure 4.8 shows the SEM micrographs with their respective PSDs of fiber clot samples undergoing stretching. The labels indicate the percentile directly measured elongation of the sample. The evolution of the PSDs shows clearly that the three characteristic length scales shift systematically with the increasing elongation. From the analysis one can see that the first and the second correlation length of the network do not change up to an increase of the elongation of 20% and 50 while from 80% onwards ξ_2 varies substantially (see table 4.3). This is due to the fact that, in the latter case, the samples of fibrin are subjected to a greater mechanical stress, the fibers are align assuming a conformation similar to a rigid rod with a consequent increase of the parameter that is correlated to the persistence length; on the other hand the width of the fibers remains approximately equal to that of the previous samples, indicating that the stress applied is not enough to go to affect the conformation of the fibrin monomers that make up the fibers.

Figure	$\xi_1 \pm \text{SD} (\mu\text{m})$	$\xi_2 \pm \text{SD} (\mu\text{m})$	$\xi_3 \pm \text{SD} (\mu\text{m})$
4.3a	4.4 ± 0.5	0.5 ± 0.5	0.2 ± 0.02
4.3b (20%)	4 ± 1.4	0.9 ± 0.01	0.2 ± 0.02
4.3c (50%)	3.7 ± 0.8	0.7 ± 0.08	0.2 ± 0.02
4.3d (80%)	--	2.3 ± 0.9	0.2 ± 0.1
4.3e (100%)	--	0.5 ± 0.05	0.2 ± 0.02

4.4. Correlation of scaffold multiscale morphology and cell viability

We cellularised the two types of scaffolds: film and clot. We have used both fibroblast (NIH-3T3) and stem cells (Ne-4C). First of all we checked the stability of the fibrin gel in the medium, as it can be seen in figure 4.9.

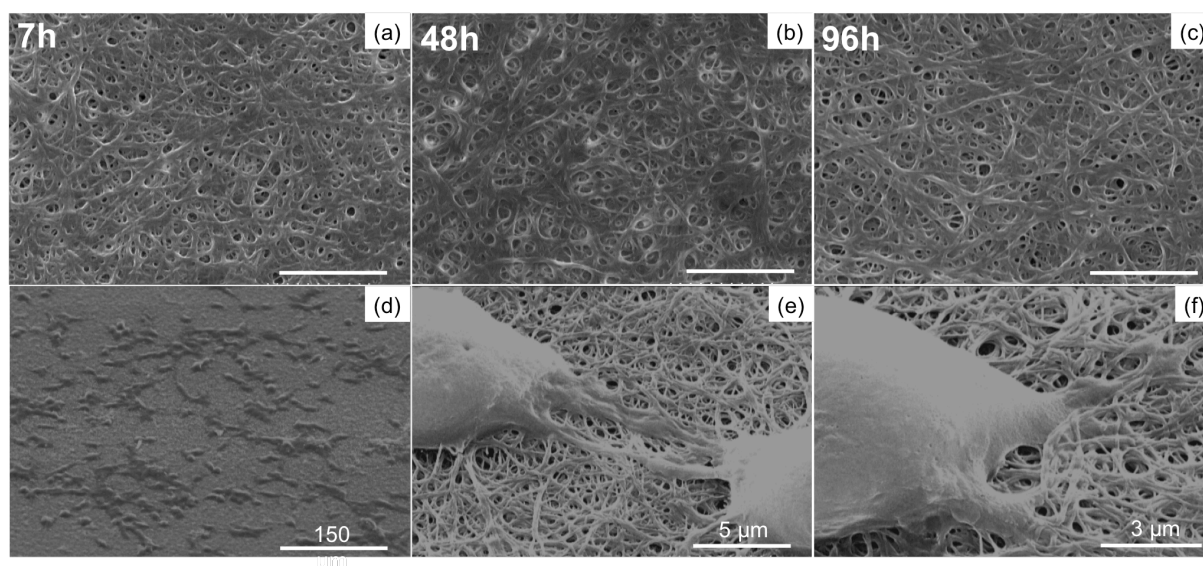


Figure 4.9: Stability of fibrin gel in cell culture medium: (a) 7h, (b) 48h, (c) 96h, scale 5 μm ; Ne-4C on fibrin glue film (d),(e) and (f).

Both cells line were incubated on the scaffolds under standard conditions (37 °C, 5% CO₂ and 95% relative humidity). They were seeded at 20,000 cells cm² on film. The samples were incubated with the cells 5h, 24h and 48h and then they were fixed following the standard protocol (see Chapter 2) to be observed by SEM. We have analyzed the images of fibrin network with cells incubated 5h and as one can see from the figure 4.9 f and g the porosity of fibrin network changes in the proximity of cells, this is because the cells apply a mechanical load on the fibers where they adhere thus locally distorting the network. Moreover cells during their growth cycle start to digest the fibrin as mentioned in the first paragraph of this chapter. In fact, in the samples incubated 24h the fibrin network around the cell can no longer be observed by SEM and at 48h we can only observe the cells with few fragments of fibers. We analyzed how the cell modifies the morphology of the fibrin network, figure 4.10 shows the respective power spectral densities vs wave vector. In this case we see that the first correlation length ξ_1 decrease compared to the one obtained in the samples without cells; this is likely to be due to the distortion of the fibers caused by cellular adhesion. In fact, in this case ξ_1 approaches the value of ξ_2 sample stretched to 80%.

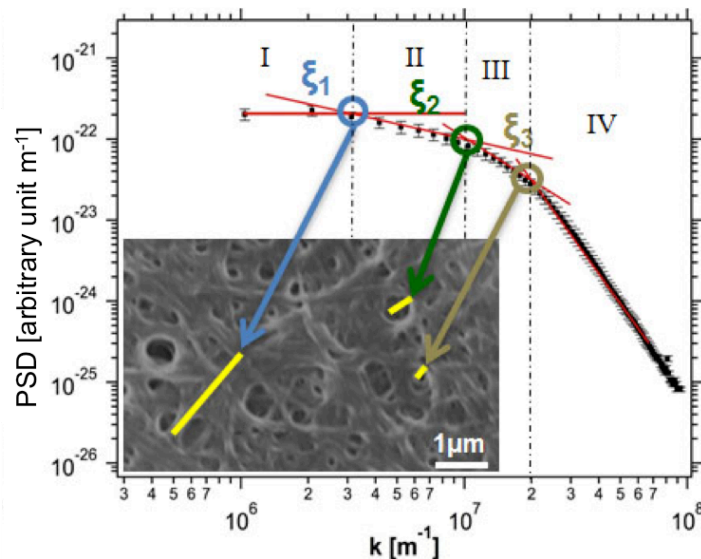


Figure 4.10: Power spectral densities vs wave vector. NE4C stem cells on fibrin gel; average PSDs of SEM images of in the proximity of cell adhesion loci $\xi_1 = 2.3\mu\text{m} \pm 0.1\mu\text{m}$, $\xi_2 = 0.5\mu\text{m} \pm 0.002\mu\text{m}$, $\xi_3 = 0.3\mu\text{m} \pm 0.008\mu\text{m}$. The characteristic length scales reported in the figures are the average values over different images. The error is the standard deviation.

Regarding clots after they were subjected to 100% of mechanical stress they were seeded with 50,000 cells cm²; in this way one wanted to verify if the cells are aligned along fibers. Samples were fixed after 5h, 24h (Figure 4.12) and 48h of cell incubation.

To perform properly the cell adhesion experiments, an appropriate PDMS sample holder have been fabricated that allowed to keep the sample under traction and at the same time accommodate the solution containing the cell culture medium without dehydrating them (Figure 4.11). The wires were included in the frame to facilitate its handling.

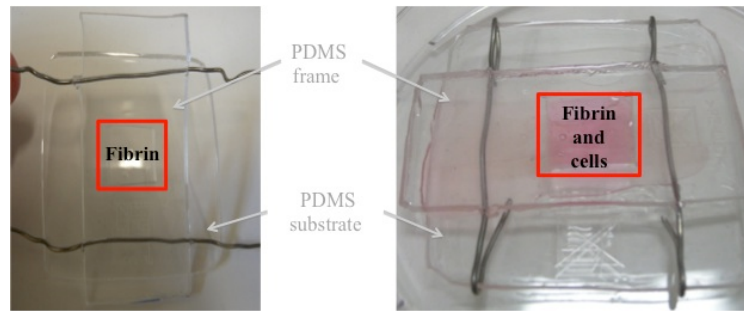


Figure 4.11: PDMS frame for confinement of cells

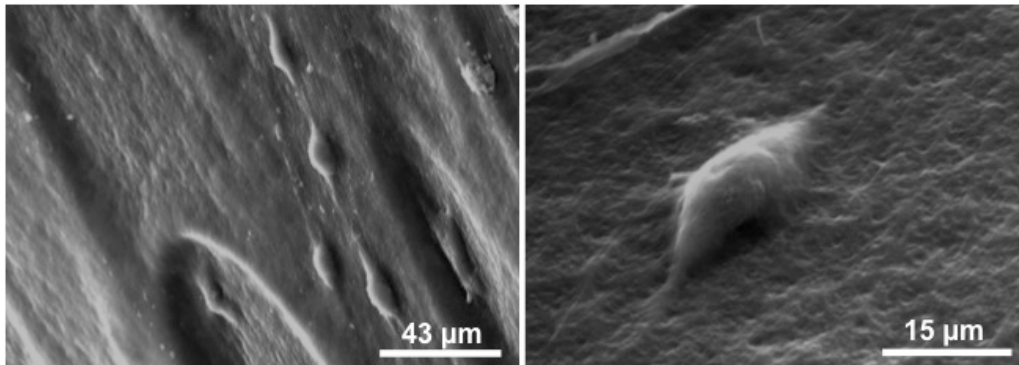


Figure 4.12: Cells adhesion to 24h on fibrin clots elongated to 100%. The images show the adhesion and growth of cells (Ne-4C) long fiber alignment.

4.5 Conclusions

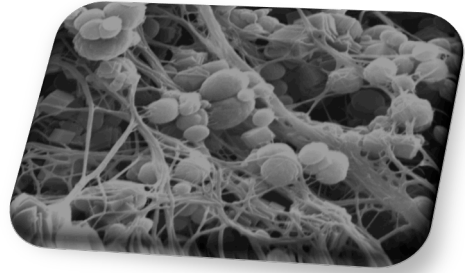
In this part of the work, we have fabricated two types of scaffolds and we have observed cell growth both on scaffolds with random orientation and on substrates manufactured with a preferred orientation. An important goal of this work was to fabricate 3D scaffolds with a well-defined morphology to be used as a starting point for the regeneration of portions of urethral tissue. In this frame the realization of a fibrin scaffold, of different thickness and easy to handle fabricated under controlled spatial confinement has been demonstrated.

The mechanical properties of the gel were studied, applying mechanical stress to the clots and determining the elongation and conformational properties using advanced image analysis of electron microscope micrographs. Furthermore, we have verified that keeping constant the concentration of fibrinogen and varying the concentration of thrombin, we are able to obtain a scaffold with different elastic properties and morphology. The fibers actually align in a preferential direction during stress. The characterization of the fibrin network by SEM has helped us to understand how the morphology of fibrin network might affect the cell growth and how the cells distort the network by adhering on the samples (see figure 4.12). An accurate morphological analysis based on the "power spectral density" (PSD) is crucial for all the results reported here, because it allows to quantitatively characterize the morphology of the network that we have fabricated. The different correlation lengths that are provided by this analysis are important first of all because they represent useful numerical parameters to be associated with the network distortion and because they describe morphological properties that must be fitted for cell proliferation for instance a large enough porosity to permit the cell migration and the diffusion of signalling molecules and nutrients and a network dense enough to allow the development a good number points of adhesion for each cell (cell 5-10 μ m).

Bibliography

- 1 Hudak, S. J., Atkinson, T. H. & Morey, A. F. Repeat Transurethral Manipulation of Bulbar Urethral Strictures is Associated With Increased Stricture Complexity and Prolonged Disease Duration. *J Urology* **187**, 1691-1695, (2012).
- 2 Mundy AR, A. D. "Urethral strictures" (BJU 2011).
- 3 Brandes, S. B. & Morey, A. F. *Advanced male urethral and genital reconstructive surgery*. (Human Press, 2014).
- 4 Gargollo, P. C., Cai, A. W., Borer, J. G. & Retik, A. B. Management of recurrent urethral strictures after hypospadias repair: Is there a role for repeat dilation or endoscopic incision? *J Pediatr Urol* **7**, 34-38, (2011).
- 5 Moniruzzaman, M., Faruquzzaman & Mohiuddin, T. Urethral stricture in adult as a consequence of childhood hypospadias repair. *Bratisl Med J* **112**, 530-534, (2011).
- 6 Barbagli, G. & Lazzeri, M. Surgical treatment of anterior urethral stricture diseases: brief overview. *International braz j urol : official journal of the Brazilian Society of Urology* **33**, 461-469, (2007).
- 7 Hameed, A., Mohammed, A., Nasir, S. & Plamer, M. Management of bulbar urethral strictures: review of current practice. *Can J Urol* **18**, 5676-5682, (2011).
- 8 Kotov, S. V. & Belomyttsev, S. V. [Oral mucosa transplantation in extended urethral stricture]. *Urologiia*, 78-82, (2011).
- 9 Riechardt, S. & Fisch, M. Two-stage urethroplasty with buccal mucosa. *BJU international* **109**, 150-162, (2012).
- 10 Zimmerman, W. B. & Santucci, R. A. Buccal mucosa urethroplasty for adult urethral strictures. *Indian journal of urology : IJU : journal of the Urological Society of India* **27**, 364-370, (2011).
- 11 De Luca, M., Pellegrini, G. & Green, H. Regeneration of squamous epithelia from stem cells of cultured grafts. *Regen Med* **1**, 45-57, (2006).
- 12 Pellegrini, G., Rama, P., Mavilio, F. & De Luca, M. Epithelial stem cells in corneal regeneration and epidermal gene therapy. *J Pathol* **217**, 217-228, (2009).
- 13 Ahmed, T. A., Dare, E. V. & Hincke, M. Fibrin: a versatile scaffold for tissue engineering applications. *Tissue engineering. Part B, Reviews* **14**, 199-215, (2008).
- 14 Uibo, R. *et al.* Soft materials to treat central nervous system injuries: evaluation of the suitability of non-mammalian fibrin gels. *Biochimica et biophysica acta* **1793**, 924-930, (2009).
- 15 Shaikh, F. M. *et al.* Fibrin: a natural biodegradable scaffold in vascular tissue engineering. *Cells, tissues, organs* **188**, 333-346, (2008).
- 16 Ye Q, Z. G., Benedikt P, *et al.* . Fibrin gel as a three dimensional matrix in cardiovascular tissue engineering. *European Journal of Cardio-thoracic Surgery* **17**, 587-591, (2000).
- 17 Bensaïd, W. *et al.* A biodegradable fibrin scaffold for mesenchymal stem cell transplantation. *Biomaterials* **24**, 2497-2502, (2003).
- 18 Laurens, N., Koolwijk, P. & de Maat, M. P. Fibrin structure and wound healing. *Journal of thrombosis and haemostasis : JTH* **4**, 932-939, (2006).
- 19 Mosesson, M. W. Fibrinogen and fibrin structure and functions. *Journal of thrombosis and haemostasis : JTH* **3**, 1894-1904, (2005).
- 20 Lee, M. G. & Jones, D. Applications of fibrin sealant in surgery. *Surgical innovation* **12**, 203-213, (2005).

- 21 Ariens, R. A., Lai, T. S., Weisel, J. W., Greenberg, C. S. & Grant, P. J. Role of factor XIII in fibrin clot formation and effects of genetic polymorphisms. *Blood* **100**, 743-754, (2002).
- 22 Muszbek, L., Yee, V. C. & Hevessy, Z. Blood coagulation factor XIII: structure and function. *Thrombosis research* **94**, 271-305, (1999).
- 23 Wolberg, A. S. Thrombin generation and fibrin clot structure. *Blood reviews* **21**, 131-142, (2007).
- 24 Weisel, J. W. Fibrin assembly. Lateral aggregation and the role of the two pairs of fibrinopeptides. *Biophysical journal* **50**, 1079-1093, (1986).
- 25 Weisel, J. W. & Nagaswami, C. Computer Modeling of Fibrin Polymerization Kinetics Correlated with Electron-Microscope and Turbidity Observations - Clot Structure and Assembly Are Kinetically Controlled. *Biophys. J.* **63**, 111-128, (1992).
- 26 Albala, D. M. Fibrin sealants in clinical practice. *Cardiovasc Surg* **11**, 5-11, (2003).
- 27 Fattahi, T., Mohan, M. & Caldwell, G. T. Clinical applications of fibrin sealants. *J Oral Maxil Surg* **62**, 218-224, (2004).
- 28 Jackson, M. R. Fibrin sealants in surgical practice: An overview. *Am J Surg* **182**, 1s-7s, (2001).
- 29 MacGillivray, T. E. Fibrin sealants and glues. *J Cardiac Surg* **18**, 480-485, (2003).
- 30 Spotnitz, W. D. Commercial fibrin sealants in surgical care. *Am J Surg* **182**, 8s-14s, (2001).
- 31 Dunn, C. J. & Goa, K. L. Fibrin sealant - A review of its use in surgery and endoscopy. *Drugs* **58**, 863-886, (1999).
- 32 Brown, A. E., Litvinov, R. I., Discher, D. E., Purohit, P. K. & Weisel, J. W. Multiscale mechanics of fibrin polymer: gel stretching with protein unfolding and loss of water. *Science* **325**, 741-744, (2009).
- 33 Dubey, N., Letourneau, P. C. & Tranquillo, R. T. Neuronal contact guidance in magnetically aligned fibrin gels: effect of variation in gel mechano-structural properties. *Biomaterials* **22**, 1065-1075, (2001).
- 34 Calo, A., Stoliar, P., Bystrenova, E., Valle, F. & Biscarini, F. Measurement of DNA morphological parameters at highly entangled regime on surfaces. *J Phys Chem B* **113**, 4987-4990, (2009).



Chapter 5

Enhancing fibrin scaffold functionality with drug delivery

Drug delivery systems enable the modulation and the localization of the release of therapeutic agents. The main function of a drug delivery system is to carry biological active agents. Material selection plays an important role when designing sustained release drug delivery systems. It is necessary to understand the characteristics of the desired material, including biocompatibility and biodegradability, as well as the chemical, physical, morphological and surface properties as all of them affect the release of the incorporated bioactive agents^{1,2}. One of the aims of a controlled release system is to provide a sustained dosage of the incorporated agents over an extended time by reducing the initial burst release. This chapter describes the fabrication of a bioactive fibrin scaffold where microcrystals of calcium carbonate loaded with retinoic acid were incorporated to obtain its controlled release.

5.1 Introduction

The application of fibrin in tissue engineering can be grouped into three main areas: fibrin as cell matrix material alone, fibrin as a cell matrix material combined with a polymeric scaffold, and as delivery system for growth factors or other therapeutic agents. A simple method for the use of fibrin as a scaffold material involves suspending primary or expanded cells in a component of the fibrin gel, as it has been described in chapter 4. The resulting three-dimensional scaffold may be cultivated *in vitro* to obtain an adequate tissue for re-implantation. In addition to the application as scaffold *in vitro*, the fibrin system can also be used as cell delivery vehicle *in vivo*. Cells suspended in fibrin can be directly injected into a defect in a minimally invasive procedure with little stress for the patient; the fibrin gel can be polymerized *in vivo* in the desired three-dimensional shape, at the same time ensuring the retention of the cells at the injection site^{3,4}.

An alternative strategy for tissue engineering is the combination of hydrogels with polymeric scaffolds. Highly porous solid scaffolds can provide sufficient load-bearing capacity for the process of implantation and for structural integrity *in vivo*. However, many scaffold systems lack adequate cell seeding efficiency, sufficient cell distribution and subsequent sufficient extracellular matrix synthesis and deposition. In contrast, fibrin gels generally incorporate all of the applied cells and enable a good cell distribution providing the requirements for a coherent tissue development, but often lack adequate biomechanical strength and volume stability^{5,6}. Therefore, the advantages of fibrin combined with favourable characteristics of

synthetic or naturally derived polymeric scaffolds can be utilized to develop a simple, stable composite for implantation. Following this approach tissue development with the desired three-dimensional shape can be achieved; furthermore the time for tissue development may be reduced as compared to the use of either system alone⁷. This strategy has been successfully applied in tissue engineering of urothelium^{8,9}, and cardiovascular engineering⁷.

Fibrin can also be applied as delivery system for the release of growth factors, cytokines or other bioactive molecules to control cell adhesion, proliferation, migration, differentiation, and matrix production. Many growth factors bind to fibrin, bFGF and VEGF are even supposed to bind specifically. Alternatively, such proteins can be incorporated into the gel during polymerization^{10,11}. Furthermore, when applied *in vivo*, the presence of the growth factor in the defect is maintained over a long time. Additionally, the kinetics of growth factor release can be controlled by varying fibrinogen and thrombin concentration as well as by the addition of degradation inhibitors. Factors released from fibrin gels used for tissue regeneration include bFGF, VEGF, NTF, ECGF, GDNF and NGF^{10,12}.

Hubbell et al. developed an innovative technology for growth factor delivery on the basis of a combination of fibrin and heparin, utilizing the ability of heparin to stabilize the bioactivity of growth factors and control their release¹³.

Andree et al. established a method to deliver EGF expression plasmids from a fibrin matrix to a human keratinocyte culture system. These plasmids can enhance keratinocyte proliferation during expansion *in vitro* as well as directly after transplantation of the cells in combination with a fibrin matrix into a skin defect *in vivo*. Unfortunately, the time span of release from fibrin hydrogels is rather short due to the fast diffusion of the small molecules^{14,15}.

In this work, we wanted to include retinoic acid (RA) in the scaffold. RA is a factor used for the differentiation of neural stem cells. Retinoic acid (RA), a potent metabolite of vitamin A, acts as a growth and differentiation factor in many tissues. In vitamin A adequacy, RA is present in plasma at nanomolar concentrations, and thus circulating leukocytes are continuously exposed to low levels of RA¹⁶. Most of the biological actions of RA are mediated by two families of nuclear retinoid receptors¹⁷. The binding of RA to nuclear transcription factors of the RA receptor (RAR) and retinoid X receptor (RXR) families enables these receptors to induce the transcriptional activation of a wide range of retinoid-responsive genes¹⁷. The ability of retinoids to regulate cell growth and promote cell differentiation has been established in numerous cell culture and animal models. Cell growth and differentiation are tightly controlled processes that co-ordinately maintain normal tissue homeostasis. The decision of cells to differentiate is commonly made in the G1 phase of the cell cycle, and the induction of differentiation is believed to require cell cycle arrest^{18,19}. However, despite a general understanding that retinoids often induce cells to cease or slow their rate of proliferation and to assume a more mature phenotype, there is still little specific knowledge of how RA can induce the arrest of the cell cycle, and co-ordinately, activate a program of cell-type specific differentiation.

In the present study, we have manufactured bioactive scaffold of fibrin loading retinoic acid in microcrystals of calcium carbonate that were then embedded in fibrin scaffold that we

have described in the chapter 4. We have decided not to incorporate retinoic acid directly into fibrin, because we wanted the release of the RA not to happen immediately in a single burst. The formation of calcium carbonate minerals (e.g. calcite) occurs in a wide range of natural environments (e.g. soils and calcifying marine plankton), and is a key component of the global carbon cycle²⁰. The formation of crystalline calcium carbonate polymorphs (calcite, vaterite and aragonite) during biomineralization often occurs via a nano-particulate Amorphous Calcium Carbonate (ACC) precursor²¹. The crystallization of ACC to calcite enables organisms to form biominerals with complex morphologies and crystals with defined crystallographic orientations. In recent years these bio-mineralisation processes have stimulated significant interest due to their potential to be mimicked and applied to form industrial products with specific particle shapes²². Also, these calcium carbonate transitions can be utilized to incorporate proteins (e.g. insulin) into the final crystalline phase for potential drug delivery applications²³. However, the nanoscale mechanisms of the calcium carbonate crystallization pathways are still poorly defined. Furthermore, there are currently no quantitative kinetic models to describe the transformation from ACC to crystalline calcite at ambient conditions. This is despite the fact that such information is crucial for understanding the physical and chemical conditions which lead to calcium carbonate bio-mineralisation or the production of particles with specific shape/size for industrial applications²⁴. In the present study, neuroectodermal stem cells (Ne4C) and human neuroblastoma cells (SH-SY5Y) were used, in minimal essential medium as described in chapter 2 to see if the delivery of RA from the calcite carriers could induce their differentiation.

5.2 Blending retinoic acid into fibrin scaffolds with calcium carbonate microcrystals: modulation of neuronal stem cell differentiation

Initially, we differentiated both cell lines using the fibrin film produced as described in the chapter 4 only as a supporting scaffold. We seeded 25,000 cells per cm², as required by the protocol of differentiation; after 4 hours from sowing, the time required for cell adhesion, we induced differentiation by replacing the medium with differentiation medium composed of DMEM F-12 Ham (1:1), 1X ITS, 4mM glutamine, 40µg ml⁻¹ gentamicin and 2.5µg ml⁻¹ amphotericin (DM), containing all-trans retinoic acid (RA), 1µM. After two days, the DM was replaced by DM containing 40ng ml⁻¹ neurotrophic brain-derived factor (BDNF). Half of the DM was then changed every day by subsequent replacing it with DM, without any inducers until the end of the experiment. As a control, the same differentiation protocol was applied in parallel to cells seeded on glasses inserted in a 24-multiwell plate. After 8 days of differentiation, we characterized the samples using the protocol of immunofluorescence staining of β-tubulin III, performed as previously described (see Chapter 2) co-labeling the nuclei with DAPI. In figure 5.1 the obtained results are reported.

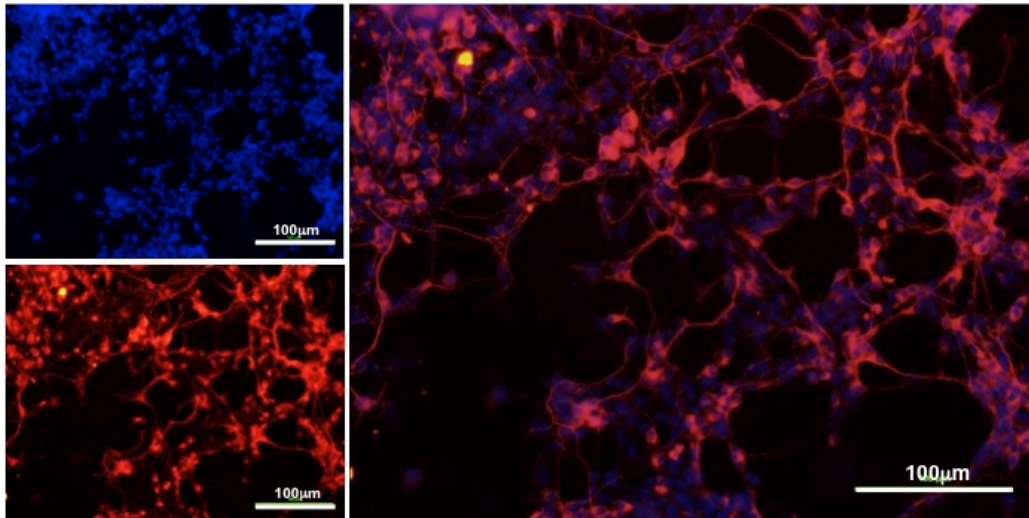


Figure 5.1: Immunofluorescence images: cell differentiation day 8 through retinoic acid with a concentration of 1 μM. The images show the formation of the neuronal network of Ne4C in astrocytes.

Subsequently, we have incorporated the RA to a final concentration of 1 μM directly in the fibrinogen solution subsequently combined with thrombin, as described in the previous chapter. After 24h of polymerization at 4 °C we cellularised the samples. We seeded 25,000 cells per cm², but the release of retinoic acid has occurred too quickly and differentiation of cells has been only partially achieved. To slow down the release of retinoic acid through the fibrin, we decided to incorporate retinoic acid in crystals of calcite and vaterite.

This work was developed in collaboration with Prof. Giuseppe Falini, Dr. Matteo Calvaresi and Matteo Di Giosia Department "G. Ciamician" University of Bologna, who have provided us with RA crystals embedded.

The microcrystals were prepared by rapid mixing equal volumes (2ml) of CaCl₂ and Na₂CO₃ aqueous solutions, 1 mL of retinoic acid was added to the latter. Typically, 0.5 M CaCl₂ was rapidly poured into an equal volume of 0.5 M Na₂CO₃ solution at room temperature. After vigorous agitation with a magnetic stirrer, the precipitate was filtered off, thoroughly washed with pure water, and dried in air. In figure 5.2, the characterization of crystals of calcite and vaterite with incorporated retinoic acid have been reported. The concentrations of retinoic acid used are 200 μM, 40 μM and 8 μM. Differentiation assays were performed with both the previously mentioned cell lines.

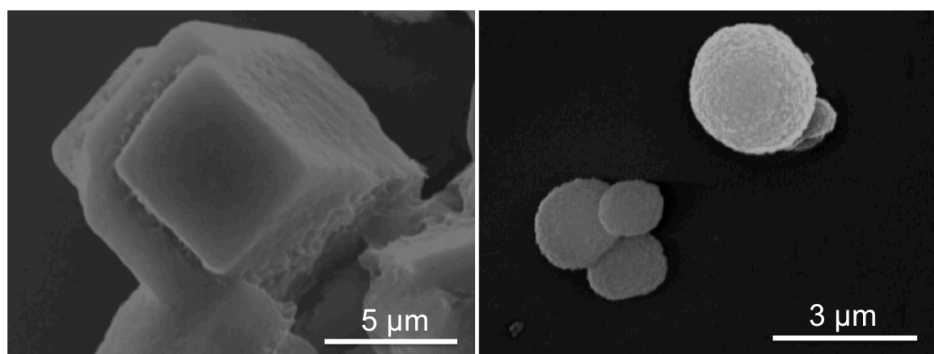


Figure 5.2: SEM images: Crystals of (right) calcite (left) vaterite with 200 μM concentration of retinoic acid.

The differentiation of NE-4C/SH-SY5Y cells into a densely interconnected neuronal network on the scaffold has been successfully achieved. The addition of the neurotrophic brain-derived nerve growth factor (BDNF) after 2 days from retinoic acid exposure was used to improve the survival of newly born neurons and to promote the neurite maturation.

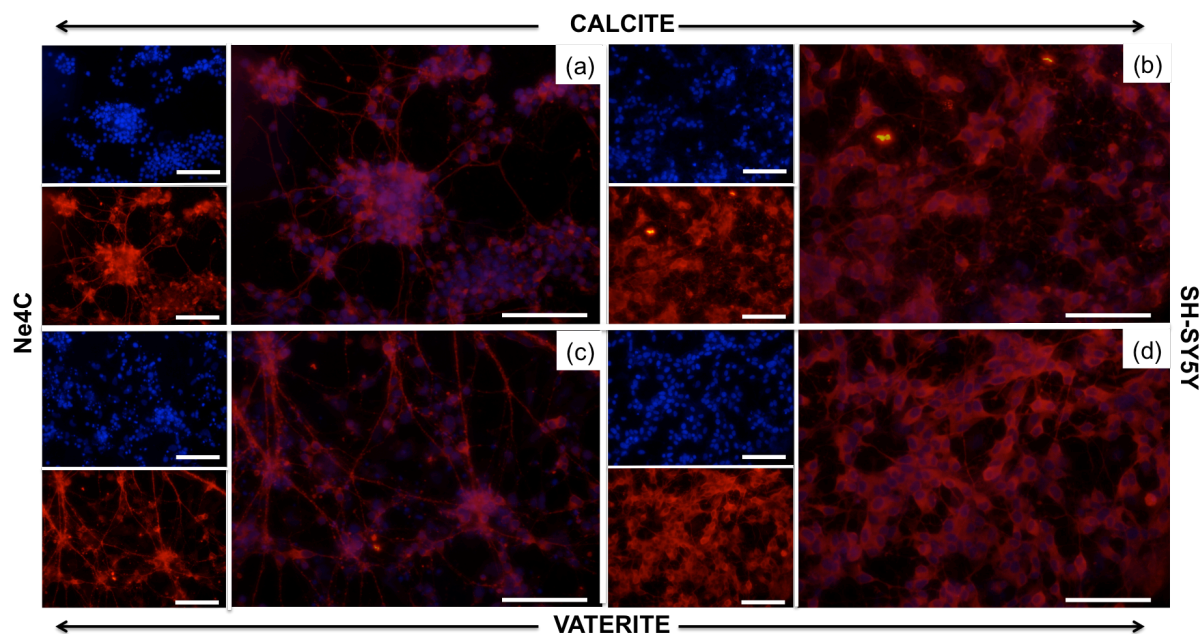


Figure 5.3: Immunofluorescence images: cell differentiation day 8 through retinoic acid with a concentration of 200 μ M incorporated in the crystals. (a) and (c) show the formation of the neuronal network of Ne4C in astrocytes, (b) and (d) show the differentiation of SH-SY5Y cells into neurons.

During the course of the differentiation process, we observed progressive cell morphological changes. After prolonged time of incubation (from day 5) developed neuronal processes are visible and the active areas are almost completely covered by a dense layer of mature neuronal cells. Figure 5.3 show typical fluorescence microscopy results of the neuronal network at eight days upon induced differentiation (day 8) after co-staining using specific probes. The blue colour (DAPI) marks the nuclei of all the cells. The differentiation is visualized by the specific labelling of III β -tubulin, a typical marker of neuronal processes (red). This clearly demonstrates the differentiation of the majority of cells and the formation of a dense neuronal network with long and interconnected neuronal filaments. These images show that there is also a substantial growth of the network in presence of microcrystal.

To confirm the result obtained by the release of RA by means of the crystals of calcite and vaterite, we have carried out tests of control. Figures 5.4 and 5.5 show respectively the results obtained by differentiating the cells with crystals and giving RA directly in solution (top); as one can notice, there are no differences compared to the results obtained by incorporating RA in crystals and this corroborates the results we got. In figures 5.4 and 5.5 it is shown that in the presence of crystals without RA both cell lines continue to proliferate as stem cells with no differentiation. As these images were obtained at the end of the days of differentiation, they also reveal that the neurite processes are still attached to the area of the microcrystals, indicating that the presence of calcium does not negatively affect the cell viability and the neuronal maturation.

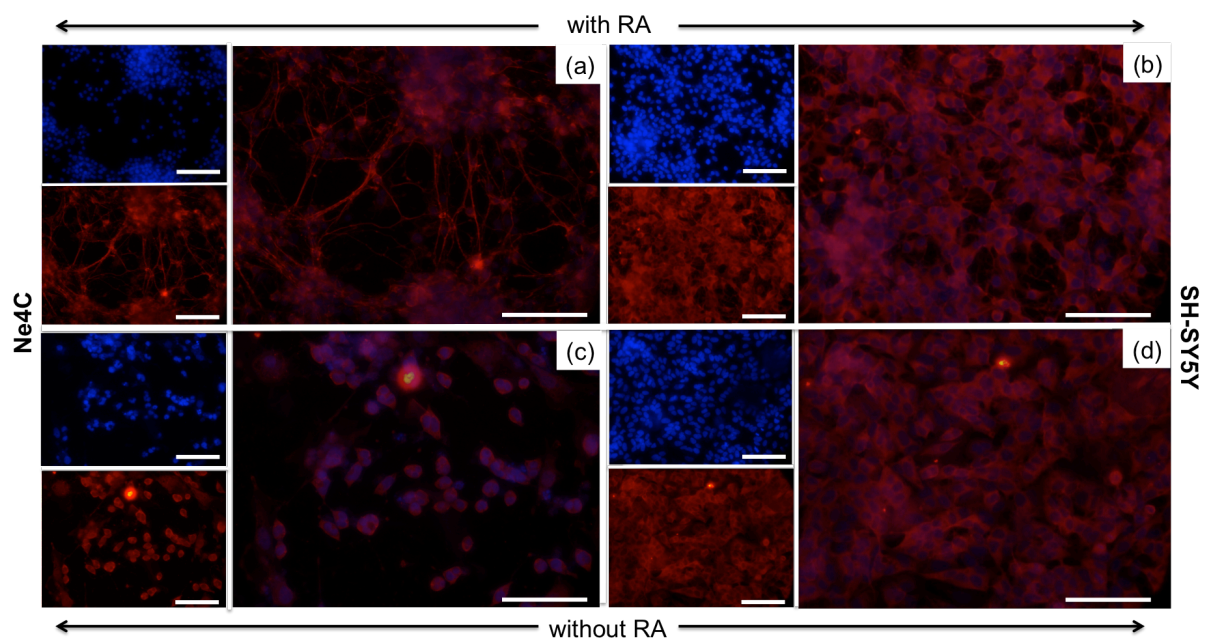


Figure 5.4: Immunofluorescence images: cell differentiation day 8 through retinoic acid with a concentration of $1\mu\text{M}$ in solution in the presence of calcite crystals; (a) show the formation of the neuronal network of Ne4C in astrocytes, (b) show the differentiation of SH-SY5Y cells into neurons; (c) and (d) show the cells after 8 days of incubation without retinoic acid in the presence of calcite crystals.

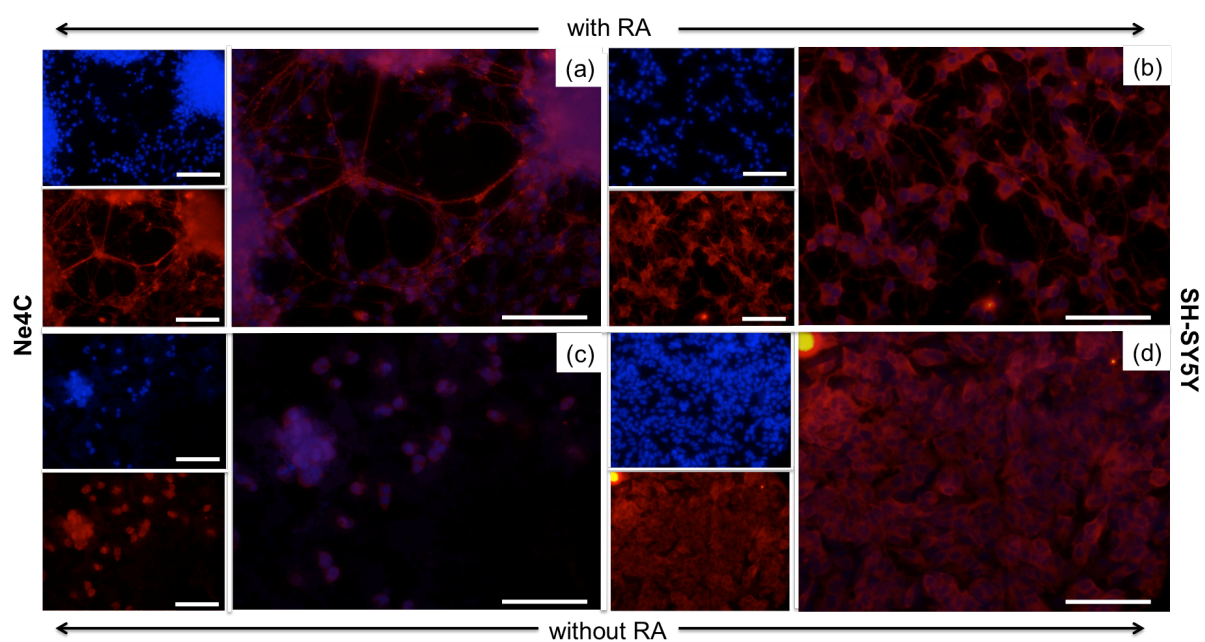


Figure 5.4: Immunofluorescence images: cell differentiation day 8 through retinoic acid with a concentration of $1\mu\text{M}$ in solution in the presence of vaterite crystals; (a) show the formation of the neuronal network of Ne4C in astrocytes, (b) show the differentiation of SH-SY5Y cells into neurons; (c) and (d) show the cells after 8 days of incubation without retinoic acid in the presence of vaterite crystals.

The successful development of a functional neuronal network by the release of drugs from the crystals of calcite and vaterite on both cell lines has been thus demonstrated. The next step was to incorporate the crystals with RA in the films of fibrin. The crystals were incorporated in the film after 1h of polymerization of the fibrin gel, then the samples were covered with

cells. In Figure 5.6 we reported the characterization of the samples of fibrin with microcrystals performed by SEM imaging.

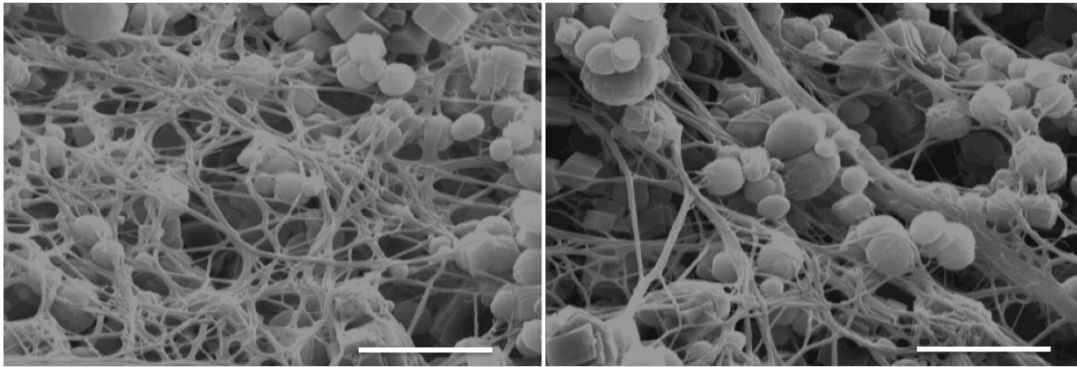


Figure 5.6: SEM images: fibrin with microcrystal. Scale bar 10 μ m

After the polymerization time of fibrin with microcrystals, we have sown the usual number of Ne4C cells on the fibrin film. After two days of incubation, we added BDNF as before and on the eighth day of differentiation the co-staining was done as in the samples described above. Figure 5.7 shows the stem cells differentiated into astrocytes through the calcite crystals with 200 μ M incorporated RA.

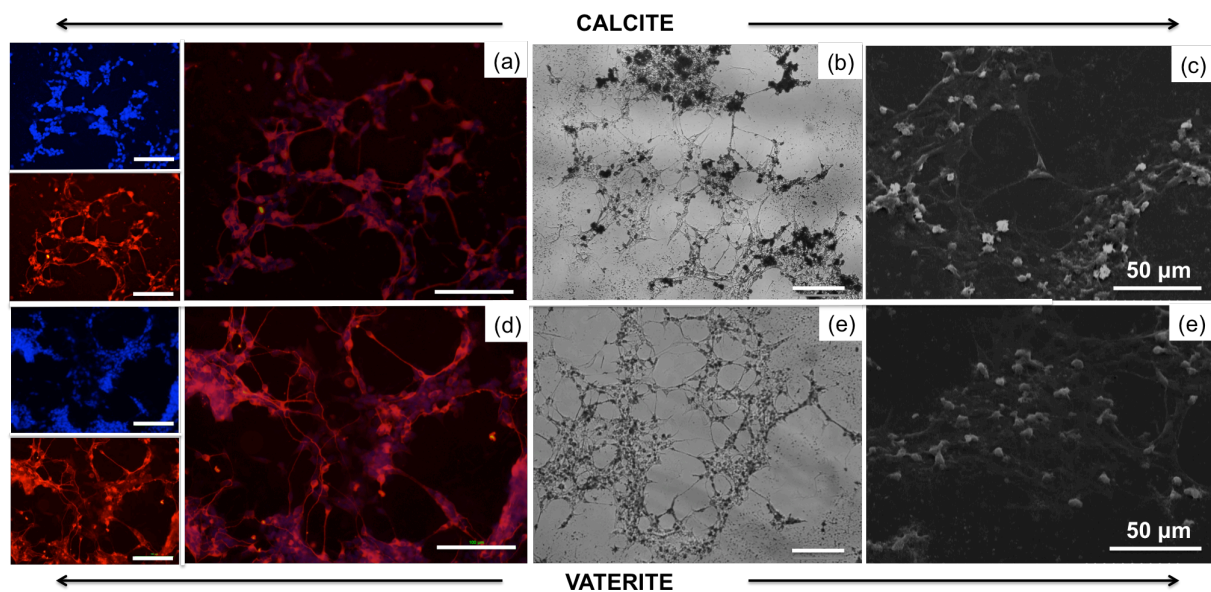


Figure 5.7: Ne4C cell differentiation day 8 through retinoic acid with a concentration of 200 μ M incorporated in the crystals. Immunofluorescence images: (a) and (d), optical images: (d) and (e), SEM images: (c) and (e) show the formation of the neuronal network of Ne4C in astrocytes. Scale bars 100 μ m

As these images were obtained at the end of the differentiation, they also reveal that the neurite processes are still attached to the area of the microcrystal, indicating that the of calcium present both in the crystals and in the fibrin does not negatively affect the cell viability and the neuronal maturation. Instead, the fibrin film with incorporated RA loaded vaterite microcrystals gave different results. In fact, after the six days of incubation, the cells were killed by alteration of calcium osmosis. The lowest concentration that the cell in extracellular environment can stand ranges from 2 to 2.5mM^{25,26} in the presence of vaterite

crystals with the calcium present in the fibrin, the concentration of calcium appears to be about 25mM. A high concentration of calcium in the cell can cause lipid peroxidation, oxidative stress or of cellular membrane block of ion pumps.

5.3 Conclusions

Our results demonstrate a strategy for fabricating a bioactive scaffold composed of fibrin and microcrystals of calcite loaded with RA. This approach aims at combining the versatility of fibrin as a material for scaffold fabrication with the possibility to release in a time and position controlled way molecules required for tuning the cell fate. Specifically here a suitable material for obtaining a well defined neural interface has been shown. In the literature there are many works that show the fibrin to be how the release of growth factors, antibiotics and chemotherapeutics from a fibrin gel can be useful in clinical applications^{14,15}. Unfortunately, the time of release from fibrin hydrogel is rather short because of the rapid diffusion of small molecules. In this work we have used microcrystals of calcium carbonate to have a more controlled release. Different applications of microcrystals of calcium carbonate can be envisioned, for example, they can be used to encapsulate drugs and then incorporated in a layer of polyelectrolyte to have a controlled release in the gastric fluid²⁷. The proposed work is alternative method for drug delivery that can be used in tissue engineering applications. There are still many challenges which must be addressed to make the delivery system more successful for the desired treatment. Different approaches, including both affinity-based delivery systems and reservoir-based systems, still provide some challenges that need to be overcome. For both types of delivery system, minimizing the initial burst release is a key factor. One of the remaining challenges is the characterization of these systems in long-term injury models with an appropriate assessment of the functional recovery.

For future applications one may be required to combine different delivery systems along with cell therapies to be more effective against neural disorders. Moreover the illustrated strategy can be a starting point for fabricating multifunctional devices by tailoring the chemical, physical and morphological properties of the device thus providing cues for directing cell behaviour in tissue engineering applications.

Bibliography

- 1 Davis , H. E. & Leach, J. K. Designing bioactive delivery systems for tissue regeneration. *Ann. Biomed. Eng.* **39** 1–13, (2010).
- 2 Thompson, B. C. Optimising the incorporation and release of a neurotrophic factor using conducting polypyrrole *J. Control. Release* **116** 285–294, (2006).
- 3 Bensaïd, W. *et al.* A biodegradable fibrin scaffold for mesenchymal stem cell transplantation. *Biomaterials* **24**, 2497-2502, (2003).
- 4 Fussenegger, M. *et al.* Stabilized autologous fibrin-chondrocyte constructs for cartilage repair in vivo. *Annals of plastic surgery* **51**, 493-498, (2003).

- 5 Jockenhoevel, S. *et al.* Fibrin gel - advantages of a new scaffold in cardiovascular
tissue engineering. *European journal of cardio-thoracic surgery : official journal of*
6 *the European Association for Cardio-thoracic Surgery* **19**, 424-430, (2001).
- 7 Peretti, G. M., Randolph, M. A., Villa, M. T., Buragas, M. S. & Yaremchuk, M. J. Cell-
based tissue-engineered allogeneic implant for cartilage repair. *Tissue Eng* **6**,
567-576, (2000).
- 8 Mol, A. *et al.* Fibrin as a cell carrier in cardiovascular tissue engineering
applications. *Biomaterials* **26**, 3113-3121, (2005).
- 9 Ameer, G. A., Mahmood, T. A. & Langer, R. A biodegradable composite scaffold for
cell transplantation. *Journal of orthopaedic research : official publication of the*
Orthopaedic Research Society **20**, 16-19, (2002).
- 10 Wechselberger, G. *et al.* Fibrin glue as a delivery vehicle for autologous urothelial
cell transplantation onto a prefabricated pouch. *The Journal of urology* **160**, 583-
586, (1998).
- 11 Sahni, A., Odriljin, T. & Francis, C. W. Binding of basic fibroblast growth factor to
fibrinogen and fibrin. *The Journal of biological chemistry* **273**, 7554-7559, (1998).
- 12 Wong, C., Inman, E., Spaethe, R. & Helgerson, S. Fibrin-based biomaterials to
deliver human growth factors. *Thrombosis and haemostasis* **89**, 573-582, (2003).
- 13 Ehrbar, M., Metters, A., Zammaretti, P., Hubbell, J. A. & Zisch, A. H. Endothelial cell
proliferation and progenitor maturation by fibrin-bound VEGF variants with
differential susceptibilities to local cellular activity. *Journal of controlled release :
official journal of the Controlled Release Society* **101**, 93-109, (2005).
- 14 Jeon, O., Ryu, S. H., Chung, J. H. & Kim, B. S. Control of basic fibroblast growth
factor release from fibrin gel with heparin and concentrations of fibrinogen and
thrombin. *Journal of controlled release : official journal of the Controlled Release
Society* **105**, 249-259, (2005).
- 15 Spicer, P. P. & Mikos, A. G. Fibrin glue as a drug delivery system. *J. Controlled
Release* **148**, 49-55, (2010).
- 16 Mohtaram, N. K., Montgomery, A. & Willerth, S. M. Biomaterial-based drug
delivery systems for the controlled release of neurotrophic factors. *Biomed Mater*
8, (2013).
- 17 Soderlund, M. B., Sjoberg, A., Svard, G., Fex, G. & Nilsson-Ehle, P. Biological
variation of retinoids in man. *Scandinavian journal of clinical and laboratory
investigation* **62**, 511-519, (2002).
- 18 Altucci, L. & Gronemeyer, H. Nuclear receptors in cell life and death. *Trends in
endocrinology and metabolism: TEM* **12**, 460-468, (2001).
- 19 Ohnuma, S., Philpott, A. & Harris, W. A. Cell cycle and cell fate in the nervous
system. *Current opinion in neurobiology* **11**, 66-73, (2001).
- 20 Zhu, L. & Skoultschi, A. I. Coordinating cell proliferation and differentiation.
Current opinion in genetics & development **11**, 91-97, (2001).
- 21 Reeder, R. Reviews in Mineralogy. *Mineralogical Society of America* **11**, 394,
(1983).
- 22 Weiner, S., Sagi, I. & Addadi, L. Choosing the crystallization path less traveled.
Science **309**, 1027-1028, (2005).
- 23 Meldrum, F. C. & Ludwigs, S. Template-directed control of crystal morphologies.
Macromol Biosci **7**, 152-162, (2007).
- 24 Fujiwara, M. *et al.* Encapsulation of Proteins into CaCO₃ by Phase Transition from
Vaterite to Calcite. *Cryst Growth Des* **10**, 4030-4037, (2010).

- 24 Meldrum, F. C. & Colfen, H. Controlling Mineral Morphologies and Structures in Biological and Synthetic Systems. *Chem Rev* **108**, 4332-4432, (2008).
- 25 Boron, W. F. B., Emile L. *Medical Physiology: A Cellular And Molecular Approach*. (Elsevier/Saunders, 2003).
- 26 Warren, L. *Review of medical microbiology and immunology*. (McGraw-Hill Medical, 2008).
- 27 Wang, C. *et al.* Combination of adsorption by porous CaCO₃ microparticles and encapsulation by polyelectrolyte multilayer films for sustained drug delivery. *International journal of pharmaceutics* **308**, 160-167, (2006).



Chapter 6

Chitin 3D-scaffold for cornea regeneration

In the previous chapter we have fabricated a scaffold using a bottom up strategy. In this chapter we propose, in the perspective of Cornea regeneration, an alternative strategy for fabricating scaffolds starting from materials manufactured by nature. We used a scaffold of chitin directly coming from the pen of the squid. The scaffold of chitin was treated in order to tune the chemical and physical properties and then used for cell adhesion and proliferation.

6.1 Introduction

The human eye is a complex structure designed to gather a significant amount of information about the environment around us. The eye is housed in a cavity called the eyeball or orbit, within the skull. The space between the globe and the orbit is coated with a layer of connective tissue known as fascia bulbar¹. This, on the whole, has the function to support, protect and stabilize the eye, providing a cavity suitable to the rotation. The link between the eyeball and the central nervous system is achieved through the optic nerve. The walls of the globe are formed from three distinct layers of tissue: an outer layer scleral/corneal, an intermediate vascular/choroidal and an inner retinal. The human ocular surface is covered by corneal, limbal and conjunctival squamous epithelia (Figure 6.1a). The corneal epithelium is flattened, transparent and stratified; it contains a basal layer of cuboidal cells lying on the Bowman's membrane (smooth layer located between the epithelium and the stroma in the cornea. It is composed of collagen fibers and helps the cornea maintain its shape) of an avascular corneal stroma. Corneal renewal and repair are executed by stem cells located in the limbus, the narrow zone between the cornea and the bulbar conjunctiva (Figure 6.1a,b)². Relatively undifferentiated slow-cycling epithelial cells have been found in the limbal basal layer but not in the central cornea^{3,4}. Cells migrate from the limbus towards a wounded cornea⁵; mathematical analyses of the maintenance of the corneal epithelial cell mass⁶ and the mosaic analysis of stem cell function and corneal wound healing⁷ support the hypothesis that the corneal epithelium is regenerated by limbal stem cells. In the absence of a functional limbus, repeated corneal wounds result in progressive vascularization and recurrent erosions of the cornea, confirming that the corneal epithelium *per se* has a limited regenerative capacity⁸.

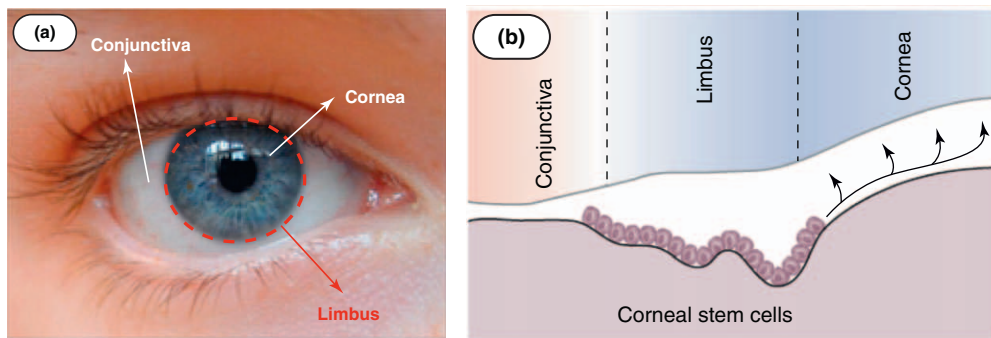


Figure 6.1: Corneal stem cells. (a) The location of the limbus on the ocular surface. (b) Diagram showing the location of the limbus as well as the migration and differentiation of the limbal stem cells to form the corneal epithelium.

During normal homeostasis, the murine central corneal epithelium could be self-sustaining and limbal stem cells might be recruited only after corneal injury⁹. So far, however, human corneal stem cells have been exclusively found in the limbus^{9,10}. The transparency of the cornea, which depends on stromal avascularity and epithelial integrity, is essential to visual acuity. Ocular chemical or thermal burns can destroy the limbus, causing limbal stem cell deficiency (LSCD). Because the corneal epithelium can no longer be formed, the cornea acquires an epithelium by the invasion of bulbar conjunctival cells that originate beyond the destroyed limbus. This process leads to neovascularization, chronic inflammation, severe symptoms, corneal opacity and the loss of vision. In a pathological cornea, the regular arrangement of the collagen fibrils is perturbed and the tissue's optical properties become strongly scattering (see Figure 6.2)^{11,12}. Sclera is already strongly scattering in its healthy state. While the exact relation between tissue structure and transparency is subject to debate, it is clear that the intensity of the scattering processes strongly decreases with increasing wavelength (Figure 6.2)¹³.

Allogeneic corneal transplantation also known as keratoplasty, is a surgical procedure where a damaged or diseased cornea is replaced by donated corneal tissue (the graft) in its entirety (penetrating keratoplasty) or in part (lamellar keratoplasty). It is aimed at replacing the scarred corneal stroma and the inner endothelium and it is not always a successful treatment. Although it temporarily removes the opacity, the conjunctival cells will resurface the cornea. The only way to prevent this invasion is to restore the limbus, which can be attained in unilateral LSCD through the grafting of limbal fragments from the uninjured eye¹⁴. The discovery that limbal cultures¹⁵ contain stem cells¹⁰ inspired the first therapeutic use of such cultures for the regeneration of a functional corneal epithelium¹⁶. Trypsinized cells of a single limbal biopsy of 1–2 mm² are cultivated on a feeder layer of lethally irradiated clinical grade [(GMP (good manufacturing practice)-certified] 3T3- J2 cells in the presence of an appropriately selected fetal calf serum. The subconfluent primary culture is trypsinized, a portion of the cells is transferred to a secondary culture on a fibrin disc of 3 cm diameter (on 3T3- J2 feeder cells)^{17,18} and the remainder are cryopreserved. When the secondary culture is confluent it is grafted over the corneal and limbal region of the injured eye, whose receiving bed had previously been surgically prepared by the removal of the abnormal epithelium and fibrovascular tissue¹⁸.

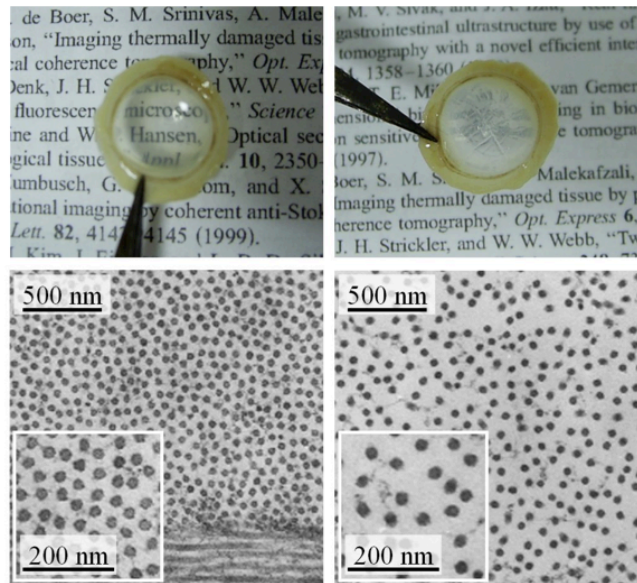


Figure 6.2: (left) The regular arrangement of the collagen fibrils in the volume of healthy cornea is responsible for its transparency. (right) Most reasons for corneal grafting involve edema (corneal swelling), which perturbs the regular fibril structure and leads to strong optical scattering¹³.

This procedure reduces the loss of uninjured limbus and offers a therapeutic option to patients with severe bilateral corneal epithelial loss. Approximately 15 years have passed since the first application of cultured limbal grafts to regenerate a corneal epithelium of patients suffering from LSCD¹⁶. Subsequent related studies^{19,20} have been limited by comparatively small numbers of cases, heterogeneous etiology, limited follow-up (often less than one year) and heterogeneous sources of transplant and cell culture. Cells have been cultured on a variety of substrates and culture media in the presence or absence of feeder cells. Patients have been treated with autologous or allogeneic limbal or oral cells. In these studies, stringent quality criteria for limbal cultures were not adopted. Although the procedures were often successful, it is not surprising that failures were reported and data were difficult to interpret.

In this work we propose an alternative transparent scaffold to serve as support for the limbal cells that are essential for the regeneration of the cornea.

The material proposed is naturally produced by nature and will represent an important alternative to the bottom-up strategy followed in the previous chapters. The idea below this novel approach is the following: upon a specific request for a regenerative medicine scaffold many possible materials matching these properties can be found in nature with the obvious advantage to be abundant and extremely biocompatible. In the present example, the material for fabricating a corneal scaffold must be transparent and mechanically resistant; the former properties is trivial to be understood the second is because it must withstand the suturing process during the surgery. In nature it exist a material perfectly matching these properties: the chitin constituting the squid pen²¹ (Figure 6.3). In addition it is biocompatible and low-cost.



Figure 6.3: (a), (b) Feather-shaped internal structure that supports the squid's mantle and serves as a site for muscle attachment; (c) transparency of squid pen.

6.2 Changing the physical chemical properties: squid pen deacetylation

From a molecular point of view, chitin is very similar to cellulose, with the difference of an acetamide or an amine group replacing the C-2 hydroxyl group of each glucose unit. Chitin (at any degree of deacetylation) takes a 2/1-helical symmetry with a repeating period of about 10 Å²². In the case of the deacetylated version of the polymer (i.e., chitosan), several crystalline polymorphic forms have been reported, with the differences being limited to the water content and packing density.

From a biological point of view, chitin played a very important role during the Cambrian explosion, being the structural material that conveyed stiffness and mechanical stability to the hard structures of many organisms. Currently, it appears in such different organisms as crustaceans, mollusks, and fungi, in three different polymorphic forms: β -chitin, α -chitin, and γ -chitin, which are β and α polymorphs analogues to cellulose types I and II, respectively²².

α -Chitin is by far, the most abundant crystalline form of chitin in nature. It is present in fungal and yeast walls, as well as arthropod exoskeletons. In this polymorphic form, the chitin chains are organized in sheets of antiparallel chains (a sort of molecular zipper), which are held by a large number of intra-sheet hydrogen bonds. In this polymorph, the sheets are also bound together, a feature not present in β -chitin²². This difference motivates the reference to α -chitin as a “3D” polymorph, in contrast with the “2D” nature of the β -chitin.

β -Chitin is formed by parallel aligned chains. The lack of inter-sheet bonds makes it more susceptible to swelling, and its natural form is a crystalline hydrate. While lacking the stability of α -chitin, β -chitin has a unique ability to incorporate small molecules other than water in the crystal lattice, and it is able to form crystal complexes with other components, such as alcohols or aliphatic amines²³. β -Chitin is found, for example, in the organic matrix of nacre, in the spines of diatoms, and in the squid pen²⁴. The third polymorph, γ -chitin, is the rarest and least characterized form. Initially discovered in the stomach of some squids, it also was found later in the cocoons of some beetles. This chitin form is usually described as a combination of the previous two, where each sheet is composed of repeats containing two parallel chains separated by an antiparallel chain²⁵.

The worldwide production of chitin has been estimated to be between 10¹⁰ and 10¹² tons/year making this natural biomarine raw material one the most abundant by products of industrial use²⁶.

The pens were provided to us by the group of prof. Falini “G. Ciamician” department of the University of Bologna. The species we have chosen is the *Loligo vulgaris*. The pens have been subjected to alkaline hydrolysis, in a 1M NaOH²⁴ solution for a total time of 2, 4, 6, 24 and 48 h. The removal of protein is indicated by absence of any colour in the medium at the end of the treatment. The pens extracted were washed with cold distilled water and then immersed in three different baths of distilled water at 100 degrees for 10 minutes each. The pens were then cut into two strips by removing the central thicker portion. Square specimens of 1 cm² were obtained from the strips.

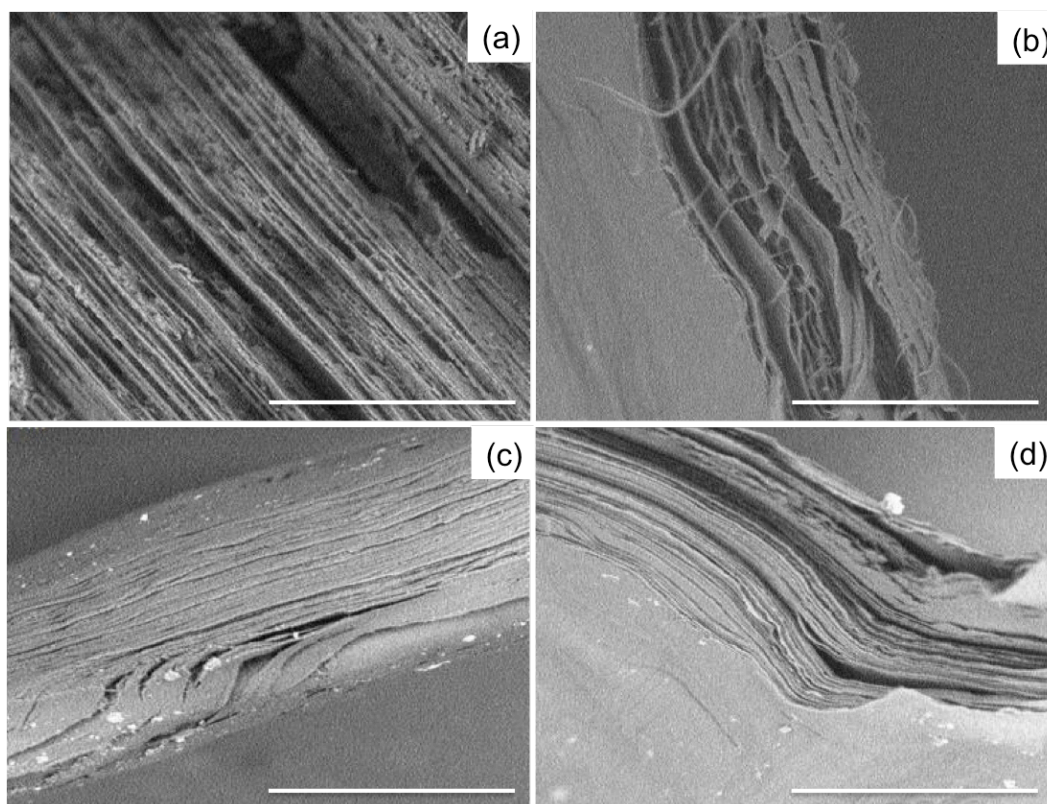


Figure 6.4: SEM images: Squid Pen (a) untreated;(b) 2h NaOH 1M;(c) 4h NaOH 1M;(d) 6h NaOH 1M. Scale bar 40µm.

Elemental analysis allowed the determination of the average degree of acetylation (DA) of the chitin samples. The formula used:

$$DA(\%) = \left[\frac{\left(\frac{C}{N} - 5.14 \right)}{1.72} \right] * 100$$

where the C/N ratio was calculated by elemental analysis²⁷. The degrees of acetylation obtained respectively for each treatment time were: 97, 96, 88, 85 and 83%. The pens were initially characterized using a scanning electron microscope Phenom Pro, which allows to observe the sample using backscattered electrons without any metal coating.

Figure 6.4, shows the SEM-Phenom micrographs of the samples before (Figure 6.4a) and after the treatment of alkaline hydrolysis (Figure 6.4b,c,d). Few protein residues can be seen

before the treatment. In addition, we may note the lamellar structure of the chitin layers. Figure 6.5 shows in detail the chitin fibers present on the pen after after 24h of the treatment.

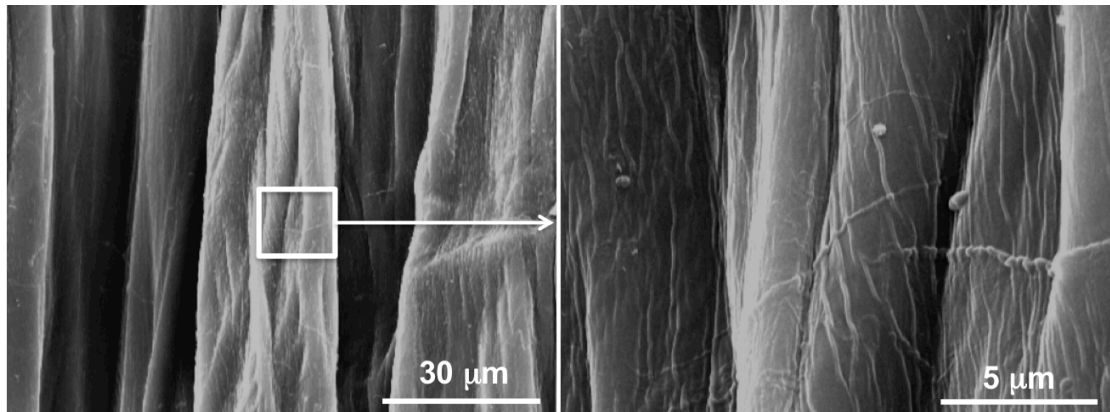


Figure 6.5: High resolution images of chitin fibers.

6.3 Cell adhesion on squid pen

After the partial deacetylation of the chitin scaffold, we performed adhesion assays to evaluate the behavior of cells. The samples were sterilized by autoclave²⁸. NIH-3T3 fibroblast cells were randomly seeded onto the substrates and let adhere under standard cell culture conditions in the presence of serum-containing medium. These cells were chosen because they are closely related to those used in regenerative medicine application as feeder layers. The adhered cells were counted at 3h, 6h, 9h upon seeding for all the different deacetylation times. To visualize their shape, optical micrographs were collected as reported in figure 6.6. To visualize the nuclei, the cells were fixed and subsequently stained with the specific nuclei dye DAPI.

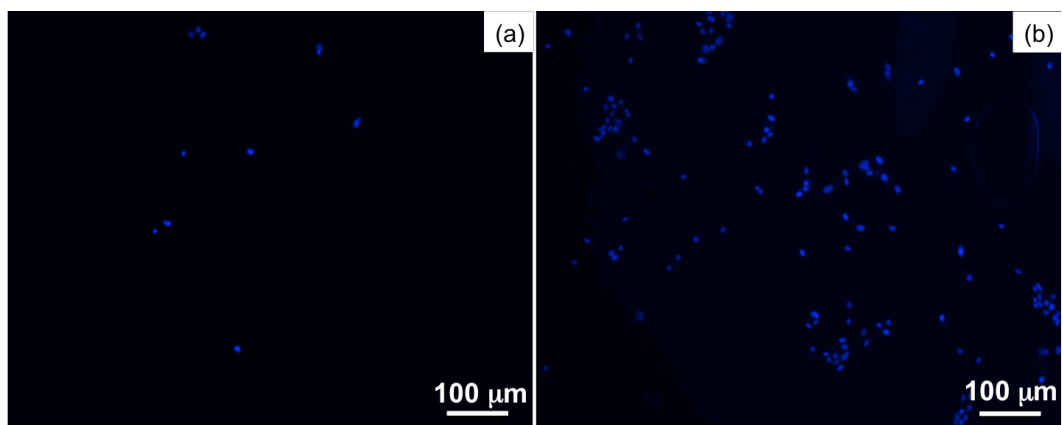


Figure 6.6: Optical and fluorescence micrographs of NIH-3T3 cells after 3h of incubation under standard cell culture conditions. Nuclei of cells stained with DAPI on squid pen treated (a) 2h NaOH 1M (b) 6h NaOH 1M.

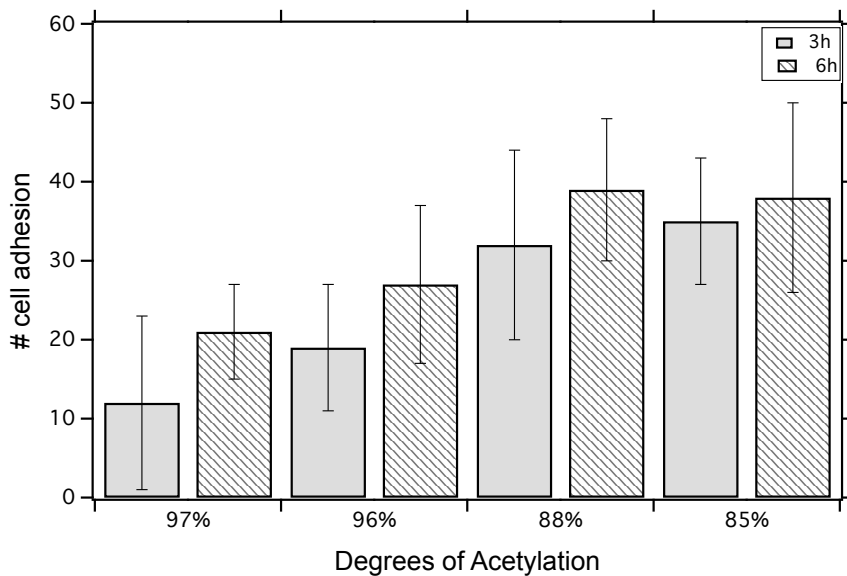


Figure 6.7: The graph shows the adhesion of cells, incubated for 3h and 6h, versus the degree of acetylation.

Figure 6.7 shows the number of adherent cells versus the chitin deacetylation time. One can notice that cellular adhesion increases with the deacetylation²⁹. This is likely to be due to an increase of amino groups.

The subsequent step was to verify the proliferation of cells. In this case we stopped the samples after 24h of culture. Figure 6.8 shows a good cell coating on the chitin scaffold.

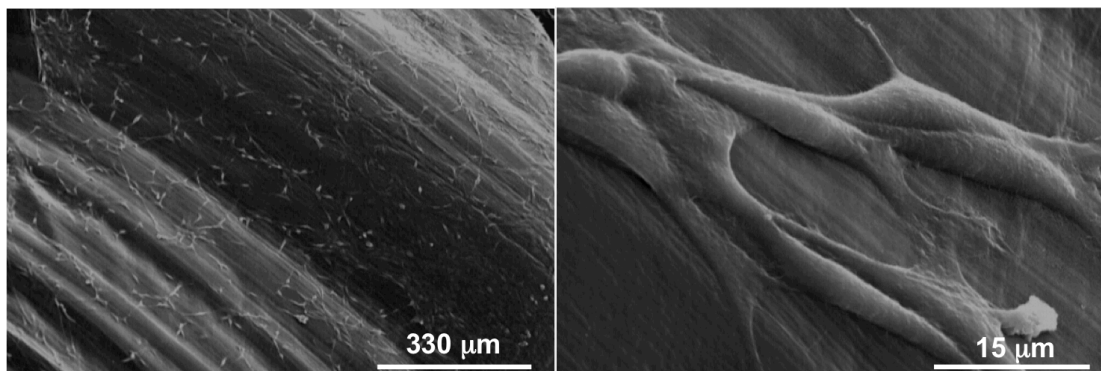


Figure 6.8: The SEM images show the adhesion of the Fibroblast (NIH-3T3) on squid pen after 24h of incubation.

A possible strategy to increase the adhesion of cells on scaffolds is to functionalize its surface. Following the indications of Prof. Graziella Pellegrini from the center for regenerative medicine “Stefano Ferrari” at the University of Modena, fibrin has been chosen because of its current in clinical phase; other proteins such as laminin or fibronectin that are usually employed to favour cell adhesion have been discarded because they would not be allowed in therapeutic applications. Pre-treated squid pen samples were immersed in a solution of fibrin using an initial concentrations of 10 mg/ml of fibrinogen and 0.5 IU of thrombin. In figure 6.9 it is shown the characterization of the scaffold coated with fibrin, in the same figure a direct fluorescence imaging of actin has been performed showing the adhesion points of cell to the chitin scaffold. It can be noted how the presence of fibrin facilitates the adhesion and proliferation of cells (Figure 6.9).

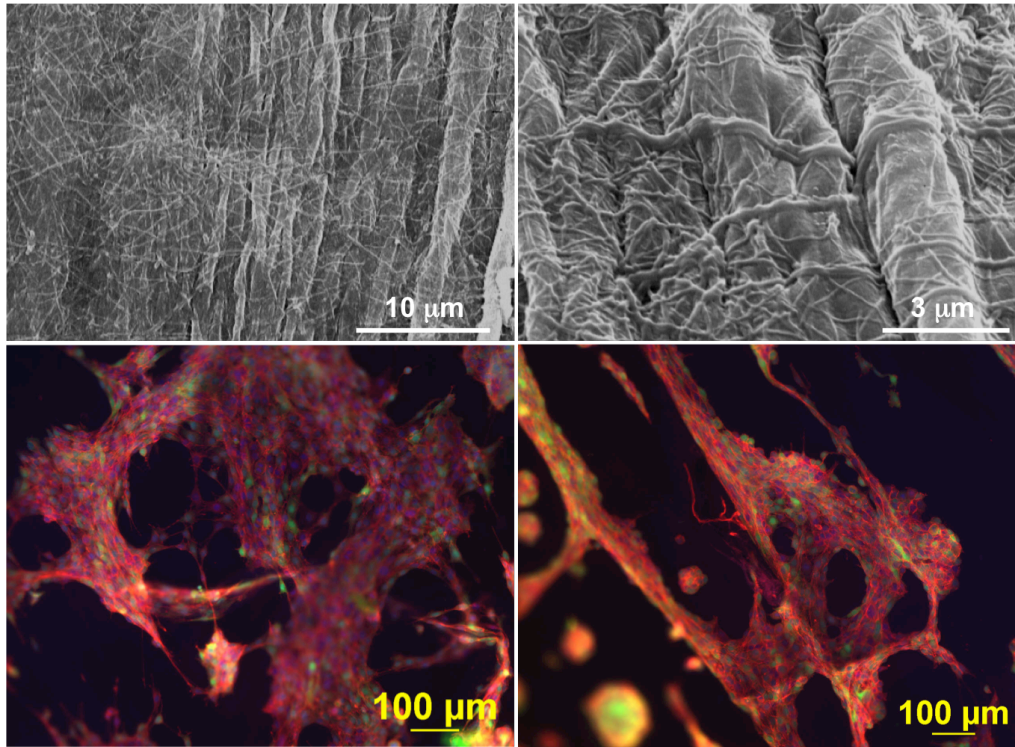


Figure 6.9: SEM images: a),b) fibrin network on squid pen; Immunofluorescence image: c),d) the cells(NIH-3T3) were stained for actin (red colour, using phalloidin), the nuclei were stained with DAPI (blue colour) on squid pen with fibrin network.

In collaboration with the previously mentioned prof. Graziella Pellegrini of the Center for Regenerative Medicine to the University of Modena and Reggio Emilia, preliminary tests were performed with keratinocytes from human cadaver cornea. Trypsinized cells of a single limbal biopsy of 1–2 mm² were cultivated on a feeder layer of lethally irradiated clinical grade [(GMP (good manufacturing practice)-certified] 3T3-J2 cells in the presence of an appropriately selected fetal calf serum. The subconfluent primary culture has been trypsinized and a portion of the cells has been transferred to a secondary culture on the chitin samples (on 3T3- J2 feeder cells), as shown in figure 6.10. In these preliminary experiments the cells show, over short cell culture time, a good adhesion even if the coverage was not homogeneous, indicating the a further tuning of the surface preparation is required.

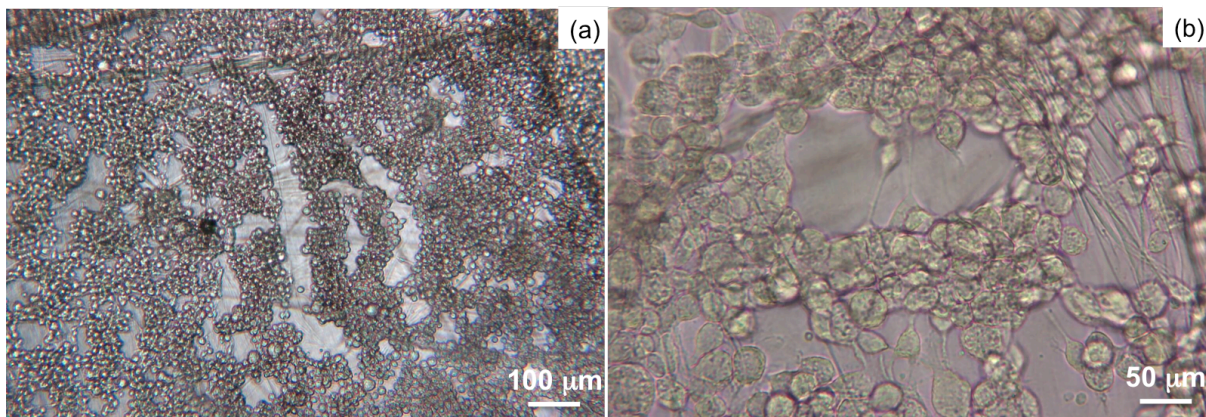


Figure 6.10: Optical images: a),b) human keratinocytes on squid pen.

6.4 Conclusions

We have proposed to use the squid pen as a scaffold for the regeneration of human cornea, because it is biocompatible, transparent, withstanding surgical sutures and, moreover, it is a waste material of the industrial chain. The purpose of this work was to exploit as much as possible the original remarkable properties provided by the structure of squid pen chitin to obtain a scaffold transparent and able to support all the mechanical stress of the cornea. We have shown that partial chemical and physical changes we can improve both secondary primary human cells adhesion. The potential of this material may go beyond the cornea application; due to its high healing power³⁰ h it can in fact also be used to regenerate other tissues such as cartilage. Furthermore, in a period characterized by the necessity of producing goods by a sustainable chemistry and a green economy, finding the way for using any kind available, natural biomass has become a must for all scientists and industrial makers. This is the reason why the industrial use of chitin represents an interesting and new opportunity for the pharmaceutical, cosmetic and textile sectors.

Bibliography

- 1 Lloyd, A. W., Faragher, R. G. & Denyer, S. P. Ocular biomaterials and implants. *Biomaterials* **22**, 769-785, (2001).
- 2 Pellegrini, G., Rama, P., Mavilio, F. & De Luca, M. Epithelial stem cells in corneal regeneration and epidermal gene therapy. *J Pathol* **217**, 217-228, (2009).
- 3 Cotsarelis, G., Cheng, S. Z., Dong, G., Sun, T. T. & Lavker, R. M. Existence of Slow-Cycling Limbal Epithelial Basal Cells That Can Be Preferentially Stimulated to Proliferate - Implications on Epithelial Stem-Cells. *Cell* **57**, 201-209, (1989).
- 4 Schermer, A., Galvin, S. & Sun, T. T. Differentiation-related expression of a major 64K corneal keratin in vivo and in culture suggests limbal location of corneal epithelial stem cells. *J Cell Biol* **103**, 49-62, (1986).
- 5 Lehrer, M. S., Sun, T. T. & Lavker, R. M. Strategies of epithelial repair: modulation of stem cell and transit amplifying cell proliferation. *Journal of cell science* **111 (Pt 19)**, 2867-2875, (1998).
- 6 Sharma, A. & Coles, W. H. Kinetics of corneal epithelial maintenance and graft loss. A population balance model. *Investigative ophthalmology & visual science* **30**, 1962-1971, (1989).
- 7 Mort, R. L., Ramaesh, T., Kleinjan, D. A., Morley, S. D. & West, J. D. Mosaic analysis of stem cell function and wound healing in the mouse corneal epithelium. *BMC developmental biology* **9**, 4, (2009).
- 8 Huang, A. J. & Tseng, S. C. Corneal epithelial wound healing in the absence of limbal epithelium. *Investigative ophthalmology & visual science* **32**, 96-105, (1991).
- 9 Majo, F., Rochat, A., Nicolas, M., Jaoude, G. A. & Barrandon, Y. Oligopotent stem cells are distributed throughout the mammalian ocular surface. *Nature* **456**, 250-254, (2008).

- 10 Pellegrini, G. *et al.* Location and clonal analysis of stem cells and their differentiated progeny in the human ocular surface. *J Cell Biol* **145**, 769-782, (1999).
- 11 Farrell, R. A. & McCally, R. L. On corneal transparency and its loss with swelling. *Journal of the Optical Society of America* **66**, 342, (1976).
- 12 Maurice, D. M. The structure and transparency of the cornea. *The Journal of physiology* **136**, 263-286, (1957).
- 13 Karsten Plamann, C. A., Caroline Crotti, Florent Deloison, Valeria Nuzzo, Donald A. Peyrot, Florent Aptel, Antoine Courjaud, Éric Mottay, Frédéric Druon, Patrick Georges, Marc Hanna, Franck Morin, Jean-Marc Legeais and Michèle Savoldelli. Ultrashort-pulse laser eye surgery uses fiber technology at 1.6 microns. *SPIE*, (2009).
- 14 Kenyon, K. R. & Tseng, S. C. Limbal autograft transplantation for ocular surface disorders. *Ophthalmology* **96**, 709-722; discussion 722-703, (1989).
- 15 Lindberg, K., Brown, M. E., Chaves, H. V., Kenyon, K. R. & Rheinwald, J. G. In vitro propagation of human ocular surface epithelial cells for transplantation. *Investigative ophthalmology & visual science* **34**, 2672-2679, (1993).
- 16 Pellegrini, G. *et al.* Long-term restoration of damaged corneal surfaces with autologous cultivated corneal epithelium. *Lancet* **349**, 990-993, (1997).
- 17 Pellegrini, G. *et al.* The control of epidermal stem cells (holoclones) in the treatment of massive full-thickness burns with autologous keratinocytes cultured on fibrin. *Transplantation* **68**, 868-879, (1999).
- 18 Rama, P. *et al.* Autologous fibrin-cultured limbal stem cells permanently restore the corneal surface of patients with total limbal stem cell deficiency. *Transplantation* **72**, 1478-1485, (2001).
- 19 De Luca, M., Pellegrini, G. & Green, H. Regeneration of squamous epithelia from stem cells of cultured grafts. *Regen Med* **1**, 45-57, (2006).
- 20 McIntosh Ambrose, W., Schein, O. & Elisseeff, J. A tale of two tissues: stem cells in cartilage and corneal tissue engineering. *Current stem cell research & therapy* **5**, 37-48, (2010).
- 21 Falini, G. *et al.* The interstitial crystal-nucleating sheet in molluscan *Haliotis rufescens* shell: a bio-polymeric composite. *Journal of structural biology* **173**, 128-137, (2011).
- 22 Fernandez, J. G. & Ingber, D. E. Bioinspired Chitinous Material Solutions for Environmental Sustainability and Medicine. *Adv Funct Mater* **23**, 4454-4466, (2013).
- 23 Noishiki, Y., Nishiyama, Y., Wada, M., Okada, S. & Kuga, S. Inclusion complex of beta-chitin and aliphatic amines. *Biomacromolecules* **4**, 944-949, (2003).
- 24 Falini, G., Fermani, S. & Ripamonti, A. Crystallization of calcium carbonate salts into beta-chitin scaffold. *J Inorg Biochem* **91**, 475-480, (2002).
- 25 Noishiki, Y. *et al.* Alkali-induced conversion of beta-chitin to alpha-chitin. *Biomacromolecules* **4**, 896-899, (2003).
- 26 Kim, S.-K. *Marine Cosmeceuticals: Trends and Prospects*. (CRC Press, 2011).
- 27 Xu, J., McCarthy, S. P., Gross, R. A. & Kaplan, D. L. Chitosan film acylation and effects on biodegradability. *Macromolecules* **29**, 3436-3440, (1996).
- 28 Hugo, W. B. A Brief-History of Heat and Chemical Preservation and Disinfection. *J Appl Bacteriol* **71**, 9-18, (1991).

- 29 Wang, S. L. *et al.* Reclamation of chitinous materials by bromelain for the preparation of antitumor and antifungal materials. *Bioresource technology* **99**, 4386-4393, (2008).
- 30 Morganti, P., Del Ciotto, P., Morganti, G. & FabienSoulè, V. Application of Chitin Nanofibrils and Collagen of Marine origin as Bioactive Ingredients. *Marine Cosmeceuticals: Trends and Prospects*, 267-289, (2013).

Conclusions and Perspectives

The ability to unveil the structure and function of biosystems at the nanoscale has stimulated a wide research leading to improvements in biology, biotechnology, medicine and healthcare. In this framework a major breakthrough has come from the scaffold materials and fabrication technologies that have played a pivotal role in tissue engineering and regenerative medicine. Scaffolds are used to provide sites for cells attachment, proliferation, differentiation and migration by up regulating and down regulating the synthesis of protein and growth factors. They provide mechanical support, deliver inductive molecules or guide cells to the repair site. The incorporation of bioactive molecules like the growth factor, enzymes, proteins are crucial while designing a scaffold.

In this work I have presented different nanotechnology-based approaches for the fabrication of multiscale structures and devices that can be used for understanding the behaviour of systems relevant to regenerative medicine. Through the use of soft lithography techniques, we have demonstrated an easy method for fabricating gradients of an ECM protein, laminin, with a controlled and reproducible geometry. This study shows that is possible to achieve directional and spatial control of neural cell growth over long periods of time by means of patterned protein gradients. Patterning is an effective tool to govern the chemical stimuli-induced organization of different cell phenotypes, and this can be performed also in co-culture studies. Indeed, the next step was to fabricate a 3D scaffold where we are able to control the main morphological parameters such as porosity. In fact, equilibrium is needed between highly porous scaffolds that allow rapid tissue ingrowths and minimize diffusion limitations and less porous materials that retain both construct shape and the ability to bear mechanical loads in a complex biochemical and mechanical environment. An accurate morphological analysis is crucial because they morphological properties describe the degree of porosity, which must be large enough to permit the cell migration and the diffusion of signalling molecules and nutrients and a network dense enough to allow the development of a good number of adhesion points for each cell. Furthermore, we have exploited the porosity of the scaffold of fibrin made to incorporate micro-crystals of calcium carbonate. This approach aims at combining the versatility of fibrin as a material for scaffold fabrication with the possibility to release in a time and position controlled way molecules required for tuning the cell fate. The proposed work is an alternative method for drug delivery that can be used in tissue engineering applications. This strategy can be a starting point for fabricating multifunctional devices by tailoring the chemical, physical and morphological properties of the device thus providing cues for directing cell behaviour in tissue engineering applications. In the last part we propose a novel strategy for fabricating scaffolds using natural materials that come from sea organisms, this materials has been thoroughly optimized by nature. Squid pen is a chitin made biocompatible scaffold, transparent, mechanically resistant and, last but not least, a waste material of the industrial chain. The potential of this material may go beyond the cornea application; due to its high healing power, it can in fact also be used to regenerate other tissues such. Furthermore, in a period characterized by the necessity of

producing goods by a sustainable chemistry and a green economy, finding a way for using any kind of available, natural biomass has become a must for all scientists and industrial makers.

It is evident that nanotechnology will be a critical tool in the fight to resolve current critical medical issues. The nanoscale assembly of organic and inorganic matter leads to the formation of cells and to the most complex known systems - the brain and human body. Nanotechnology plays a key role in understanding these processes and in the advancement of biological sciences.

Participation to meeting and conferences:

- “Design, fabrication and porosity analysis of a biocompatible scaffolds for regeneration of tissue”. **M. Barbalinardo**, F. Valle, M. Di Giosia, M. Calvaresi, G. Falini, G. Pellegrini and F. Biscarini. XIII Giornata della Chimica dell’Emilia Romagna. Bologna, Italy, 18 December 2013.
- “Design, fabrication and porosity analysis of a biocompatible scaffolds for regeneration of tissue”. **M. Barbalinardo**, F. Valle, L. Lungaro, G. Falini, G. Pellegrini and F. Biscarini. 13° Sigma Aldrich Young Chemists Symposium: 13° S.A.Y.C.S. Hotel Atlantic-Riccione, Italy, 28-30 October 2013
- “Fabrication, characterization and porosity analysis of a scaffold based on a standing fibrin” **M. Barbalinardo**, F. Valle, B. Chelli, E. Bystrenova, G. Falini, G. Pellegrini and F. Biscarini. CESB2013, Sorrento, Italy, 1-4 July 2013.
- “Fabrication, characterization and porosity analysis of a scaffold based on a standing fibrin” **M. Barbalinardo**, F. Valle, B. Chelli, E. Bystrenova, G. Falini , G. Pellegrini and F. Biscarini. E-MRS 2013 Spring Meeting, Strasburg, France, 27-31 May 2013.
- “Laser Assisted Bioprinting of Laminin on biodegradable substrates for cell culturing”. S. Tortorella, P. Greco, F. Valle , G. Foschi, **M. Barbalinardo**, B. Chelli and F. Biscarini. E-MRS 2013 Spring Meeting Strasburg, France, 27-31 May 2013.
- “Fabrication, characterization and porosity analysis of scaffold based on a standing fibrin“ **M. Barbalinardo**, F. Valle, E. Bystrenova, G. Foschi, E. Zanotto and F. Biscarini. XII Giornata della Chimica dell’Emilia Romagna. Ferrara, Italy, 17 December 2012.
- “Fabrication, characterization and porosity analysis of scaffold based on a standing fibrin film“. **M. Barbalinardo**, F. Valle, E. Bystrenova, G. Foschi and F. Biscarini. 9th International Conference on Nanosciences & Nanotechnologies. Thessaloniki, Greece, 3-6 July 2012.
- “Fabrication of scaffold based on a standing fibrin film: Scanning Electron Microscopy characterization“ **M. Barbalinardo**, F. Valle, M. Bianchi, E. Bystrenova, P. Greco and F. Biscarini. Summer School on Biomaterials and Regenerative Medicine: From molecular and cell biology to tissues and organ repair. Riva del Garda, Italy, 19-23 September 2011.
- “Multiscale length scale patter fabrication for regenerative medicine”. B. Chelli, E. Bystrenova, F. Valle, M. Bianchi, **M. Barbalinardo**, A. Shehu, T. Cramer, G. Foschi, M. Murgia, A. Piccoli, P. Greco and F. Biscarini. X Convegno Materiali Nanofasici, Bologna, Italy, 9 September 2011.
- “Fabrication of scaffold based on a standing fibrin film: Scanning Electron Microscopy characterization“. **M. Barbalinardo**, F. Valle, M. Bianchi, E. Bystrenova, P. Greco and F. Biscarini. 10th Multinational Congress on Microscopy 2011, Urbino, Italy, 4-9 September 2011.
- “Multiscale patterning for regenerative medicine” E. Bystrenova, F. Valle, B. Chelli, M. Bianchi, P. Greco, A. Bergia, G. Foschi, **M. Barbalinardo**, M. Cavallini and F. Biscarini. Tuurkish Italian Workshop on the Frontiers in Nanomaterial Research and Applications, Istanbul, Turkey, 8-10 December 2010

Trainings:

- “Science through Scanning Probe Microscopy StSPM’13 ”. Consiglio Nazionale delle Ricerche of Bologna. Organized by Dr. Cristiano Albonetti, Dr. Francesco Valle and Prof. Fabio Biscarini. December 2013
- “Scuola di Microscopia Elettronica “Pier Giorgio Merli””. Consiglio Nazionale delle Ricerche of Bologna. Organized by Dr. Roberto Balboni and Dr. Andrea Parisini. November 2012 e February 2013
- “Scuola Avanzata teorica-pratica di Microscopia a Scansione di Sonda”. Consiglio Nazionale delle Ricerche of Bologna. Organized by Prof. Fabio Biscarini. November 2011
- Bologna Winter School: “Grand Challenges in Computational Biology: New development for solving the unsolved problems of Computational Biology”. University of Bologna. Organized by Prof. Rita Casadio. February 2009

Publications:

- “Morphological Analysis of Fibrillar Scaffolds for Tissue Engineering”. **M. Barbalinardo**, F. Valle, G. Falini, G. Pellegrini and F. Biscarini (*in preparation*)
- “Laser Assisted Bioprinting of Laminin on biodegradable PLGA substrate for neural stem cell adhesion and differentiation”. S. Tortorella, P. Greco, F. Valle, **M. Barbalinardo**, G. Foschi and F. Biscarini (*in preparation*)
- “Neural Cell Alignment by Patterning Gradients of the Extracellular Matrix Protein Laminin“ B. Chelli, **M. Barbalinardo**, F. Valle, E. Bystrenova, M. Bianchi, P. Greco, and F. Biscarini Interface Focus 2014 February 4;1, 200130041.
- “Fabrication, characterization and porosity analysis of a scaffold based on fibrin glue “ **M. Barbalinardo**, F. Valle, B. Chelli, E. Bystrenova, G. Foschi, E. Zanotto, G. Falini, G. Pellegrini and F. Biscarini. La chimica e l’industria 2013, 7.
- “Organic Ultra-Thin Film Transistor with Liquid Gate for Extracellular Stimulation and Recording of Electric Activity of Stem Cell-Derived Neuronal Networks” T. Cramer, B. Chelli, M. Murgia, **M. Barbalinardo**, E. Bystrenova, D.M. de Leeuw and F. Biscarini Physical Chemistry Chemical Physics 2013 Mar 21;15(11):3897-905.
- “Selective Growth of α -Sexithiophene by Using Silicon Oxides Patterns” C. Albonetti, **M. Barbalinardo**, S. Milita, M. Cavallini, F. Liscio, J.F. Moulin and F. Biscarini Int J Mol Sci. 2011; 12(9): 5719-5735.
- “Multiscale pattern fabrication for life-science applications” F. Valle, B. Chelli, M. Bianchi, E. Bystrenova, **M. Barbalinardo**, A. Shehu, T. Cramer, M. Murgia, G. Foschi, P. Greco, M. Cavallini and F. Biscarini European Biophysics Journal with Biophysics Letters 2010; 40: 233-234.

Ringraziamenti

Prima di tutto vorrei ringraziare il Prof. Fabio Biscarini per tutto ciò che mi ha insegnato e per avermi dato la possibilità di svolgere il mio dottorato presso i laboratori del CNR.

Un ringraziamento particolare va al mio tutor Dr. Francesco Valle per tutto ciò che mi ha trasmesso, per avermi dato la possibilità di poter seguire le mie curiosità scientifiche, per avermi fatto conoscere dei ricercatori eccezionali con i quali collaborare, per avermi sostenuto, sopportato ed aver creduto in me durante questo periodo di dottorato.

Ringrazio il Prof. Giuseppe Falini per la sua disponibilità, per la sua umiltà scientifica e per avermi dato la possibilità di poter lavorare con lui e con il suo meraviglioso gruppo, tra i quali mi sento di ringraziare Dr. Matteo Calvaresi, Dr. Stefania Rapino, Matteo Di Giosia, Alessandro Ianiro e Michela Reggi.

Un grosso grazie a tutti i ragazzi del laboratorio e di ufficio Silvia, Adrica, Alessandra, Zahra, Michele, Stefano (Chiodo), Rafael, la cui compagnia ha reso più divertenti e spensierate le lunghe giornate in laboratorio, inoltre per me in questi anni non sono stati solo dei colleghi ma anche degli amici sui quali poter contare nei momenti di difficoltà.

Grazie a Lisa, Stefano (Casolo), Denis, Massimiliano (Max), Patrizia, Eva, Tobias e Beatrice per tutti i consigli e per la loro disponibilità.

Vorrei dire grazie ad Elettra Zanutto con la quale ho condiviso un anno di esperienza in laboratorio ed è stata la prima laureanda che ho avuto la possibilità di seguire nel suo percorso di tesi.

Un grazie speciale va a Giulia e Francesca (Chicken Corner), che ormai non le reputo più mie colleghe ma amiche sincere con le quali abbiamo condiviso i momenti più belli e più difficili in questi anni e mi auguro che questa amicizia non finisca mai.

Grazie a tutta la mia famiglia, in modo particolare a mia mamma per avermi sostenuta e incoraggiata e spero che sia orgogliosa di me.

Un ultimo grazie al mio compagno di vita e sventuta, Luigi, il quale ha condiviso ogni momento di questo percorso, che mi ha ascoltato, capito, consigliato e sopportato.

Infine, ringrazio tutte le persone che non ho nominato esplicitamente, ma che hanno creduto in me.

GRAZIE di CUORE

Marianna